Lead Detection and Mapping with Reference to Relationships Between Scale, Sensor Characteristics, Surface Conditions and Atmospheric Properties
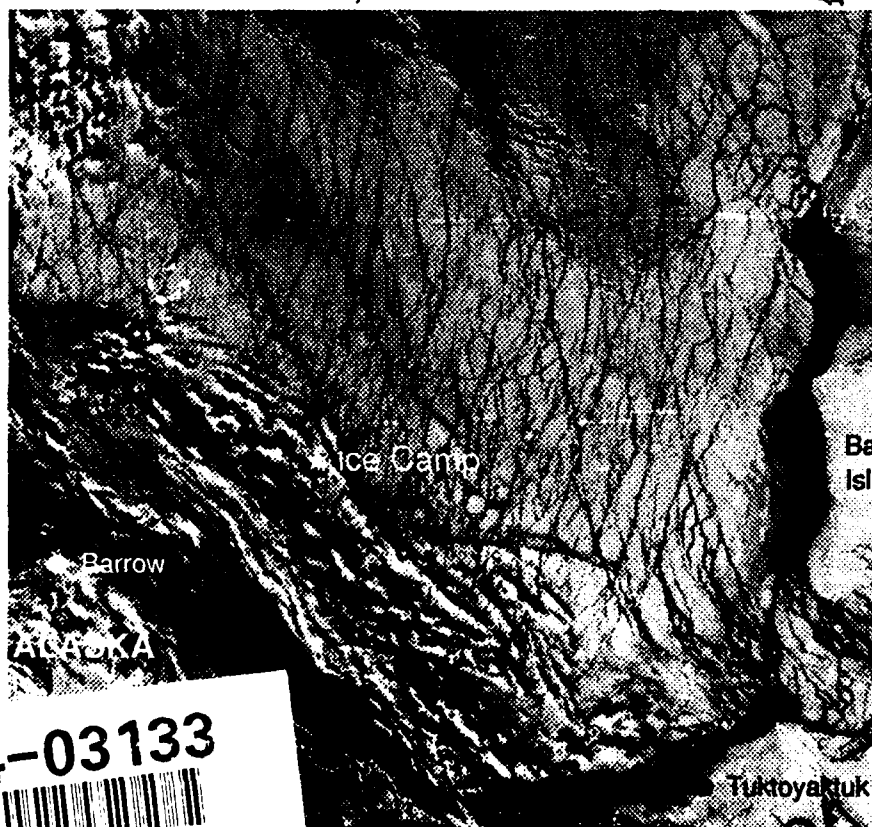
FINAL REPORT

S DTIC
ELECTE
FEB 0 1 1994
A

J. Key, J.A. Maslanik, and R.S. Stone

Division of Cryospheric and Polar Processes
Cooperative Institute for Research in Environmental Sciences
University of Colorado at Boulder

AD-A275 321

AVHRR Channel 2, LEADEX Area

Banks Island

Ice Camp

Barrow

ALASKA

Tuktoyaktuk

94-03133

94 1 31 219

Lead Detection and Mapping with Reference to Relationships Between Scale, Sensor Characteristics, Surface Conditions and Atmospheric Properties
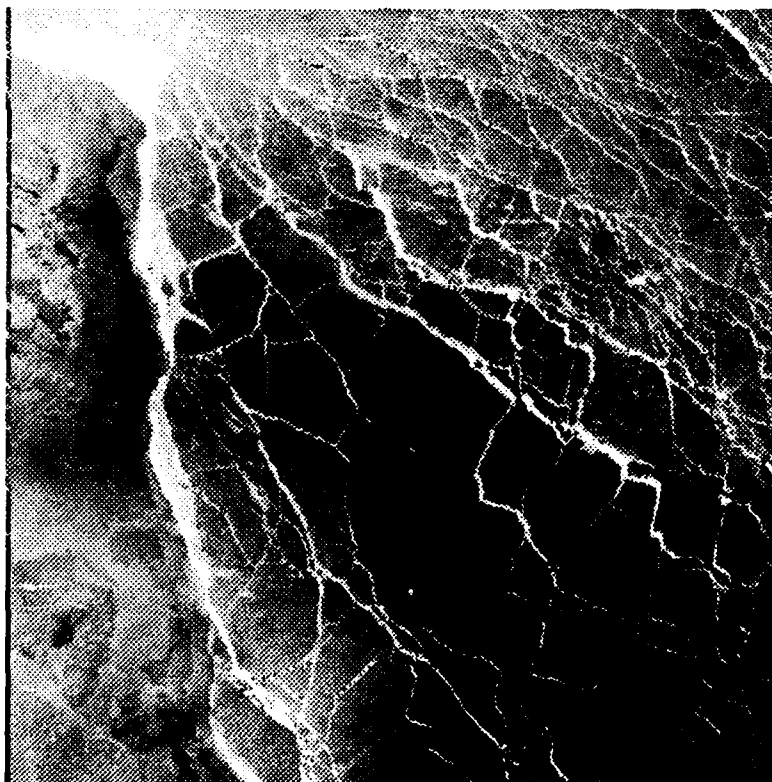
FINAL REPORT

15 April 1991 - 31 October 1993

ONR Grant No: N00014-90-J-1840

J. Key, J.A. Maslanik, and R.S. Stone

Cooperative Institute for Research in Environmental Sciences
Division of Cryospheric and Polar Processes
University of Colorado
Boulder, CO 80309-0449

Accesion For		
NTIS CRA&I		☑
DTIC TAB		☐
Unannou...ed		☐
Justification		
By A 250437		
Distribution /		
Availability Codes		
Dist	Avail and/or Special	
A-1		

ATSR Thermal Image of the Beaufort Sea

TABLE OF CONTENTS

SUMMARY

During the three project years, empirical studies of scale relationships in the retrieval of sea ice lead statistics have been undertaken, as have modeling investigations of atmospheric influences on the satellite signal. Additionally, we have developed statistical models that describe the scaling properties of leads. The empirical studies have been based primarily on comparisons within and between Landsat and AVHRR imagery, while the atmospheric models have been specific to the AVHRR. Submarine sonar data have been used in the statistical model development.

Specific accomplishments include: atmospheric temperature and humidity profiles for the Arctic have been constructed from Soviet ice island data and were used in the construction of three-season "standard" atmospheres for the central Arctic; resampling methods have been tested on various types of imagery, and nearest-neighbor resampling has been shown to be the most effective in maintaining the spectral characteristics of leads while spatial interpolation (e.g., bilinear) retains their spatial structure; empirical relationships between pixel size and lead width have been determined; procedures for the retrieval of lead statistics have been developed and applied to Landsat and ERS-1 SAR data; the relationship between "apparent" lead widths measured along a transect (e.g., from submarine sonar or as a sampling method for satellite imagery) and the "true" lead width distribution has been formalized in a statistical sense, so that one distribution may be obtained from the other; a statistical model has been developed for the retrieval of lead area fraction from measurements along a line; a method to partially adjust the total lead area fraction for field-of-view was developed and tested on AVHRR and Landsat imagery; a combination of SAR and AVHRR was used to estimate true lead temperature and width; the effects of atmosphere/surface conditions on the AVHRR-measured radiance in the thermal channels have been examined in terms of the thermal contrast between leads and the surrounding ice pack and the relationship between atmospheric optical depth and lead size has been quantified; information on Arctic aerosol optical depths during LEADEX has been collected by two of the investigators and has been used to assess the extent of tropospheric and stratospheric aerosols and their effect on lead detection from satellite; satellite and *in situ* data collected during LEADEX and SIMMS'92 have been used to test the theoretical and empirical models/methods developed during the first two project years, and shows these models/methods to be generally valid.

Additionally, two workshops for the satellite remote sensing investigators of the Leads ARI were hosted by this group in Boulder. One workshop report and seven referreed papers have been published, with three others in press or submitted for publication. Two graduate students have been supported part-time over the course of the project.

PROJECT OBJECTIVES

The goal of this project is to understand how sensor characteristics, atmospheric properties, and surface conditions influence the detection and interpretation of sea ice leads using Advanced Very High Resolution Radiometer (AVHRR) and other satellite data. We seek to determine the sources and magnitudes of errors inherent in the measurements, how data from different sensors can be combined, and how lead statistics change with the different spatial resolutions of existing and future sensors.

In partial fulfillment of these objectives, we have defined which atmospheric and surface parameters are most critical for lead detection. Based on model simulations, we have been able to better evaluate the importance of Arctic-specific model parameters; e.g., temperature and humidity profiles and aerosols, for the purpose of accurately simulating sensor responses. Sensor characteristics such as spectral response, field-of-view, spatial resolution, scan geometry and data processing methods coupled with scene variability (solar zenith angle, atmospheric opacity, surface temperature, snow cover, ice thickness, size with respect to sensor resolution) determine feature signatures. The effects of these parameters had to be examined before lead signatures could be evaluated in terms of lead width and orientation, particularly for features that occur near spatial and radiometric limits of sensor resolution.

The NOAA AVHRR satellite sensor provides daily, Arctic-wide coverage of ice conditions at moderate resolution and low cost. These image sets contain information that is of primary concern to research and operational interests in the Arctic. Although a variety of studies have examined various aspects of remote sensing of sea ice, essentially no work had previously been done to relate lead signatures observed in AVHRR data to lead characteristics. This lack of substantive verification work left key questions unanswered and posed significant research problems relevant to current lead investigations. Specifically, the following questions motivated our research:

Lead and Surface Characteristics: How does lead detection depend on ice thickness for given sets of sensor properties, surface temperatures, and atmospheric conditions? Since the temperature contrast between open water and ice provides a means to map leads using thermal imagery, to what degree does this contrast affect the apparent width of a lead as observed in an image and our ability to detect it? Does lead orientation affect lead detection when a wide-angle scanning instrument such as AVHRR is used instead of a nadir-viewing sensor such as Landsat? How accurately must surface temperatures be measured to yield accurate lead calculations?

Atmospheric, Boundary Layer, and Solar Zenith Angle Effects: How do these factors combine with surface conditions and path length to the sensor to determine the thresholds of lead detection? What feedbacks to the atmosphere do leads create, and how will these affect detection; e.g., ice crystal plumes from open leads that extend up to - and in some cases through - the top of the inversion layer? What are the characteristics of "typical" polar atmospheres (i.e., water vapor content, temperature profiles, cloud microphysical characteristics), how are they treated in radiative transfer models, and how do these factors affect remote sensing?

General Sensor Considerations: In what ways might sensor scan-angle, sensor calibration, data gridding, and image enhancements influence the ability to detect leads? Are lead statistics derived from image centers where spatial resolution is greatest comparable to those derived from image limbs where resolution is poorest?

While we do not claim to be able to answer all of these questions completely, the results of the past three years' research have given us at least partial answers to each.

To accomplish our objectives, our approach included both modeling and empirical studies (Figure I.1). The radiative transfer modeling is done for the purpose of simulating the satellite sensor response under a variety of atmospheric and surface conditions. The empirical studies include: a comparison of lead statistics determined in imagery of varying scales; e.g., AVHRR, Landsat, SAR, and OLS data; effects of different resampling methods and digital image enhancements on lead detection in AVHRR and Landsat data; use of distributions derived from the low resolution imagery to estimate characteristics of the distributions obtained in the high resolution images; and the relationship between lead width and spacing statistics measured along a transect to the true distributions.

Results from this work will be important to the development and application of lead detection and mapping algorithms proposed elsewhere within the Leads ARI. For example, the ability to more accurately access lead width and spacing distributions from medium resolution imagery is crucial to the evaluation of large-scale heat flux estimates. The modeling and empirical approaches to quantifying the relationships of scale discussed here are a necessary first step to operational lead analysis from satellite data.

Satellite data used in this study includes Landsat visible, AVHRR visible and thermal, ERS-1 SAR, and OLS visible and thermal. Additionally, lead statistics have been derived from submarine sonar data. Radiosonde temperature and humidity profiles from arctic ice islands are employed for radiative transfer studies. Each data type is described in more detail in the appropriate sections.

This report is divided into four parts. The first details those studies that directly relate to retrieving lead statistics from satellite imagery: image preprocessing, sensor field-of-view, and sampling methods. The second part describes radiative transfer studies of how the atmosphere affects the satellite signal and how this in turn might affect lead statistics derived from the imagery. Part III details the use of data collected during LEADEX and other field experiments. Part IV summarizes the accomplishments to date.
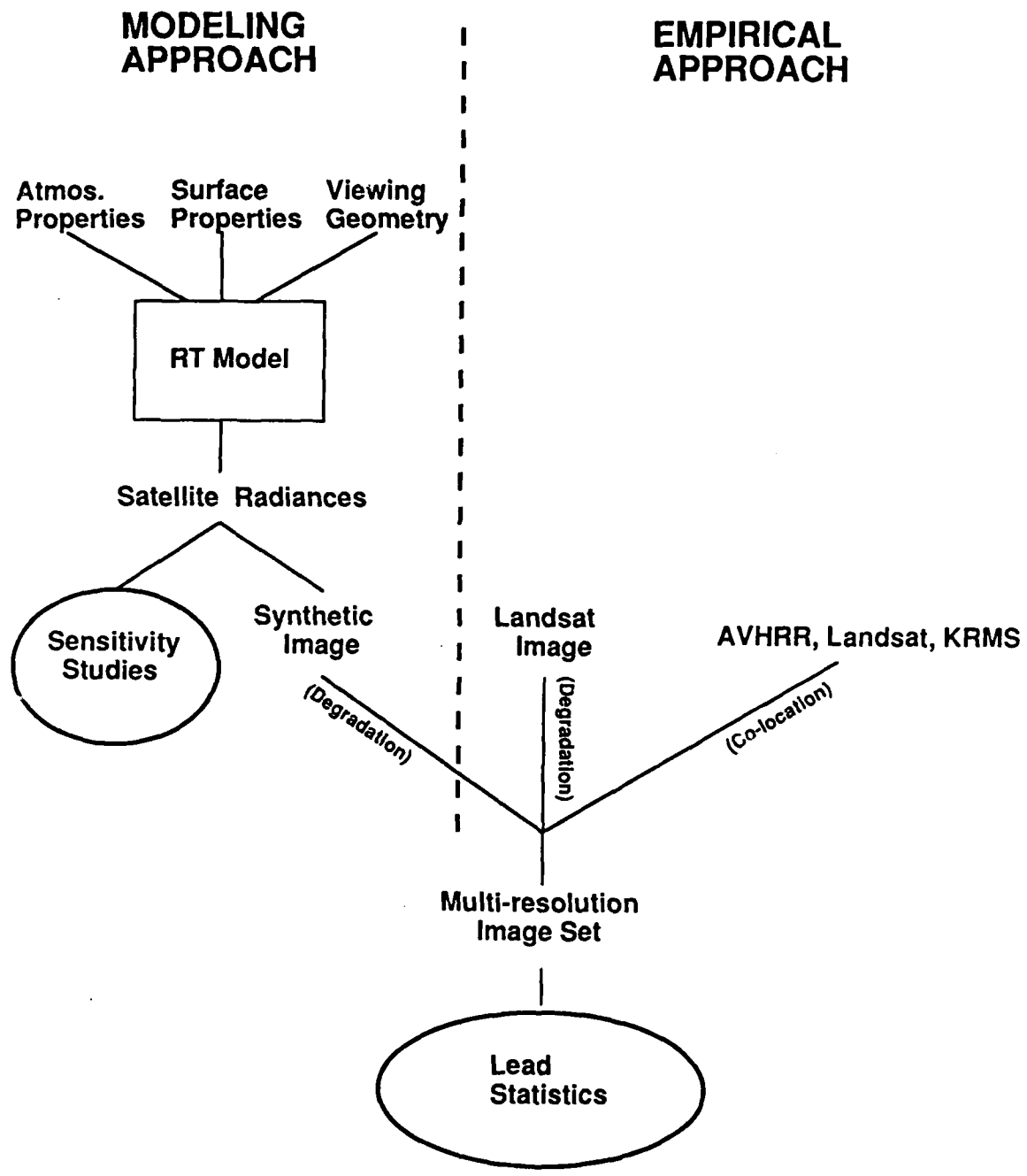
Fig. I.1. Overview of the modeling and empirical approaches to the study of lead mapping and relationships of scale in satellite data. The radiative transfer model on the left is used for sensitivity studies and to generate simulated imagery. This imagery as well as Landsat data are degraded to coarser resolutions. The simulated multi-resolution data sets, along with actual data from different satellite sensors, are used to study the effects of measurement scales on derived lead statistics.

PART I: IMAGE-RELATED STUDIES

The empirical portion of this study involves the comparison of AVHRR, Landsat, and - to a limited extent - KRMS data. These sensors provide a broad range of spectral and spatial resolutions. In this section, the potential effect of image preprocessing methods on lead statistics is examined.

I.1 IMAGE PREPROCESSING AND ITS EFFECT ON LEAD STATISTICS

Figures I.2 and I.3 show the effect on lead detection in AVHRR imagery of different resampling methods and different digital number thresholds for "lead / no lead" mapping. The plots in Figure I.2 of digital numbers along transects in AVHRR data processed using different resampling schemes show some relatively small shifts in digital number (DN) within leads and adjacent to leads, which would yield a change in estimated lead-covered area (such as at transect location 292-293 in Figure I.2a). For small leads, the potential exists to perhaps mask the lead completely (as at transect location 279 in Figure I.2a). Figure I.3a shows results using a threshold that detects small and large leads. The threshold used for Figure I.3b detects only the larger leads. The effect of the "smoothing" interpolations (bilinear and cubic convolution) is to eliminate about 40% of the smallest leads using this threshold detection scheme. Figure I.4 summarizes the effect of threshold and resampling scheme on total lead-covered area (in this case, the percent of an AVHRR image covered by leads). The effect of using different resampling schemes is small compared to the effect of choosing different thresholds. Thus, while Figure I.3 suggests a substantial reduction in small leads when interpolations are used vs. nearest neighbor, the effect of the loss of these small leads on total lead area is relatively small. However, it is also worth noting that, since the turbulent fluxes from a given lead-covered area may increase as the proportion of lead-covered area in narrow leads (as opposed to wide leads) increases, any systematic shift by the processing scheme toward a reduction in small leads may need to be considered when calculating regional estimates of surface fluxes.

To further examine the effects of different interpolation schemes, "synthetic" images containing a simulated lead or lead complex with different shapes and dimensions (e.g., the patterns shown in Figure I.5) are used. Four lead types were created (e.g., "Type 1", etc. in Figure I.5): Type 1 represents narrow open-water leads; Type 2 wider open-water leads; Type 3 leads with new and young ice growing from the edges of the leads; and Type 4 representing leads with new ice building up along one side of the leads. These images were then resampled using bilinear interpolation and nearest-neighbor methods. Resampling was applied to a 45° rotation of the original images. Table I.1 lists the change in lead-covered area resulting from the resampling and determined using two different thresholds. A DN of 10 (a typical reflectance for open water) was chosen to represent open water and a DN of 85 was used for ice-covered pixels. The effects are clearly dependent on the threshold chosen to define the cut-off between whether to consider a pixel as part of a lead or not. Both the bilinear and nearest neighbor interpolations cause large reductions in the area assumed to be open water. When a threshold is chosen at a higher reflectance, such as would be appropriate to detect all pixels with some open water or thin ice in them, then the percentage of pixels with some lead-covered area increases substantially when bilinear interpolation is used.

In addition to affecting the calculation of lead-covered area, the different resampling schemes affect the appearance of leads in an image, and thus the ability of an interpreter or automated pattern-recognition scheme to detect the leads. In particular, nearest neighbor resampling tends to break up the

linearity of leads. Figure I.6 shows a lead complex in Landsat imagery resampled using nearest neighbor (Figure I.6a), with an attempt at reconstituting the linearity using a median filter (Figure I.6b). As with most enhancements, the improvement is subjective, but the lead patterns appear more well defined in the median-filtered image.

Additional insight into the effects of spatial resolution and sensor properties can be gained by comparing colocated imagery from different sensors. Figure I.7 shows registered Landsat Multi-spectral Scanner (MSS) imagery (top) and AVHRR data (bottom) for a portion of the Beaufort Sea. While the same general lead structure is apparent in both images, the ability to detect the smaller leads is considerably reduced in the AVHRR image (maximum spatial resolution of 1.1 km) vs. the 80 m Landsat image. This effect of spatial resolution on lead detection, as well as the effect of different spectral information on lead mapping, is also illustrated in Figure I.8, which shows a subsection of the Landsat and AVHRR images, as well as a KRMS strip superimposed on the Landsat data. This comparison of how leads are represented in visible-band wavelengths (the Landsat), thermal (AVHRR), and passive microwave (KRMS), points out the problems of intercomparing lead statistics derived from different sensors. In this example, threshold detection of lead-covered area in the three data types yields 1.1% lead-covered area in the Landsat, 12.8% in the AVHRR (which includes apparent low cloud with substantially warmer temperatures than the ice surface), and 5.4% lead-covered area in the KRMS image.

These different representations are perhaps better represented by comparing transects through the imagery. Figure I.9 shows such a transect. The lead located at transect location 32 is marked with an arrow on the Landsat image in Figure I.8. The transect runs vertically through the imagery. In this example, a contrast stretch was applied to the AVHRR data to enhance the subtle DN differences in the image. From these comparisons and a similar comparison of transects in AVHRR (unenhanced) and Landsat (Figure I.7), it is fairly clear that the AVHRR and Landsat reveal similar lead patterns, but that the number of leads detected, and the image area that is considered to be partially lead-covered, is quite sensitive to the DN threshold chosen to define lead area. In Figure I.9, for example, the large lead at location 32 could be defined as having a lead width from 800 m to about 1500 m in the Landsat data depending on the DN threshold used, and from 300 m to 1800 m in the AVHRR, again depending on which DN is selected. The lead information contained in the KRMS data clearly is quite different from that shown in the other image types.

Table I.1. Effect of resampling method (bilinear interpolation = BL, nearest neighbor = NN) and digital number (DN) threshold on estimation of percent lead-covered area.

Lead Type	Threshold	Fractional Area Lead Coverage (%) (by Resampling Method)		
		None	Bilinear	NN
1	≤ 84	0.65	1.23	0.82
2	≤ 84	1.83	2.61	1.77
3	≤ 84	1.83	2.59	1.77
4	≤ 84	1.83	2.60	1.77
1	≤ 10	0.65	0.01	0.00
2	≤ 10	1.83	˙.19	0.00
3	≤ 10	1.83	0.00	0.00
4	≤ 10	1.83	0.64	0.00
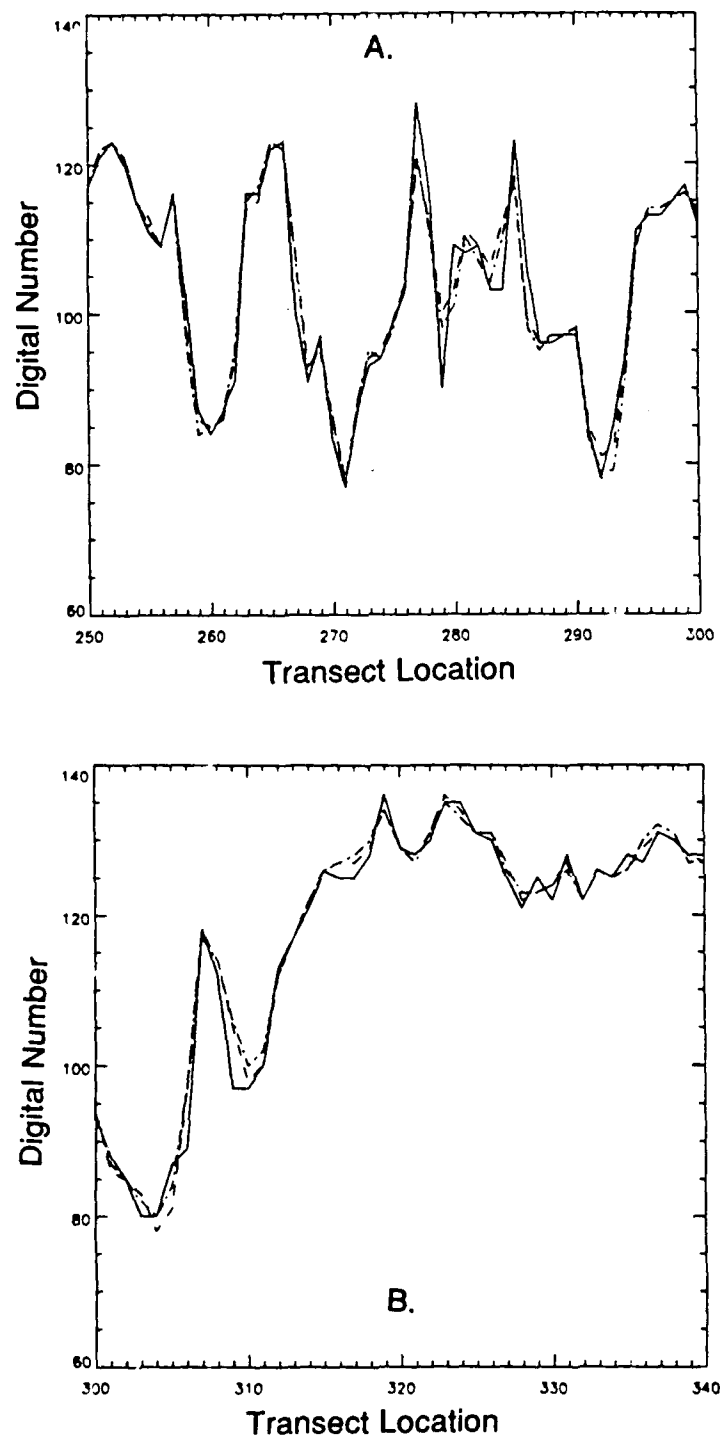
Fig. I.2. Change in AVHRR digital number (DN) using different resampling schemes. Plotted data are two transects (graphs A and B) through three colocated images processed using nearest neighbor (NN) (solid line), cubic convolution (CC) (dashed line), and bilinear interpolation (BI) (dot-dash line).
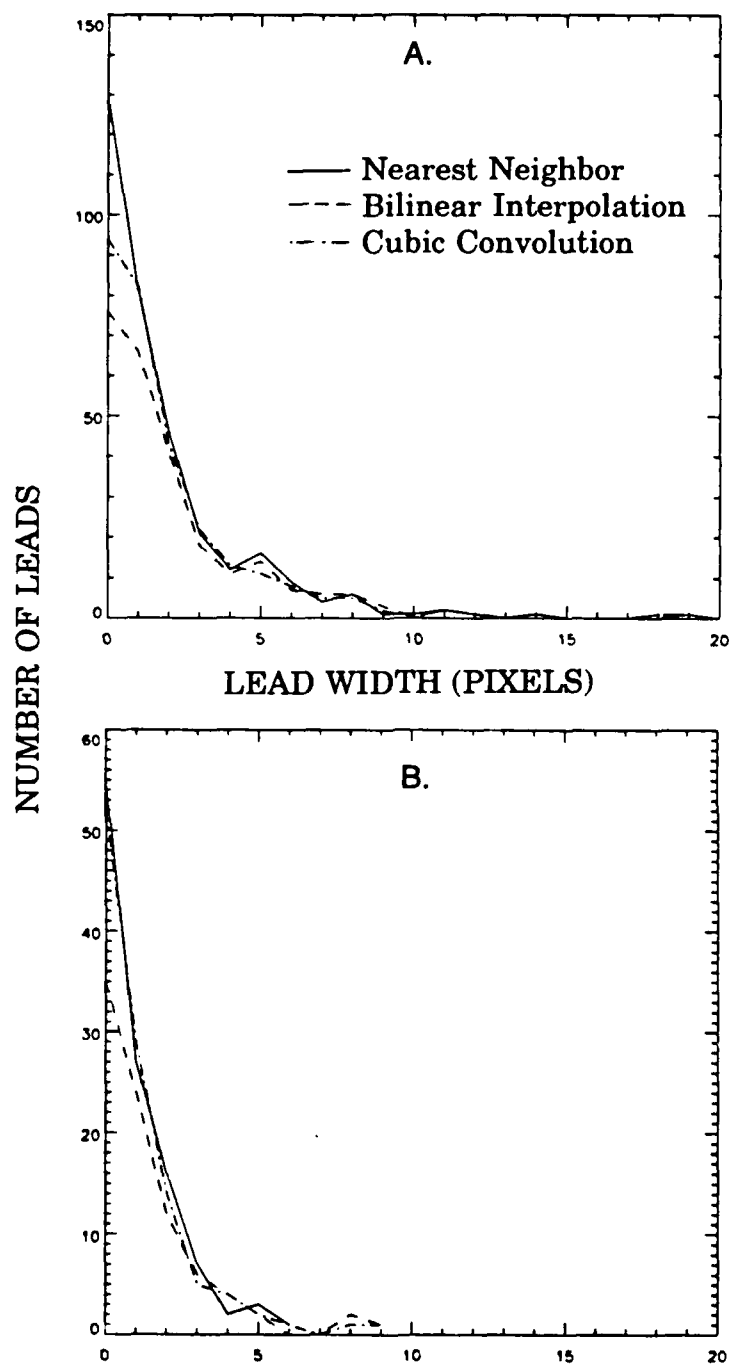
Fig. I.3. Comparison of number of leads encountered in AVHRR imagery resampled using NN, CC, and BI with two different DN thresholds (graphs A and B) used to represent leads.
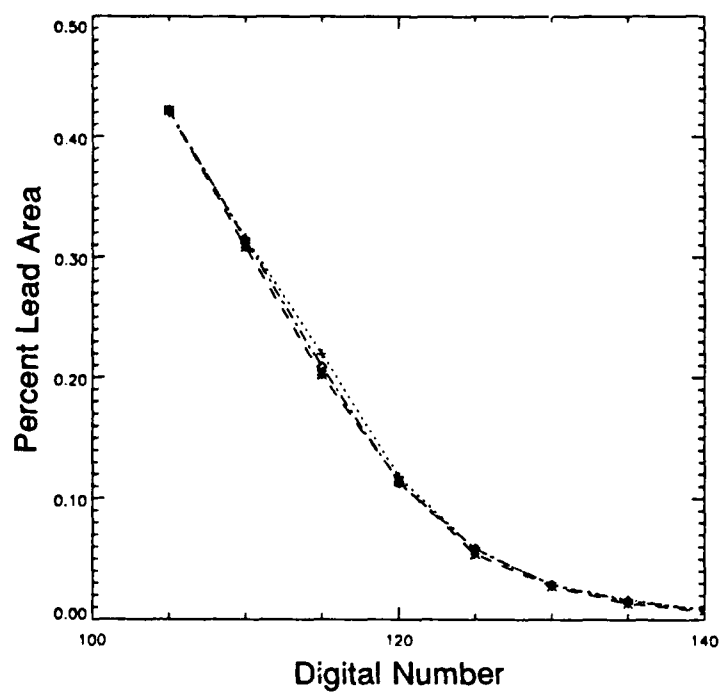
Fig. I.4. Change in percent lead area estimated in an AVHRR image as a function of resampling scheme and DN threshold.
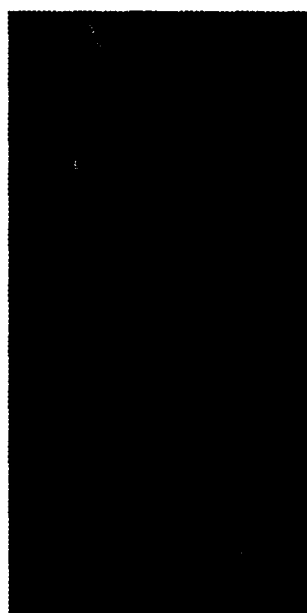
Fig. I.5. Synthetic images used to assess effects of resampling on different lead types.

A.

B.
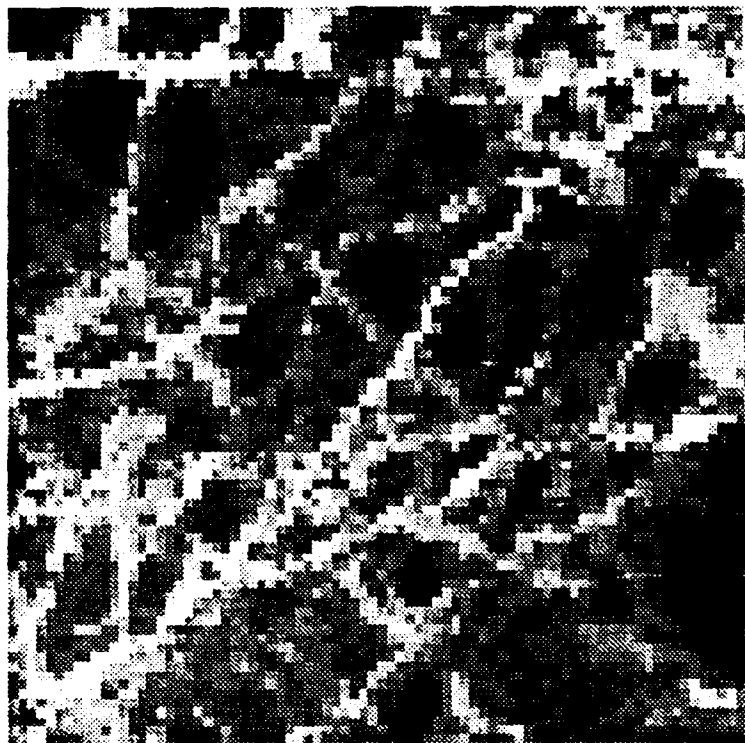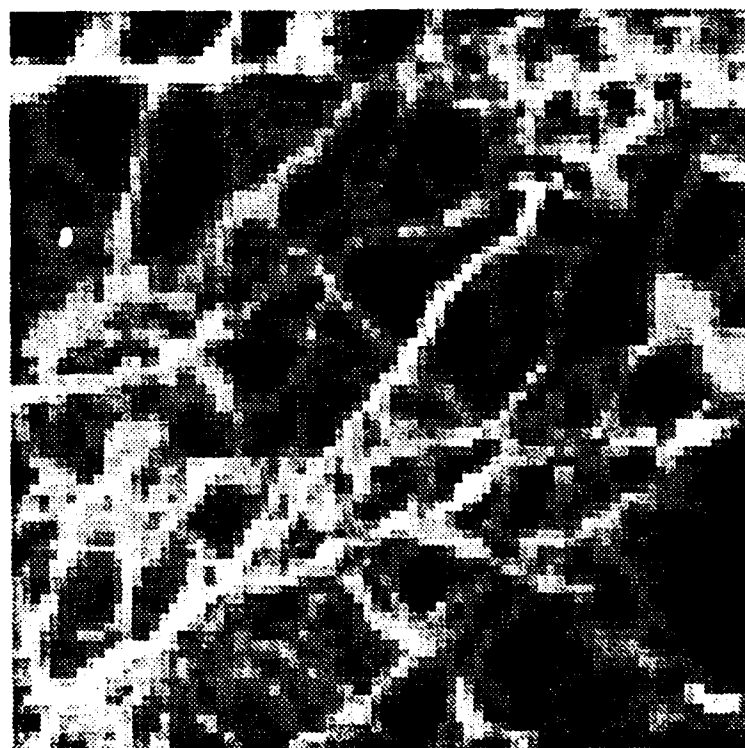
Fig. I.6. Effect of NN resampling on lead appearance in Landsat imagery (A), and reconstruction of lead appearance through the application of a spatial filter (B).
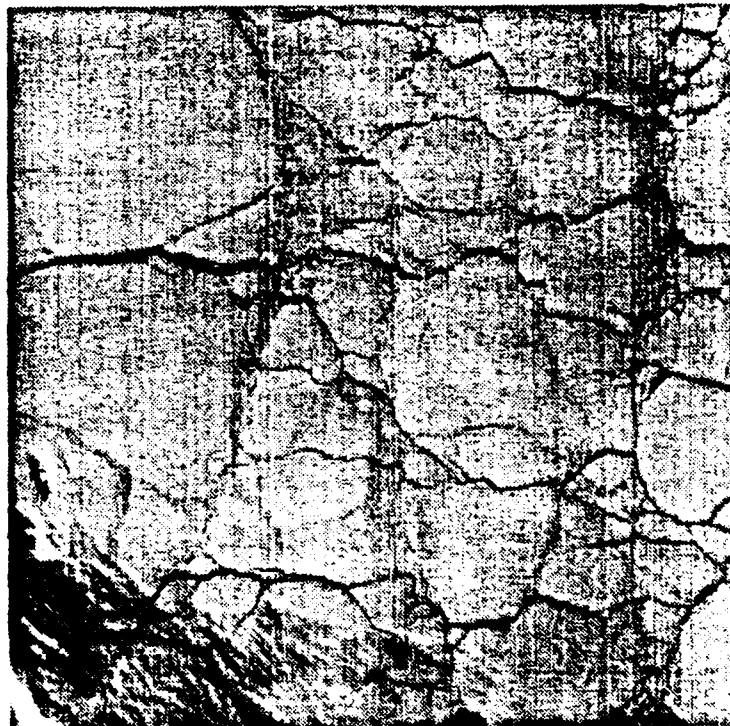
A.

B.

Fig. I.7. Colocated Landsat and AVHRR imagery for the Beaufort Sea, showing the representation of the same lead complex in the different image types.
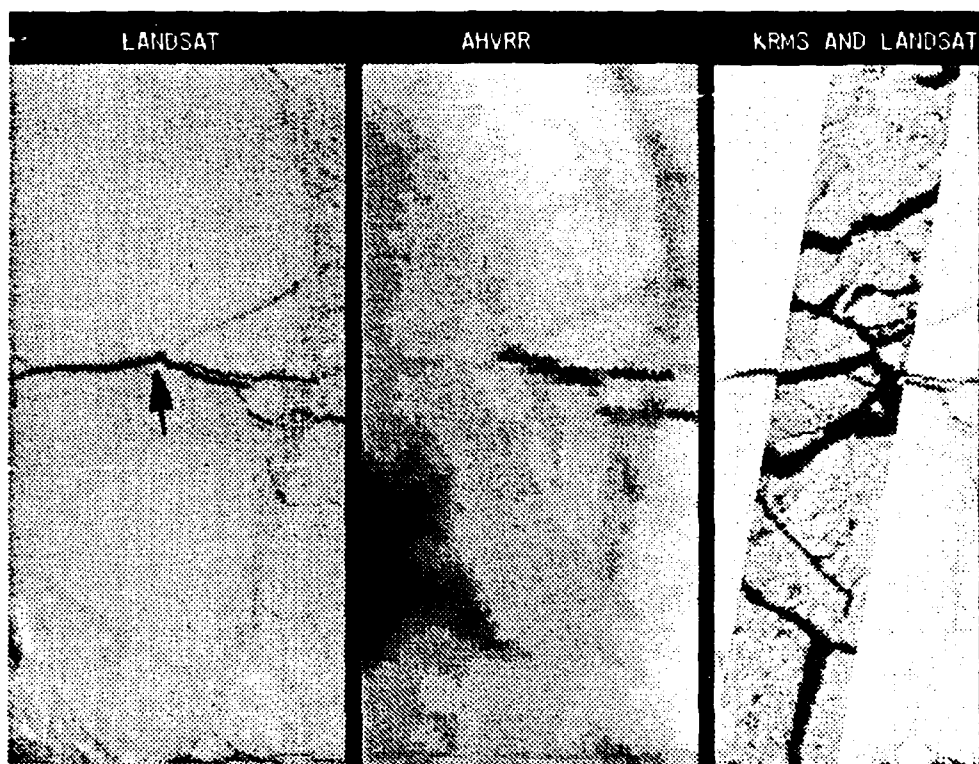
Fig. I.8. Colocated Landsat, AVHRR, and KRMS + Landsat imagery for the Beaufort Sea. The black arrowhead in the Landsat image marks the location of the lead and transect presented in Figure I.9.
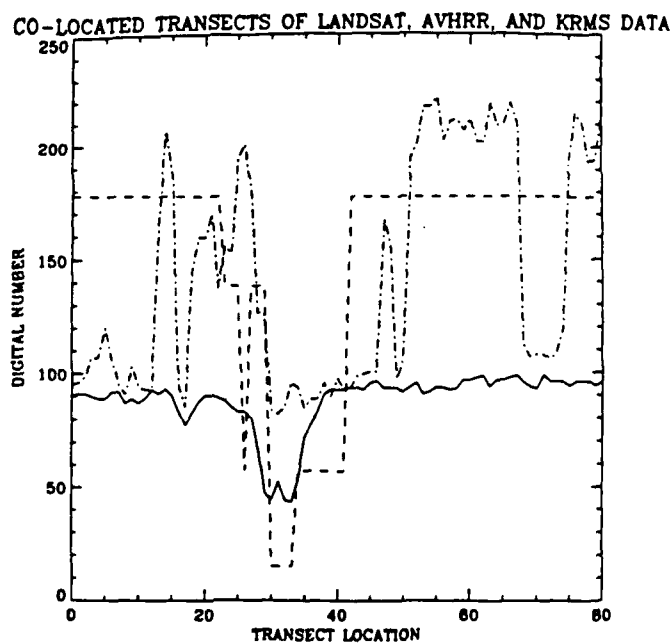
Fig. I.9. Transect through the imagery in Figure I.8.

I.2 THEORETICAL ANALYSIS OF THE EFFECT OF SENSOR RESOLUTION ON OBSERVED FRACTIONAL AREA COVERAGE

An analytical description of the relationship between the satellite-derived fractional area coverage of a geophysical field and sensor resolution is needed in order to assess the potential error in many satellite-derived products and to understand in a more quantitative manner the benefits of different sensor systems. While there have been studies of the effect of sensor resolution on parameter retrieval, the approaches have been empirical and specific to a single geophysical variable. In the analysis of land cover classes, for example, the variance within satellite images has been examined as a function of measurement scale for the purpose of determining the optimal resolution for change monitoring (e.g., *Woodcock and Strahler*, 1987; *Townshend and Justice*, 1988). In studies of cloud fraction, real and synthetic data containing cloud fields were degraded in resolution, and the fractional coverage was observed as a function of scale (e.g., *Wielicki and Parker*, 1992; *Wielicki and Welch*, 1986; *Shenk and Salomonson*, 1972).

Even though these studies are useful, no concise statement of the relationship between fractional coverage and sensor resolution has been given, so that the results are difficult to generalize to other geophysical fields. A complete analytical description of the problem is difficult at best, involving geometrical (viewing geometry), spectral (band location and width), radiometric (signal-to-noise ratio, quantization levels), and spatial (sensor resolution or pixel size) properties. In this section a first attempt at an analytical approach to the problem is described. We are concerned only with the fraction of the image area covered by some geophysical parameter; e.g., open water fraction. We take an approach similar to that of *Shenk and Solomonson* (1972) where cloud fields were simulated and the relationship between pixel size, cloud size, estimated area fraction and true area fraction were expressed for different thresholding operations. That work is extended, however, by generalizing the problem to any geophysical variable whose spatial structure can be described by its autocovariance function. Additionally, a specific probability density function is used as a model of the subpixel area fraction so that the results do not depend upon a given simulation. In this manner the results are applicable to a wide variety of geophysical fields including clouds, sea ice fractures ("leads"), and land cover classes. In the next section the analytical approach is described. The models are then applied to simulated fields of clouds and sea ice leads in a satellite image context.

I.2.1 ANALYTICAL APPROACH

Our goal is to determine the proportion of pixels in an image that have the characteristic of interest; e.g., the fraction that are cloudy or that are sea ice leads, etc., given some thresholding operation. This depends on the distribution of the subpixel area fraction, which is specified by its shape, mean and variance. The variance depends on the pixel size and the spatial structure of the geophysical parameter, described by its autocovariance function. The formalization that follows can be applied to virtually any geophysical parameter whose spatial distribution can be described in this manner.

Let $q(\mathbf{x})$ be a measurable property (e.g., temperature or reflectance) at a point whose position is represented by the location vector $\mathbf{x}$, and define ζ to be any condition on q. For example, ζ might be the condition $q(\mathbf{x}) < T_s\text{-}\delta$, where T_s is the surface temperature and δ is some threshold amount. The indicator function $I(\mathbf{x})$ in a square region R is equal to 1 if $q(\mathbf{x})$ satisfies ζ and 0 otherwise. The fractional coverage for which q satifies ζ is given by

$$P = A_R^{-2} \int_R I(x) \, dx \tag{1}$$

where A_R is the side length of R and is a normalizing factor. For the rest of the discussion R is a satellite image. The probability density function (pdf) of I is $f_I(1) = P$ and $f_I(0) = 1 - P$.

Now let $q_Z(y)$ be a measurable property of a pixel Z within R centered at location y (again, a vector). As measured by the sensor, q_Z would be an average over a pixel:

$$q_Z(y) = A_Z^{-2} \int_{Z(y)} q(x) \, dx$$

where A_Z is the side length of the pixel. An argument could be made for using the sensor point spread (transfer) function, but for simplicity a rectangular spatial response is assumed. The fractional area of R for which q_Z satisfies ζ is an estimate of the true fractional coverage and is

$$P' = N^{-1} \sum_R I_Z(y) \tag{2}$$

where N is the number of pixels in R and I_Z is the indicator function for the pixel based on q_Z, defined in the same way as is I (for a point) based on q. Our goal is to relate P' to P over a range of A_Z.

To determine P' analytically the probability density of I_Z must be known. It is not trivial, and depends on P, ζ, pixel size, and the way in which objects satisfying ζ are distributed in space. Since I_Z is a function of q_Z, which in turn depends on the fractional coverage within a pixel p_Z, then (under certain conditions) I_Z can be expressed in terms of p_Z. For example, consider a cloud pattern where the cloud top temperature T_c is everywhere the same and is less than the surface temperture T_s. Let ζ be a thresholding operation such that

$$I_Z = \begin{cases} 1 & \text{if } q_Z < T_s - \delta \\ 0 & \text{otherwise} \end{cases}$$

where δ is some threshold amount. This is equivalent to

$$I_Z = \begin{cases} 1 & \text{if } p_z \geq p \\ 0 & \text{otherwise} \end{cases} \tag{3}$$

The expression $p_Z \geq p$ states that the fractional coverage within the pixel is greater than some quantity p, which in this example has a value such that

$$(1-p)T_s + pT_c < T_s - \delta$$

In reality there may be a distribution of T_c, although we do not address this issue here. So, based on (3), the probability density of I_Z is

$$f_{I_z}(1) = \text{Prob}(P_Z \geq p)$$
$$f_{I_z}(0) = \text{Prob}(P_Z < p) = 1 - f_{I_z}(1)$$

where P_z represents the random variable subpixel fractional coverage (with specific realization p_z), and Prob($P_z \geq p$) represents the probability that the fractional coverage within the pixel is greater than some quantity p. Now, how is Prob($P_z \geq p$) determined?

For a single pixel the fractional coverage of the geophysical parameter is

$$p_z(y) = A_z^{-2} \int_{Z(y)} I(x) \, dx$$

which can be used as an estimate of the true area fraction in the image P. After *Stoyan et al.* (1989, pg. 184), the expected value and variance of P_z are

$$\mu = E(P_z) = P$$

(4)

$$\sigma^2 = \text{Var}(P_z) = E[P_z - E(P_z)]^2$$

$$= E\left\{[A_z^{-2} \int_Z I(x) \, dx - P][A_z^{-2} \int_Z I(x') \, dx' - P]\right\}$$

(5)

$$= A_z^{-4} \int_Z \int_Z k_I(\|x - x'\|) \, dx \, dx'$$

where k_I is the autocovariance function for the indicator function. The effect of pixel size on the autocovariance function has been studied by *Jupp et al.* (1988, 1989), although the autocovariance function in (5) does not depend on pixel size; i.e., it refers to the true underlying (point) autocovariance. The expression (5) for the variance of the subpixel area fraction can be expanded as

$$\sigma^2 = A_z^{-4} \int_0^{A\sqrt{2}} k_I(r) \, r\{A^2[2\pi - 8\xi(r)]$$

(6)

$$- 8Ar\sqrt{2}\cos[\pi/4 + \xi(r)] + 2r^2 \cos[2\xi(r)]\} \, dr$$

where

$$\xi(r) = \begin{cases} 0, & 0 \leq r \leq A \\ \dfrac{1}{4}\cos^{-1}\left[1 + \dfrac{2}{\sqrt{2} - 1}(1 - r/A)\right], & A < r \leq A\sqrt{2} \end{cases}$$

as given in *Rothrock and Thorndike* (1984, with a correction made here). This applies to a square pixel and an isotropic covariance function.

If a specific model distribution for P_z is assumed, with expected value and variance as defined above, then the density of the pixel indicator function is also known. Here we use the Beta distribution, a two-parameter density function defined over the closed interval $0 \leq p \leq 1$ that is often used as a model for proportions:

The two parameters can be determined by maximum likelihood estimation based on the mean and variance of the subpixel fractional coverage in (4) and (5) (Falls, 1974):

The shape of the distribution is related to the size of the pixel relative to the spatial structure (e.g.,

$$f_{beta}(p) = \begin{cases} p^{\gamma-1}(1-p)^{\beta-1} \; \dfrac{\Gamma(\gamma+\beta)}{\Gamma(\gamma)\Gamma(\beta)}, & \gamma, \beta > 0; \; 0 \le p \le 1 \\ 0, & \text{elsewhere} \end{cases}$$

$$\beta = \frac{1-\mu}{\sigma^2} \, [\mu(1-\mu) - \sigma^2]$$

$$\gamma = \frac{\mu\beta}{1-\mu}$$

wavelength) of the geophysical parameter. In the limiting case with very large pixels relative to the wavelength of cloud elements, for example, most pixels would have a similar subpixel cloud fraction and the variance would be very small. The distribution would therefore have a single peak. On the other hand, if the pixel size is very small then the likelihood of pixels being either completely overcast or completely clear increases, the variance of the subpixel area fraction increases, and two peaks are expected. This is illustrated in Figure I.10 where the beta distribution is shown for a mean area fraction of 0.2 and variances of 0.1, 0.05, and 0.01.

The beta distribution has often been used to describe cloud amount frequency distributions (e.g., *Falls*, 1974; *Henderson-Sellers and McGuffie*, 1991; *Jones*, 1992). More recently a similar distribution, the Burger distribution, has also been used (e.g., *Henderson-Sellers and McGuffie*, 1991). The Burger distribution is described by the mean cloud amount and a correlation distance defined as the separation distance between pixels at which the autocorrelation drops below 0.99. Correlation distance was also used by *Gringorten* (1979), who developed models through simulations describing the probability of a meteorological condition occupying some fraction of a line or area.

Jones (1992) presents a shape parameter that can be used to describe the beta distribution. It is defined as

$$S = \frac{\sigma}{[\mu(1-\mu)]^{\frac{1}{2}}}$$

$S > 0.6$ implies a U-shaped distribution, $S \approx 0.6$ implies a flat distribution, and $S < 0.6$ implies a distribution with a central peak. Values of the shape parameter are also shown in Figure I.10. In the examples that follow, and in most satellite remote sensing applications where pixel sizes are 1 km or less, $S > 0.6$.

Now we return to the estimate of the total area fraction in an image, P', which is the proportion of pixels in the image for which the indicator function takes on a value of 1, as defined in (2). Given the distribution of subpixel area fraction described here by the beta pdf, P' is simply $\text{Prob}(P_z \ge p)$ or the probability that the subpixel area fraction is greater than some threshold value p. This is the area under the curve to the right of any given value along the horizontal axis in Figure I.10.

Figure I.11 shows the estimated total area fraction for four true area fractions as a function of the subpixel area fraction variance (along the abscissa) and the threshold value. The variance and the true area fraction together define the distribution of subpixel area fraction so that a wide range of spatial structures and pixel sizes is represented in the three plots, independent of any particular geophysical field. For a given autocovariance function, pixel size decreases toward the right in the plots. Note that there is an

upper limit on the variance, defined by the point at which the two parameters of the beta distribution are equal to or less than 0. This point is $\mu-\mu^2$. In theory, decreasing the pixel size fraction. Results for three subpixel area fraction thresholds are shown.

Beta Distributions of Subpixel Area Coverage
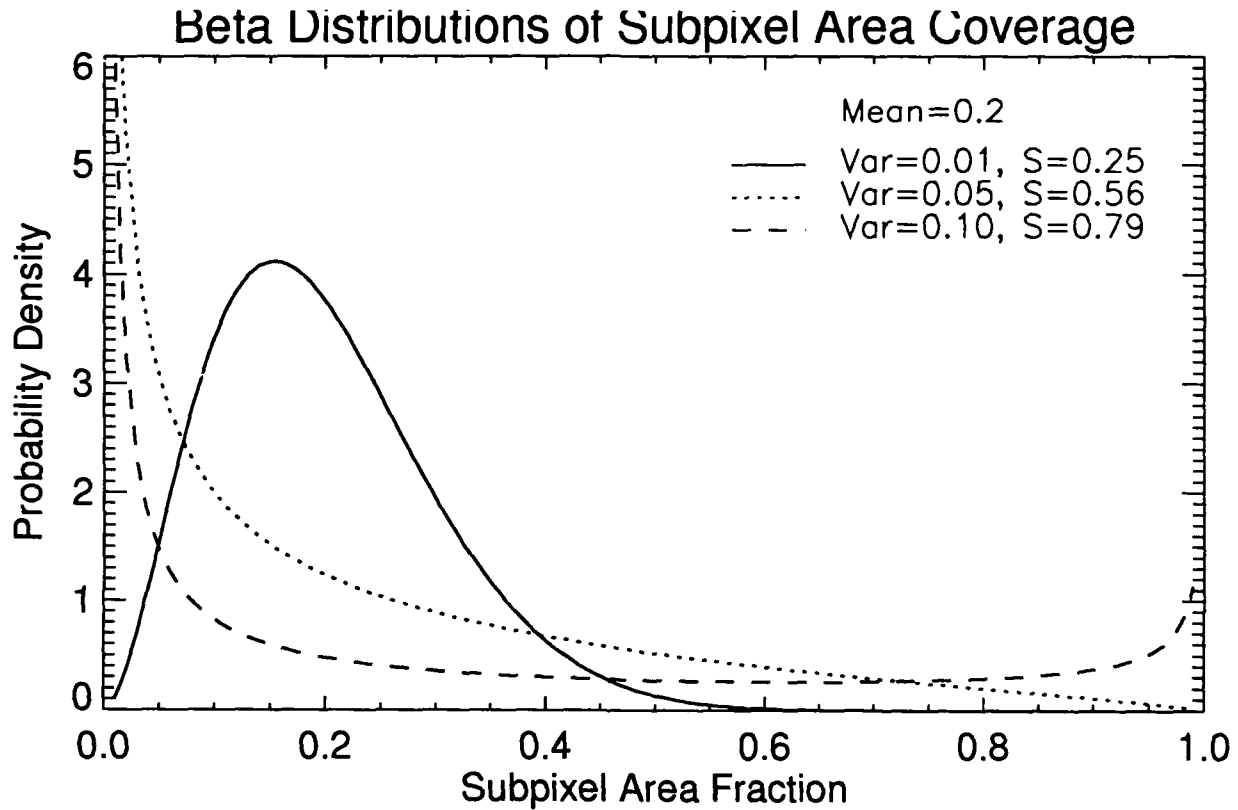
Fig. I.10. Three realizations of the Beta probability density function for a mean subpixel fractional coverage of 0.2 and three different variances. The shape parameter S is also given.
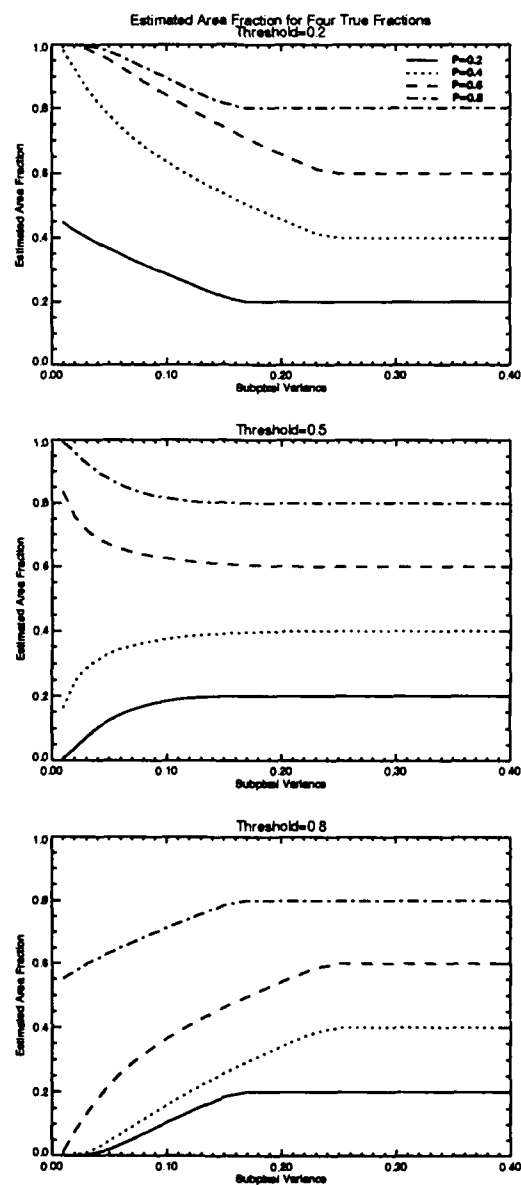
Fig. I.11. Estimated total area fraction as a function of the subpixel area fraction variance and true area fraction.

I.2.2. APPLICATION

Now we apply these models to simulated satellite data. Since these models require some *a priori* knowledge of the field's spatial structure, they cannot be used to assess the error in the total area fraction estimate from a single image alone. Instead, this section illustrates how the error can be assessed for typical realizations of two very different geophysical variables: clouds and sea ice leads.

A cloud field is simulated as a distribution of disks whose center locations follow a binomial point process and whose diameters are approximately normally distributed (in a true Gaussian distribution, negative diameters would be possible). One realization is shown in Figure I.12, where the mean diameter is 2000 m. Sea ice leads are modeled as a Poisson line process. The mean spacing between the lines (leads) is 3000 m and their orientations are random. The lines are assigned thicknesses (widths) following the negative exponential density function:

$$f_w(w) = \frac{1}{\lambda} e^{-w\lambda}$$

where w is lead width and λ is the mean width. For the simulations λ=200 m. One realization is shown in Figure I.13.

(increasing the variance) beyond this point has no effect on the estimate of the total area fraction.

To examine the effects of pixel size on the estimated fractional area coverage, these images were degraded by simple averaging of 2 x 2 pixel cells. Four degradations were perfomed. Initial pixel size is 50 m; pixel size doubles with each degradation so that the largest pixel examined is 800 m.

Exponential covariance is a reasonable model for many geophysical parameters and is used here:

$$k_i(r) = P(1-P) e^{-\alpha r}, \qquad r, \alpha \geq 0 \tag{7}$$

where α describes the dependence of the covariance on the separation distance r. Implicit in this expression is that $q(\mathbf{x})$ is isotropic. Using (7) in (6) gives

$$\sigma^2 = P(1-P) A_z^{-4} \int_0^{A/2} e^{-\alpha r} r \{ A^2[2\pi - 8\xi(r)]$$
$$-8Ar\sqrt{2} \cos[\pi/4 + \xi(r)] + 2r^2 \cos[2\xi(r)] \} \, dr \tag{8}$$

Note that the effects of area coverage and autocovariance (e.g., the size of objects and pixel size) separate out:

$$\frac{\sigma^2}{P(1-P)} = f(A),$$

which is essentially *Jones*'s (1992) shape parameter S. This is not strictly true for the correlation functions of the cloud and lead models employed here, but is still useful for the purposes of this paper. The parameter α in (7) and (8) can be determined from observed autocovariances by rewriting (7) in linear form:

$$\ln[k_{\!\wedge}\!(r)] \ = \ \ln[P(1-P)] - \alpha r \tag{9}$$

and solving by least squares regression. For the applications below, the parameter α is determined for three evenly spaced, parallel transects in the imagery and then averaged.

Table I.2 illustrates the application of the beta distribution and its estimated moments to the synthetic data in Figures I.12 and I.13. Listed are the pixel size relative to the smallest pixel (where the smallest pixel is 1), α determined from the image, the "true" area fraction P determined from the highest resolution image in which each pixel is either empty or completely full, the observed variance of the subpixel fractional coverage P_z, and the variance of P_z estimated by solving (8) numerically. The difference in the α values for the two different fields reflects their spatial structures where the (auto)covariance of the synthetic leads falls off more rapidly than that of the clouds. The true area fraction and the observed and estimated variances in Table I.2 for the cloud case were used to generate beta pdfs for comparison with the observed distribution of subpixel area fraction. The results are shown in Figure I.14 as the complement of the cummulative probability distribution function. End effects are due to binning procedures. Shown this way it is straightforward to determine the total fractional area coverage estimate P' of the image for any threshold. For example, in the top plot of Figure I.14, any threshold greater than 0.1 (in theory, any value greater than 0) would yield the same cloud area fraction: 0.25. With a larger pixel size, however, this is not the case (Figure I.14, bottom). A threshold of 0.2 produces a total area fraction of 0.33 while a threshold of 0.6 yields a total fraction of about 0.2.

Table I.2. Relative pixel size, the covariance parameter, true total area fraction, and the observed and estimated variances of the subpixel area fraction.

Image	A	α	P	Observed Var(P_z)		Estimated Var(P_z)[1]	
Clouds	1	0.05	0.246	0.185		0.178	
		16			0.133		0.124
Leads	1	0.15	0.033	0.032		0.029	
		16			0.010		0.011

[1] Estimated using (8).
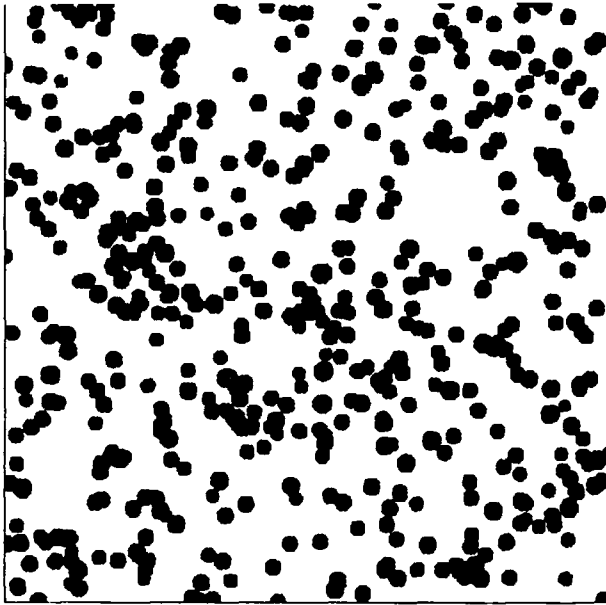
Fig. I.12. A simulated cloud field, where cloud centers follow a binomial point process and cloud diameters are Gaussian-distributed.
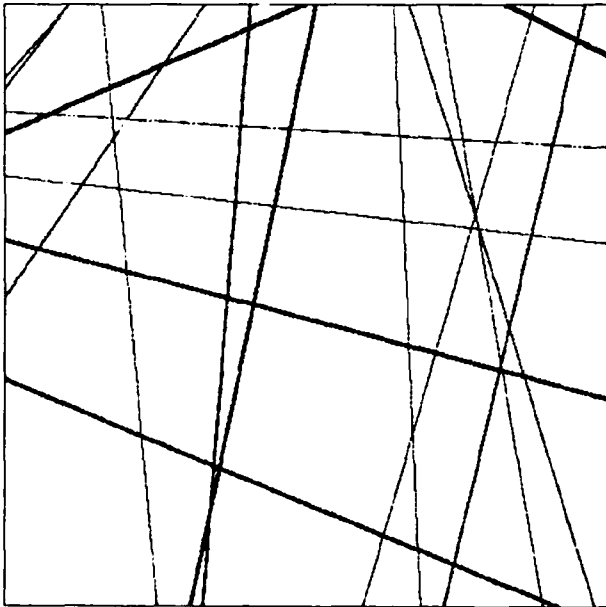
Fig. I.13. A Poisson line process, used to simulate linear openings in sea ice.

Fig. I.14. Complement of the cummulative probability function of subpixel area fraction for the cloud field in Figure I.12, using two different relative pixel sizes. Shown are the observed and estimated distributions, where the estimated functions are based on the true total area fraction and the observed and estimated variances in subpixel area fraction (Table I.2).
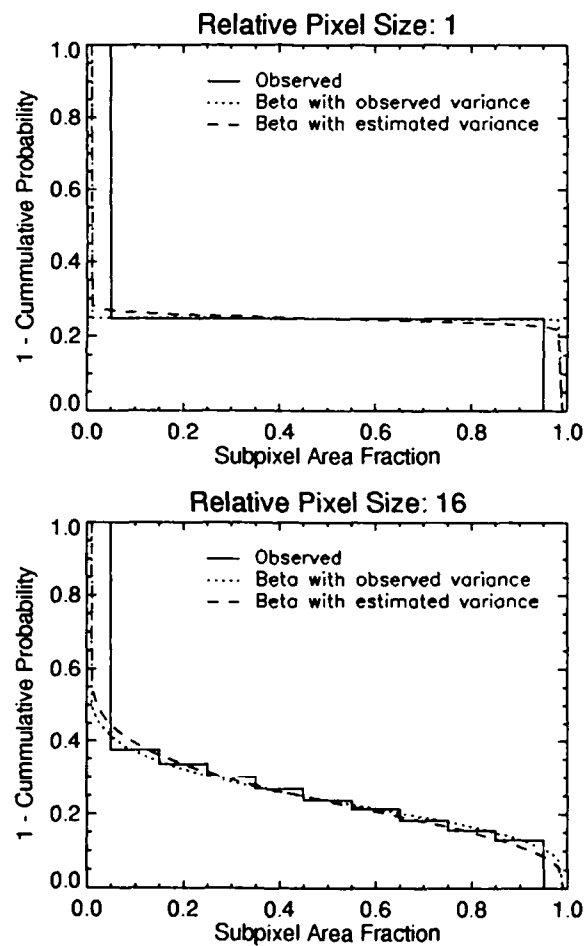
I.2.3 DISCUSSION

Except in the case of a uniform target and background, as with a single cloud deck over open water, it will generally not be possible to determine the subpixel area fraction and hence to apply the models presented here. For example, suppose thermal data are being examined for the purpose of estimating cloud fraction. Even if the background (land or ocean) temperature is known, a small deviation from that temperature in a pixel could be caused by a small amount of very cold cloud or a large amount of cloud only slightly colder than the background, or numerous other combinations of cloud amount, cloud optical thickness, and cloud top temperature. The problem is that a single threshold in terms of subpixel area fraction P_z can translate into a range of temperature thresholds and vice versa. In theory there is a single P_z threshold that would yield the same P' over a wide range of pixel sizes. This can be seen most readily in Figures I.10 and I.14. At the smallest pixel size the distribution of p_z is bimodal so that a range of thresholds would yield the same, correct P'; i.e., $P' = P$. At a large pixel size there may be only one correct threshold, but it is within the range found for the small pixel case. When dealing with DNs (temperatures, reflectances, etc.), however, this may not be the case. Further research is needed concerning the effect of "regularization", or the averaging over the point spread function of sensors. The work of *Jupp et al.* (1988, 1989) is important in this regard.

Given the pixel unmixing problem when the spectral structure of the field is complex, one way (perhaps the only way at present) to relate the DN threshold to the subpixel area fraction threshold is to choose a DN threshold very close to the background value. This is analogous to choosing a small subpixel area fraction threshold, as in the top plot of Figure I.11. If the pixel size is small enough relative to the spatial structure of the field, then P' will be a good estimate of P. If the pixel is not small, then all that can be said is that $P' \geq P$ see Figure I.11, top). How small is small?

To more easily address this and similar questions, Figure I.15 was constructed as an aid in the interpretation of (8). The figure shows the normalized variance as a function of relative pixel size A and the slope of the exponential covariance function α. The normalization was done by computing (8) without the $P(1-P)$ term so as to remove the dependence on P. Therefore, to use this figure the reported values must be multiplied by this term to retrieve the actual variance of the subpixel area fraction distribution. The two important relationships in (8) that are illustrated in Figure I.15 are that an increase in the pixel size or an increase in the rate at which the covariance drops off with distance both result in a decreasing variance. Not shown in Figure I.15 but implicit in (8) is the relationship between P and the variance: the variance of P_z is maximum when $P=0.5$ for a constant A and α.

Now if we interpret the previous condition that a DN threshold close in value to that of the background translates into a subpixel area fraction threshold of approximately 0.2 (for the purpose of illustration), then Figures I.11 and I.15 can be used together to answer "what if" questions. For example, suppose that the geophysical field had an exponential autocovariance with $\alpha=0.4$ and the true area fraction is 0.2. What would be the estimated total area fraction P' with a relative pixel size of 2? The variance based on Figure I.15 would then be approximately 0.11 and from Figure I.11 the estimated area fraction would be about 0.28 with a threshold of 0.2, 0.19 with a threshold of 0.5, and 0.12 with a threshold of 0.8. With a relative pixel size of 6 the variance is 0.056 and the area fraction estimates are 0.36, 0.13, and 0.02, respectively.

In theory a beta distribution that is consistent with the observed autocovariance function can be chosen. The regression method of estimating the rate of decay of the autocovariance described by (9) also provides an estimate of P. From these two parameters the variance in (8) is then determined, thereby defining the beta distribution. However, the autocovariance is affected by pixel size, as described in *Jupp et al.* (1988, 1989). Therefore, the autocovariance determined by (9) must be translated into the "true" (point) autocovariance before the correct beta distribution can be determined.

Fig. I.15. The variance of the distribution of subpixel area fraction computed from (8), normalized by $P(1-P)$, as a function of relative pixel size and the slope of the exponential covariance function α. To determine the actual variance, the contour value must be multiplied by $P(1-P)$.
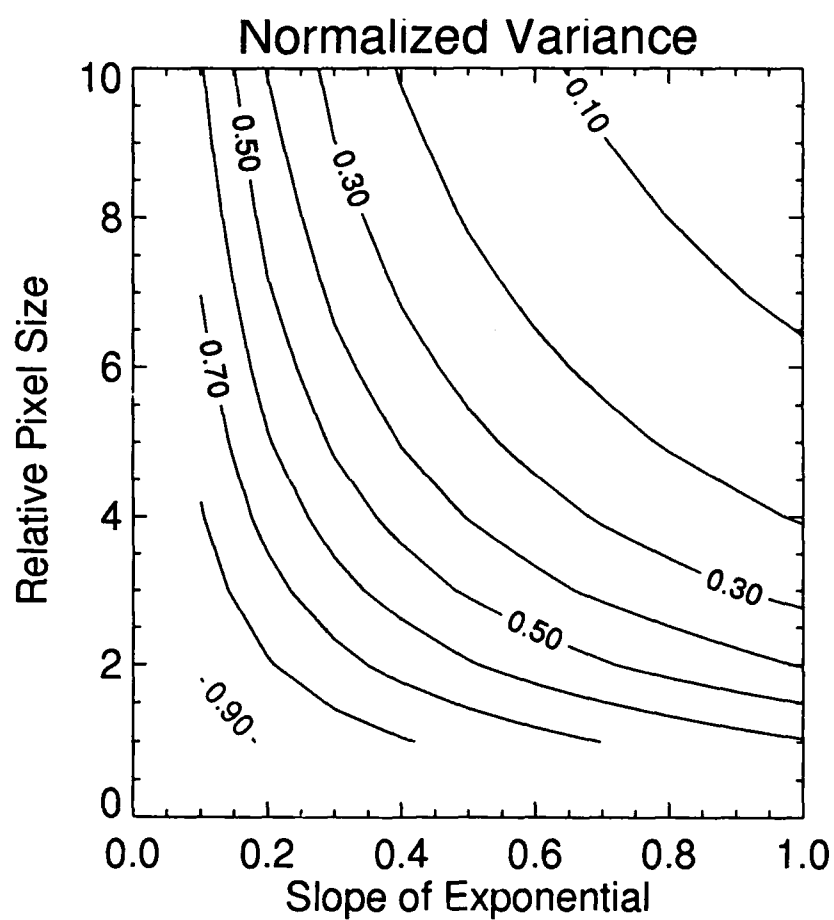
I.3 EMPIRICAL ANALYSIS OF THE EFFECT OF SENSOR RESOLUTION ON LEAD WIDTH DISTRIBUTIONS

The goal of this section is to begin to define the sources and magnitudes of errors in retrieved lead statistics as a function of the spatial resolutions of existing and future sensors, and to assess the importance of these errors in a physical context. Here we compare lead statistics retrieved from satellite imagery of varying spatial resolution, and we examine whether lead statistics derived from "medium" resolution imagery (e.g., a field-of-view of 500 - 1000 m) can be used to estimate characteristics of lead distributions that would be obtained from higher-resolution images with a field-of-view of about 80 m. The effects of atmospheric effects on the retrieval of lead geometries is examined in Section II and in *Stone and Key* (1993).

I.3.1 METHODS AND DATA

One way to investigate the effects of sensor field-of-view on retrieved lead statistics is to examine data from existing sensors of various spatial resolutions, an example of which is shown in Figure I.8. While the same general lead structure is apparent in the images, the smaller leads are obviously harder to detect in the AVHRR image than both the Landsat image and the KRMS data. In addition to the differences in spatial resolution, each sensor is sampling different spectral characteristics. For example, relatively thin ice forming within leads exhibits a low albedo and relatively high physical temperature, but the microwave brightness temperature differs dramatically from that of open water. In this example, the problems inherent in comparing lead statistics using imagery of different spatial resolutions and spectral characteristics is apparent: application of thresholds to the three data types yields 1.1% lead-covered area in the Landsat image, 12.8% in the AVHRR (which includes apparent low cloud with substantially warmer temperatures than the ice surface), and 5.4% lead-covered area in the KRMS image. Depending on which image type is used, these lead-fraction estimates would yield roughly an order of magnitude difference in the estimate of turbulent heat transported into the atmosphere from the warmer ocean.

While there are advantages to comparing lead statistics derived from different types of imagery, such a study is complicated by different acquisition times, spectral bands of the various sensors, and geolocation problems. To alleviate these sources of uncertainty, we choose to work with images of a single data type that are successively degraded in resolution by modeling the transfer function between the initial data and the desired resolution and then sub-sampling. A spatial filter that estimates the point spread function of the Landsat sensor is applied following the methodology presented in *Justice et al.* (1989). At each degradation cycle, Gaussian random noise is added back into the image to reduce the smoothing effects of the filtering operation.

We start with Landsat MSS band 4 (0.5-0.6 μm) scenes of the Beaufort Sea, March 1988, with an initial FOV of 80 m (Figure I.16). The fourth-order trend surface is removed from the original grey scale image (*Eppler and Full*, 1992) in order to correct for brightness variations caused by typically low sun angles in the Arctic. Images with FOVs of 160, 320, 640, and 1280 m are then created using the spatial filter. Each degradation is segmented using a threshold based on the Sobel operator edge detector. This procedure determines the discrete spatial gradient at each pixel in both dimensions. When its histogram is compared with that of the original image, the point of intersection determines an adequate cut-off between a lead and the ice. We note that the lead/not-lead decision is somewhat subjective; linear features from older, refrozen leads, for example, may or may not be included as leads. To differentiate between leads and other low-albedo features such as shadows and isolated open-water areas, valid lead fragments are identified using tests based on width and orientation.

Linearity is determined through correlation/regression analysis of pixels within the candidate features. Lead widths are measured perpendicular to the regression line, at 1 km intervals, and the slope of the regression line is the measure of the feature orientation.
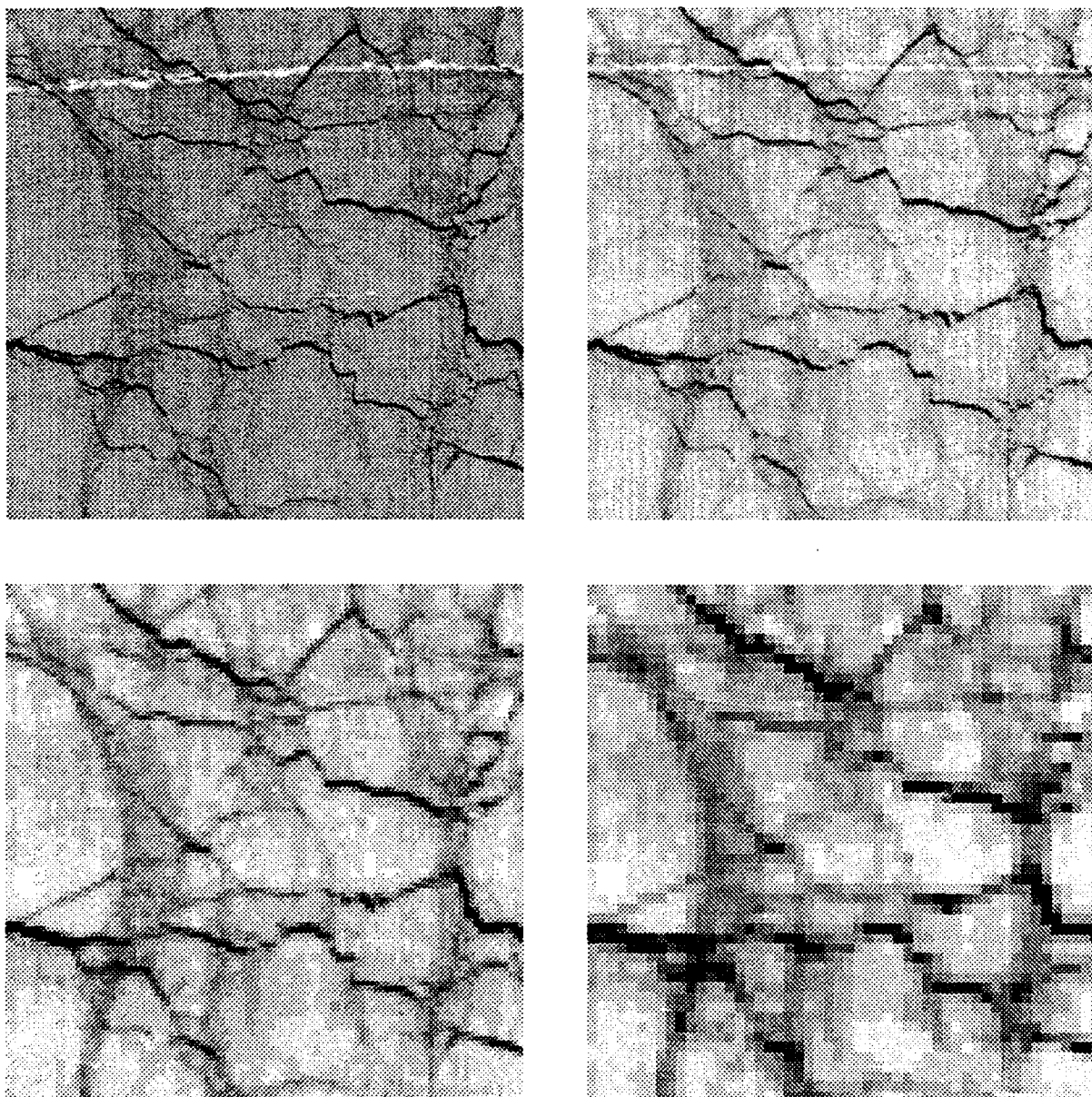

Fig. I.16. Landsat MSS band 4 scene of the ice pack north of Alaska in March 1988. Area covered in the images is approximately (80 km)^2. The degraded images have pixel sizes of 80 m (upper left), 160 m (upper right), 320 m (lower left), and 640 m (lower right).

In addition to the series of degraded-resolution Landsat images, "synthetic" images are generated as an additional tool to study the effects of spatial resolution on observed lead characteristics. These synthetic images represent lead networks as recorded in a thermal channel; e.g., leads and the surrounding ice are assigned different physical temperatures. The reason for using simulated leads is that their geometrical characteristics are completely known. Lead networks are simulated as a Poisson line process, where the mean spacing of lines (leads) is 2500 m and the orientations are random. The lines are assigned thicknesses (widths) following the negative exponential density function with mean width λ. For the simulations, $\lambda = 200$ m based on lead observations derived from submarine sonar data (e.g., Key and Peckham, 1992). For this stage of the study, leads can consist of either open water or thin ice within the surrounding matrix of thick ice. Three ice thicknesses are used: 0 (open water), 5, and 15 cm; the surrounding thick ice has a thickness of 2 m. Corresponding temperatures are 271, 256, 248, and 235 K. In the simulation, ice thicknesses within leads are assigned probabilities consistent with ice thickness distributions reported by *Maykut* (1982). One realization of the Poisson line process is shown in Figure I.17. The initial pixel size is 137.5 m, assigned so that the pixel size after the third degradation is 1.1 km, the nominal FOV of the AVHRR sensor at nadir.

I.3.2 OBSERVED CHANGES IN LEAD GEOMETRIES WITH FIELD-OF-VIEW

The distribution of lead widths corresponding to the images in Figure I.16 (degraded-resolution Landsat imagery) is shown in Figure I.18. The disappearance of small leads due to reduction in contrast and the apparent increase in the relative frequency of large leads as pixel size increases can readily be seen. In this particular Landsat sample, we find that leads narrower than approximately 250 m disappear as the resolution of the Landsat image is degraded to 320 and 640 m. However, the criteria for how a given lead will "grow" in width or disappear during image degradation depends on contrast in reflectance of the lead compared to that of the surrounding ice. For example, a narrow, open-water lead might increase in apparent width while decreasing in contrast as pixel size increases during the first degradation. However, in the subsequent degradation, the lead may "disappear" as the averaging of the sub-resolution lead and the surrounding ice raises the pixel reflectance above a given threshold. A narrow refrozen lead, in comparison, might disappear during the first degradation since the brightness contrast between the thin ice in the lead (rather than open water in the previous case) and the surrounding ice is initially smaller.

Orientations of leads can also be expected to change if the orientations are anisotropic (i.e., have a preferred orientation). An illustration of this is shown in Figure I.19 for the Landsat image in Figure I.16. Results from other Landsat scenes show similar patterns and are therefore not shown. Lead widths and orientations from the simulated lead networks (e.g., Figure I.17) exhibit similar dependencies on pixel size although orientations do not change substantially as with the real data since the basic pattern is isotropic.

Figure I.20 shows the change in mean lead width as a function of field-of-view for six Landsat images. We find that while the manner in which widths of individual leads changes is highly variable, the mean lead width, averaged over the entire image, seems to change in a more predictable way. This is a potentially important property since "true" mean lead widths might then be predicted based on measurements from a lower-resolution sensor.

The change in total lead areal coverage as a function of field-of-view is illustrated in Figure I.21 for the six Landsat images. The change in area fraction with increasing pixel size is generally exponential. The actual rate of change is, however, sensitive to the threshold levels used. In fact, it can be shown that lead area fraction may either increase or decrease with increasing pixel size depending on the threshold used. However, when the same thresholding method is used the lead fraction difference between degradation cycles varies in a predictable way. In other words, though the definition of a "lead" in the original image is still subjective, once defined it remains consistent throughout the range of degradations.
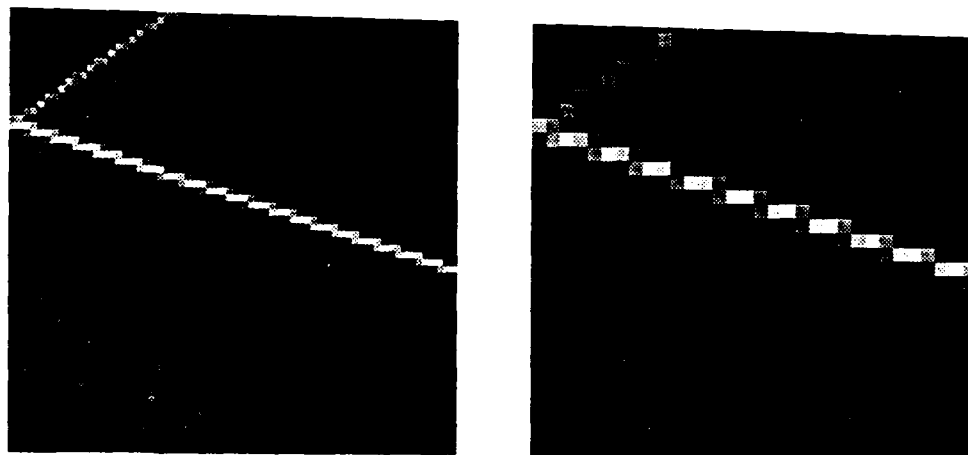
Fig. I.17. One realization of a lead network simulated by a Poisson line process with thick lines. Pixels sizes are 137.5 m (upper left), 275 m (upper right), 550 m (lower left), and 1100 m (lower right). Grey-scale values represent brightness temperatures.
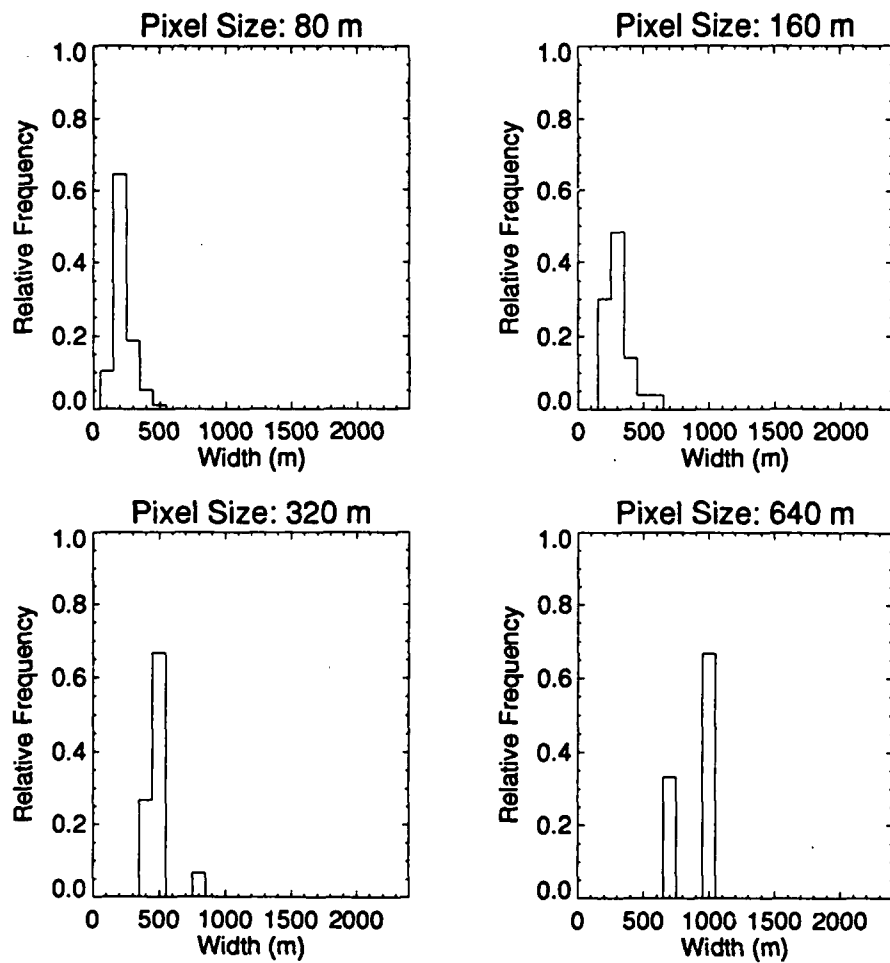
Fig. I.18. Lead width distributions for the Landsat image series in Figure I.16. Widths are grouped in 100 m bins.
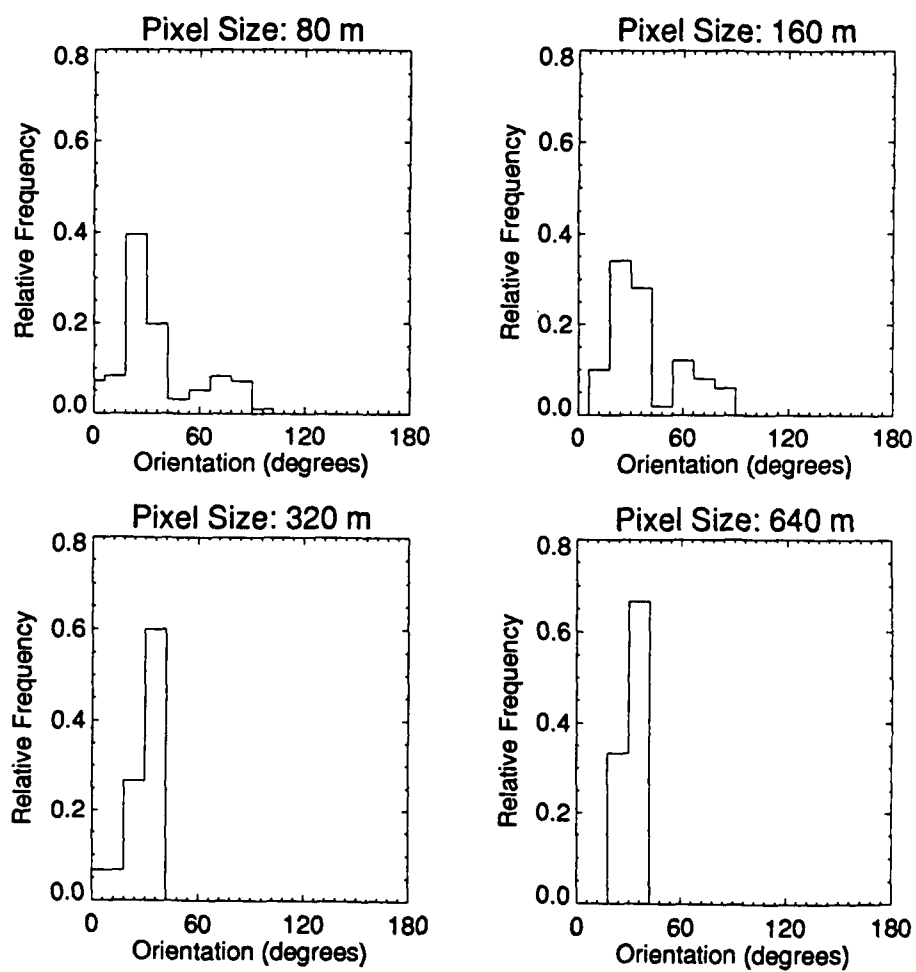
Fig. I.19. Lead orientations for the degraded Landsat series shown in Figure I.16. Orientation is the angle that a lead makes with the horizontal axis, measured counterclockwise.
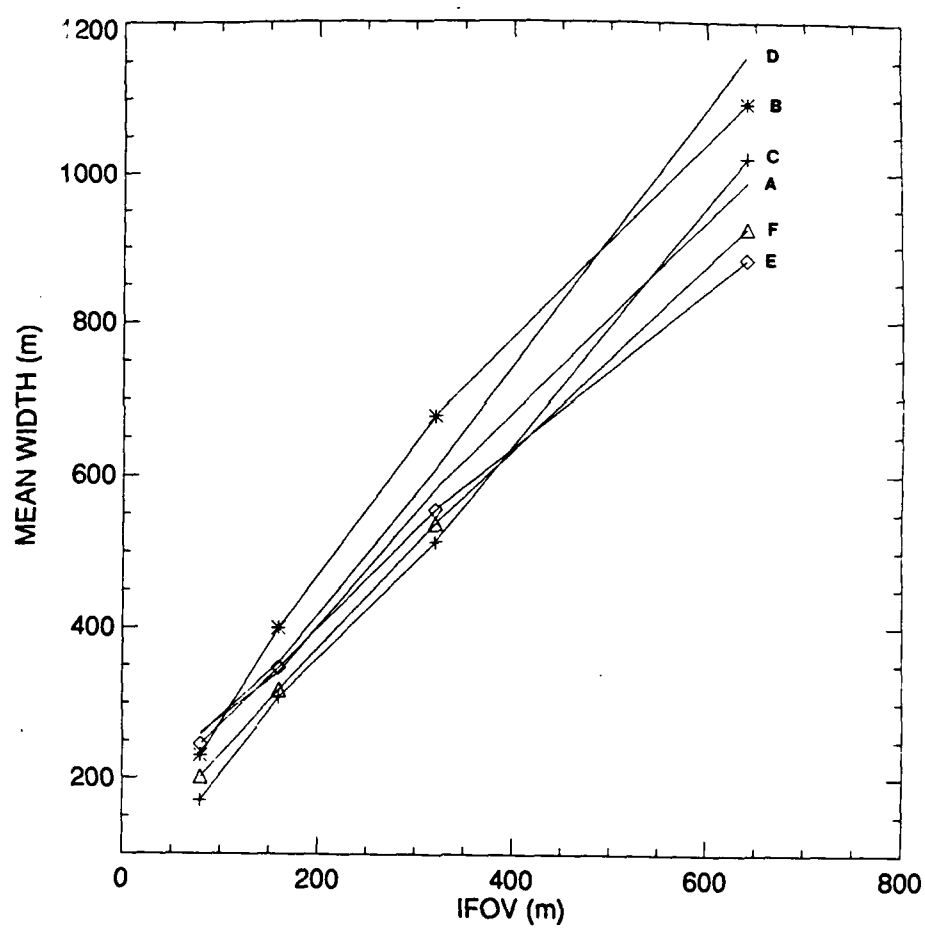
Fig. I.20. Change in mean lead width as a function of field-of-view for six Landsat images.
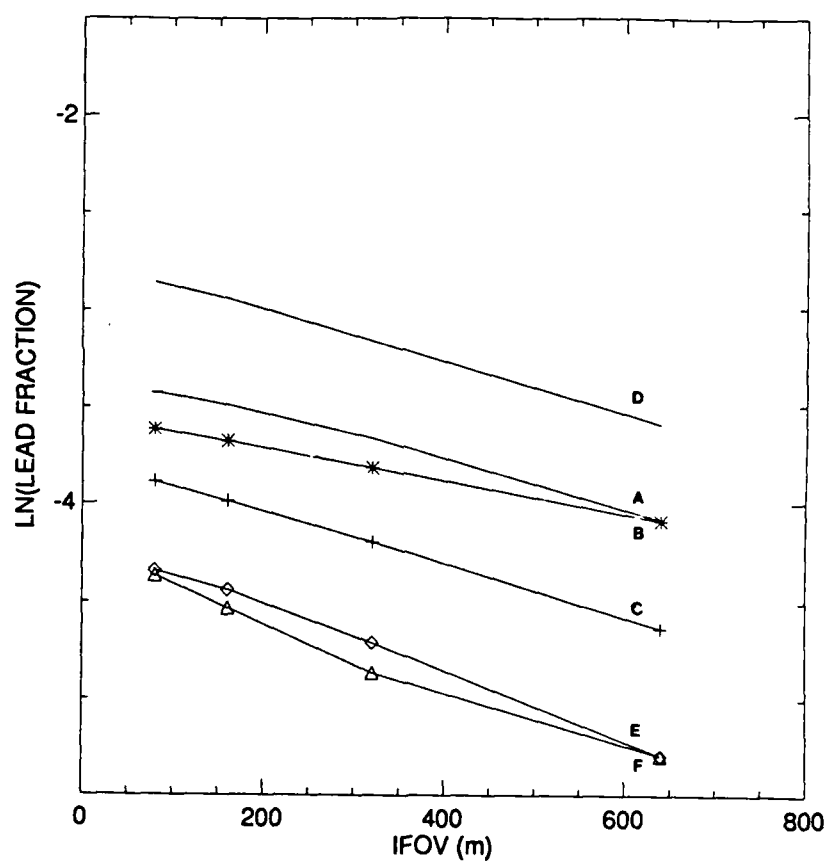
Fig. I.21. Change in total lead fractional area as a function of field-of-view for six Landsat images.

I.3.3 CONTRAST EFFECTS AND THRESHOLD SELECTION

The reason for the change in lead geometrical characteristics with sensor resolution is now examined in terms of contrast. We define the *normalized contrast* as a ratio based on the target and background temperatures, T_T and T_B:

$$C = \frac{T_T - T_B}{T_B}$$

Of course, the contrast ratio need not be defined in terms of temperature, so that T_T and T_B could also be reflectance or digital number (DN). Letting p be the fractional area coverage of a lead in a pixel; e.g., width/FOV, then the *total contrast* which takes into account the reduction in temperature contrast as a function of pixel size is

$$C_{tot} = \frac{[pT_T + (1-p)T_B] - T_B}{T_B}$$
$$= pC$$

The change in total contrast can be seen in Figure I.16, and is shown in more detail in Figure I.22 where four individual leads, each with a different initial contrast, are placed in an image context. The lead at the top of the figure has the lowest initial contrast. The images are degraded as described previously, with noise added initially and at each degradation. The change in the total contrast of each lead from one degradation to the next is shown in Figure I.23.

If every pixel in the image is to be labeled as either a lead pixel or not a lead pixel, then some thresholding operation must be used. One possible method is to choose as a threshold the background temperature plus some multiple of its variability σ, say $T_B + 2\sigma$. This threshold can also be expressed as a unitless contrast ratio:

$$\gamma = \frac{2\sigma}{T_B}$$

If the total contrast of a pixel is below this value, then the pixel is not a lead pixel. This threshold contrast includes implicitly the effect of the fractional area coverage of a lead within the pixel. It can be used to determine the minimum initial contrast, or *critical contrast*, necessary for a lead of a given width in a pixel of a given size to be detectable:

$$C^* = \frac{C_{tot}^*}{p}$$

where the asterisk represents a critical (cutoff) value and $C_{tot}^* = \gamma$.

Figure I.24 shows total contrast as a function of the initial contrast and the width/FOV ratio of leads; i.e., the combinations of the later two variables that give rise to a specific total contrast. For example, an initial contrast of 0.15 and a p (width/FOV) of 0.15 yields the same total contrast (0.02) as an initial contrast of 0.05 and a p of 0.4. The total contrast can also be considered as the threshold

contrast in that any point below a contour chosen as the threshold contrast represents a lead that is not detectable. For example, given a background ice temperature of 240 K with a standard deviation of 5 K, the threshold contrast as defined above is 0.042. If there exists a lead that is 500 m wide passing through a 1 km pixel, (so $p = 0.5$) then its initial contrast must be at least 0.084 (which is its critical contrast) for it to be detected. Given a background temperature of 240 K, this critical contrast translates into a lead temperature of 260.2 K.
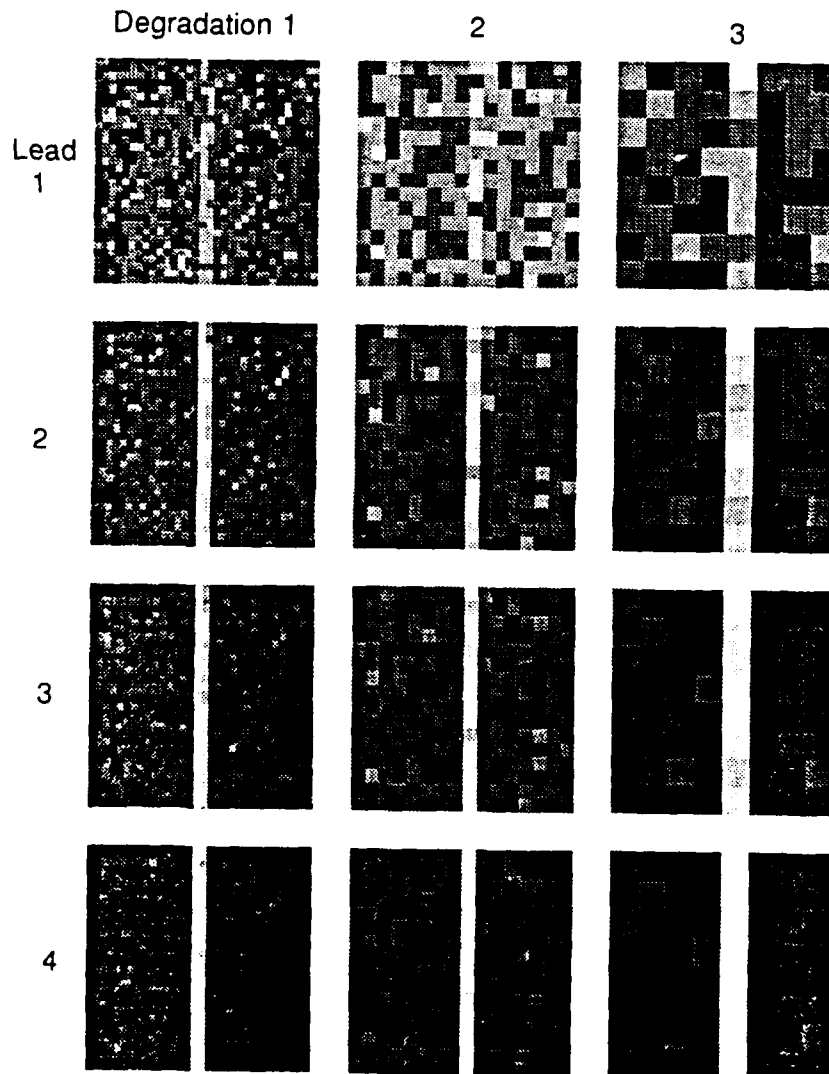
Fig. I.22. Four single-lead images of varying initial contrast (not shown) degraded three times. Initial lead width is one pixel. Gaussian noise is added after each degradation.
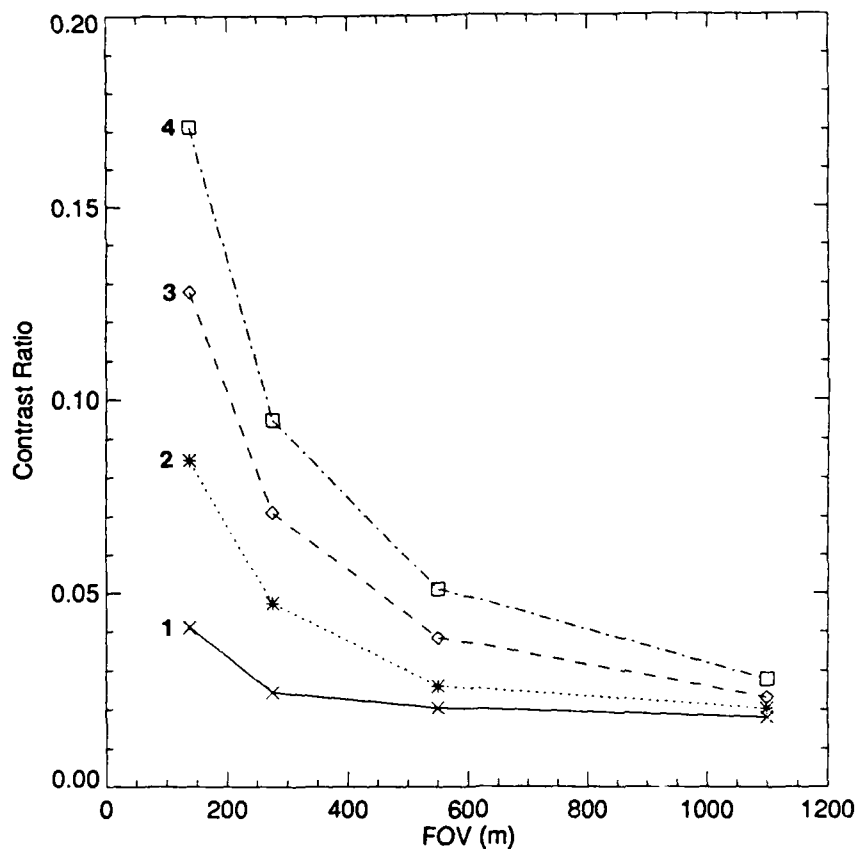
Fig. I.23. Total contrast as a function of field-of-view for the four leads in Figure I.8.
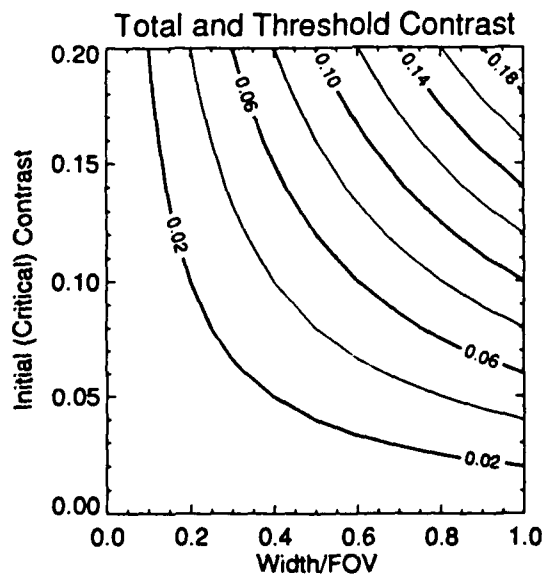
Fig. I.24. Total contrast as a function of the initial contrast and the width/FOV ratio of leads; i.e., the combinations of the later two variables that give rise to a specific total contrast. The total contrast can also be treated as the threshold contrast in that any point below a contour chosen as the threshold contrast represents a le. that is not detectable.

I.3.4 EFFECTS OF CHANGES IN FIELD-OF-VIEW ON TURBULENT HEAT FLUX

As noted in previous sections, image characteristics affect the retrieval of lead width distributions as well as total lead area. To quantify the effects of these image characteristics, we calculate turbulent heat flux as a function of lead area and lead width. Changes in both the mean lead width and lead-covered area are considered in the calculation of sensible and latent heat flux as a function of fetch (treated here as the lead width), surface temperature, air temperature, and wind speed using the procedure outlined by *Andreas and Murphy* (1986). In this approach, a bulk Richardson number defines atmospheric stability that controls convective turbulence based on temperature and wind speed. Convective turbulence combines with the mechanical mixing introduced by the step effect of an air mass in equilibrium with thick sea-ice conditions travelling over the physically rough edge of a lead and the considerably warmer open water or thin ice in the lead. The addition of mechanical turbulence introduced by the ice-lead boundary tends to result in a higher rate of heat transfer from smaller leads compared to larger leads. Thus, for a given areal coverage of leads in an image, a greater number of smaller leads will result in more heat loss to the atmosphere than from a lesser number of larger leads, even though the total amount of open water in the image remains the same. Under the conditions examined by *Andreas and Murphy* (1986), this decrease in flux as lead width increases becomes negligible for lead widths greater than about 200 m.

To illustrate the effects of changes in lead statistics using different image fields-of-view, we calculate sensible and latent heat flux using the above approach for the data presented in Figure I.20 and the associated changes in lead areal coverage in Figure I.21. An open-water temperature of $-1.8°$ C, wind speed of 5 m s^{-1}, air temperatures of $-28.9°$ C at a reference height of 2 m, ocean salinity of 34 ppt, air pressure of 1000 mb, and a neutral-stability drag coefficient of 1.49 x 10^{-3} are used to represent typical mid-winter (January) conditions over the Arctic sea ice pack (Maykut, 1978; Andreas and Murphy, 1986). Although leads are often covered by thin ice rather than open water and thus have a lower surface temperature than open water, the assumption that the leads are not refrozen and have a surface temperature of $-1.8°$ C is a useful baseline for our calculations. Turbulent (sensible plus latent) heat flux from leads is calculated using the mean lead width at each field of view and then weighted by the areal coverage ~f leads for the six MSS images used in Figures I.20 and I.21 to yield an areally-averaged heat flux. Turbulent fluxes from open-water leads under these conditions are around 300 Wm^{-2} compared to a flux of nearly 0 from surrounding ice taken to be three meters thick. Thus, lead fraction and lead width dominate the transfer of turbulent heat through the ice pack during winter. Table I.3 shows these areal averages for the six MSS images. Since the effect of increasing the fields-of-view in these examples is to decrease the apparent lead fraction, areally-averaged fluxes decrease as field-of-view increases. However, as noted earlier, the choice of thresholds can affects both the magnitude and direction of change in lead statistics with changing FOV. If we assume that the lead widths and lead fractions measured using the 80 m FOV imagery are closest to reality, then the errors introduced by using lead widths and lead fraction measured at a 640 m FOV are substantial - averaging 45% over the six images. Since the change in turbulent heat transfer with changing lead width is greatest for smaller leads, those images with smallest mean lead widths at the 80 m FOV (such as Images C and F) are most affected. In the images studied here, where the mean lead width is fairly large, the effect of errors in lead fraction is about five times that of the effect of uncertainty in lead width.

Table I.3. Areally averaged turbulent (sensible + latent) flux (in Wm^{-2}) for typical January conditions as a function of field of view for six MSS images. The percent change in the flux between FOVs of 80 m and 640 m is also shown.

			Image			
FOV (m)	A	B	C	D	E	F
80	23.5	19.1	17.4	50.7	10.6	15.0
160	22.2	17.7	14.4	47.0	9.7	12.1
320	19.9	16.1	11.7	41.6	8.2	8.9
640	16.7	14.0	7.9	33.7	5.6	5.3
% change	29	27	55	34	47	65

I.3.5 TRANSLATION BETWEEN SCALES

From the previous discussions it is obvious that lead statistics change significantly as a function of field-of-view, and that there are important implications of these changes for large-area turbulent heat flux estimates. Is there any possibility of estimating the true lead widths and area fractions from those observed in lower-resolution imagery?

I.3.5.1 Width Distributions

Given that very small features will generally not be resolved, the issue then becomes one concerning the possibility of using the distribution of lead widths measured at low resolution to estimate the complete or "true" distribution. For example, assume that lead widths x follow a negative exponential distribution with an unknown mean λ. From a sampling point of view it is useful to treat the distribution of widths as discrete and address the number n_i of leads in bin i that have widths between x_i and x_i+w:

$$n_i = \frac{Nw}{\lambda}e^{-x_i/\lambda} \tag{10}$$

where w is the width of the bin and N is the unknown total number of leads in the spatial area. The idea is that n_i is measured for a few bins, and that λ and N are estimated. To accomplish this, (10) is rewritten in linear form as

$$\ln(n_i) = \ln(\frac{Nw}{\lambda}) - \frac{1}{\lambda}x_i \tag{11}$$

Letting $a = \ln(Nw/\lambda)$ and $b = \lambda^{-1}$ and solving for a and b by the method of least squares with the observed data, the mean of the distribution and the total number of leads can then be estimated.

Experiments with this model show it to be very sensitive to the bin width and the number of bins in which leads actually occur in the lower-resolution imagery. This is not unexpected considering that

the entire range of x is being estimated in the least squares model by observations in only one part of its range. A more fundamental problem exists with this method: as shown earlier, the widths of the leads observed in the lower-resolution data are probably not the true widths of those leads. Figure I.25 illustrates the problem where the actual lead width distribution - which is exponential - in the simulated leads image of Figure I.17 is estimated using the above method and the observations from each degraded image. Significant departures from the actual distribution are obvious.
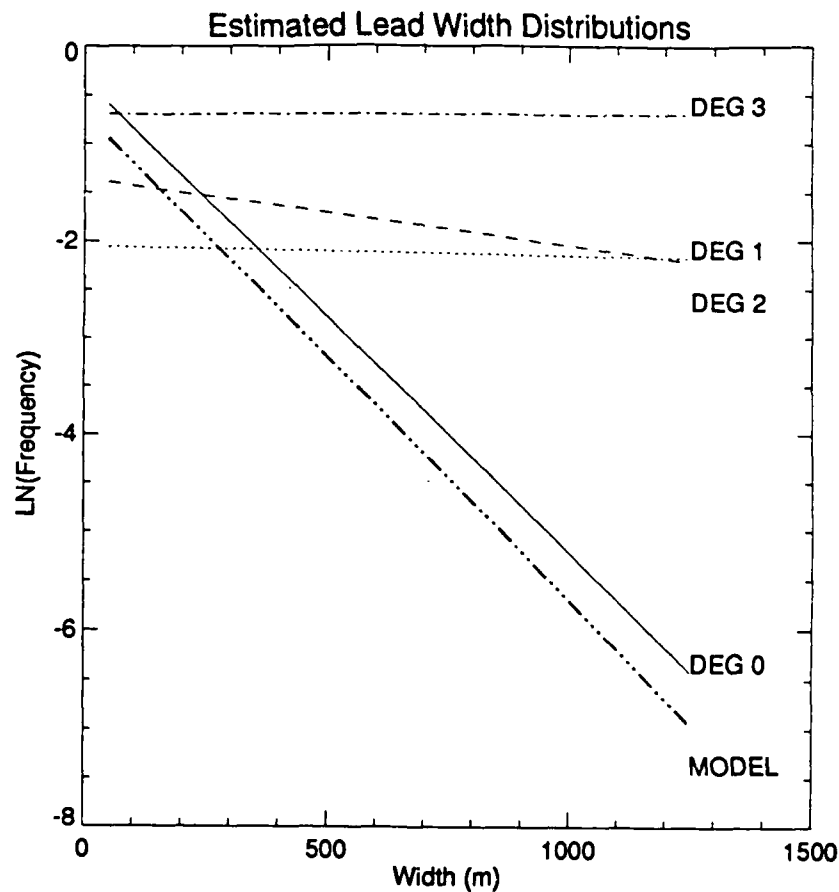
Estimated Lead Width Distributions

Fig. I.25. Estimated actual width distributions from observed lead widths at each field-of-view or degradation (DEG0-DEG3) of the simulated lead network shown in Figure I.17. Also shown is the model distribution used to generate the leads in the image.

Is it possible to unmix the pixels and thereby obtain the true lead widths? Using a single spectral band, it is not possible when ice of different thicknesses, and thus different reflectances and surface temperatures, are present in the field-of-view. For a brief time during the summer when new ice is not forming in the leads, the percentage of open water within the FOV can be calculated with a single spectral band since all leads can be assumed to contain only open water and therefore essentially the same reflectance or temperature. During the winter when no visible-band data are available, no unmixing is possible since leads can consist of a large range of ice thicknesses. During the spring and fall months the problem can, in theory, be solved using one thermal and one visible-band observation and an energy balance approach as follows. The total contrast of a lead pixel in both a thermal and a visible-band image of the same lead are observed. The mean background (ice) temperature and albedo, T_B and α_B are determined from the data. This leaves two equations with three unknowns:

$$C_{tot,IR} = p\frac{T_T - T_B}{T_B}$$

$$C_{tot,Vis} = p\frac{\alpha_T - \alpha_B}{\alpha_B}$$

Actually, the target (lead) temperature and albedo are physically related, although the relationship is a complex one. An energy balance model is used to determine the target albedo for a given target temperature (Maykut, 1982):

$$(1 - \alpha_T)F_r - I_{ice} + F_L + \varepsilon \ \sigma T_T^4 + F_s + F_e + F_c = 0$$

where α is the albedo, ε is the longwave emissivity, σ is the Stefan-Boltzmann constant, I_{ice} is the amount of shortwave energy that penetrates the ice and does not directly heat the surface, F_r and F_l are the downwelling shortwave and longwave radiation, F_s and F_e are the sensible and latent heat fluxes, and F_c is the conductive heat flux. A flux toward the surface is positive. The energy balance equation is solved for a range of possible target temperatures, $T_B \leq T_T \leq 273.15$ K, until a combination of p, T_T, and α_T is found that is consistent with the observed total contrasts.

While in theory this method will work, in practice it would be difficult to accurately estimate all the necessary parameters. It is not our purpose here to present methods of retrieving these parameters, but instead we summarize the potential error through an example of the sensitivity of the energy balance approach: if the target albedo α_T can be estimated to within 0.05, for example, the range of p that could satisfy the above equations is 0.455 to 0.556 for $\alpha_B = 0.7$, a true p of 0.5 and a true α_T of 0.2. With a 1 km FOV this translates into a range in lead widths of 445 to 556 m, where the true width is 500 m. While the use of physical models can help the unmixing process, we do not expect that we will ever be able to fully resolve the mixture components with existing data.

As can be seen in Figure I.20, however, the unmixing of pixels to determine the actual lead widths observed may not be necessary. The fact that the mean lead widths change in a predictable way with increasing pixel size implies that the mean of the width distribution measured at one field-of-view can be used to estimate the mean width at another field-of-view. Even though the rate of change of mean lead width with pixel size depends on the threshold used (not shown), the relationship is approximately linear for a given thresholding operation. This relationship can be utilized as follows. For an image at a given field-of-view, determine the mean lead width. Degrade the image and once again determine the mean lead width using the same thresholding operation as before. The two points define a line analogous to those in Figure I.20. The mean lead width at a narrower FOV can then be determined and applied in (11).

Of course the relationship is not perfectly linear, so that some error in the predicted mean lead

width can be expected. As an example, we consider the two images with the smallest and greatest error in turbulent heat flux due to FOV, as given in Table I.3, images B and F. The relationships for these two images are among the most nonlinear of those examined. For image B the mean lead width at a pixel size of 320 m is 680 m; degrading that image to a 640 m pixel size would yield a mean lead width of approximately 1080 m, also as indicated. If these two points were then used to extrapolate back to a FOV of 80 m, the estimated lead width would be 360 m as opposed to the 231 m value actually measured in the imagery. The difference between the turbulent flux calculated for a single lead (no area-weighting) whose width is the mean width at 320 m FOV and that calculated at the 80 m FOV is 16 Wm^{-2} (4.1% difference) compared to 12 Wm^{-2} (3.1%) using the mean width extrapolated to an 80 m FOV from measurements at 320 m FOV. For image F, which showed the greatest sensitivity of turbulent fluxes to field-of-view, the corresponding errors are 25 Wm^{-2} (6.3%) and 15 Wm^{-2} (3.8%).

I.3.5.2 Total Area

If lead area fraction in satellite imagery follows a known scaling law, then the "true" area fraction can be estimated from the area fraction determined at any scale. Fractal geometry is type of scaling relationship that has been used in the analysis of geophysical phenomena and deserves mention in the context of lead area. In particular, the stream length-drainage area relationship has been described in terms of fractals (Robert and Roy, 1990). However, in that and related studies the streams have no width and are therefore not applicable to the lead studies presented here. In contrast, *Karlinger and Troutman* (1992) have examined the "fat" fractal relationship between river channels with finite widths and drainage area. An examination of the data presented in Figure I.21 reveals that in general the fractional area coverage of leads decreases exponentially (log-linear) with increasing pixel size, and in some cases the decrease is even linear, so that the log-log relationship described by fractal scaling laws does not appear to apply.

As with lead widths, the rate of change of area fraction with increasing pixel size is not constant, but rather is a function of the threshold used. In fact, the direction of change is also threshold-dependent, so that the lead area may increase or decrease with increasing pixel size. The theoretical reasons for this are examined in *Key* (1993) where the distributions of the subpixel area fraction of various geophysical fields with known covariance structures are modeled by a Beta probability distribution, and the estimated total area fraction in an image is determined as a function of threshold. Unfortunately, the relationship between digital number (or temperature or reflectance) and the subpixel area fraction can be complex, so that expressing the subpixel area fraction threshold as a DN threshold is often not possible.

Therefore, perhaps the best estimate of the true area fraction of leads in an image is obtained using the procedure outlined earlier for mean lead width: degrading the image once, assuming an exponential or possibly linear relationship, and extrapolating back to a smaller FOV. Of course, the same thresholding operation must be used for both images (the Sobel operator here). As was done in the previous section, the potential error in this method for the Landsat images can be examined using the data in Figure I.21. Using image B, lead fraction extrapolated to an 80 m FOV from observations at an FOV of 320 m is 0.031 versus the observed fraction at 80 m of 0.0378. Combining this error with the error in open-water turbulent flux associated with mean lead width as calculated in the previous section, the error in using the extrapolated lead fraction and lead width versus the statistics observed at an 80 m FOV is 5.7% of the areally-averaged turbulent heat flux. If the lead statistics are not adjusted for field-of-view, i.e., if the lead statistics observed at an FOV of 320 m are used, then the error increases to 15.6%. For image F, the error is 20% using the extrapolated statistics compared to 40.7% percent using the statistics at 320 m. In these two cases, extrapolating the lead statistics reduces the average error in turbulent flux by about 57%. This technique is further applied to AVHRR and Landsat TM data in Section III.2.2.

I.4 LINEAL METHODS OF ESTIMATING LEAD PARAMETERS: WIDTH DISTRIBUTIONS MEASURED ALONG A TRANSECT

Perhaps the largest source of high-resolution data that is potentially useful for lead statistics is that collected by submarine sonar over the last three decades. For ice draft information these data are invaluable. But can they also be used for statistics of lead geometries; i.e., lead widths and spacings? Lead width and spacing statistics have been examined in two sonar data sets. Both are in the Canada Basin (Figure I.26); one in August of 1970 and one in October of 1978. Tables I.4 and I.5 show the results. How realistic are these data? If leads are conceptualized as linear features of some width, then crossing the lead at any angle other than perpendicular to its local orientation will result in an overestimate of the actual width.
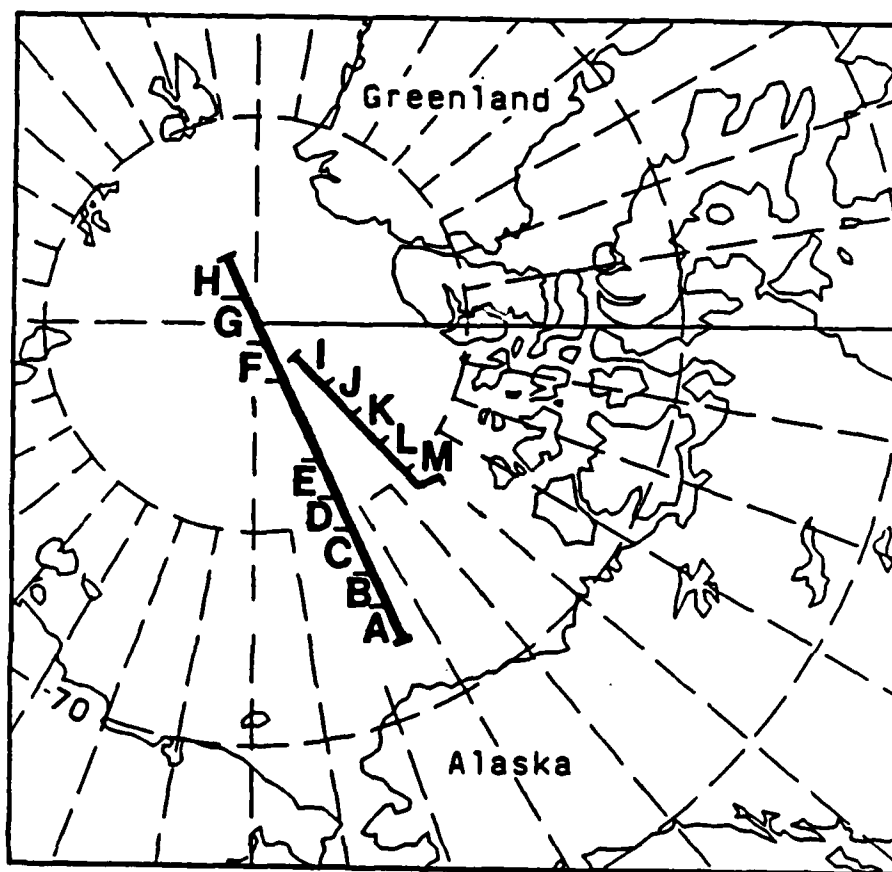
Figure I.26. Sonar transect locations through the central Canada Basin (August 1970) and northeastern Canada Basin (October 1978).

Table I.4. Lead widths (m) and standard deviations (below) in the QUEENFISH data by region, maximum draft (cm), minimum width (m). Also given are the maximum lead widths encountered. No statistics are given if fewer than 20 leads were found in a region.

MAX DRAFT/ MIN WIDTH	A	B	C	REGION D	E	F	G	H
30 / 3	26.5	33.1	21.3	26.5	47.7	------	18.5	23.8
	2.1	2.9	2.4	2.6	7.1		2.6	3.7
20	60.5	66.1	54.8	53.5	68.3	------	------	------
	3.8	5.8	5.6	5.2	. 9.6			
50	88.2	109.7	------	100.4	------	------	------	------
	5.3	·10.8		10.4				
200	------	------	------	------	------	------	------	------
Maximum:	228	502	130	283	327		70	90
70 / 3	32.6	54.8	27.5	32.1	49.4	36.4	34.7	40.0
	3.3	3.8	2.0	2.8	7.0	8.3	3.8	3.7
20	63.7	78.1	55.6	54.2	73.7	55.9	59.0	60.4
	6.8	5.2	3.9	4.2	9.9	13.9	6.4	5.4
50	106.1	129.2	106.5	104.2	129.5	------	98.1	105.5
	14.3	8.5	7.9	9.5	19.0		10.3	9.1
200	------	------	------	------	------	------	------	------
Maximum:	885	526	255	294	374	537	257	227
100 / 3	28.9	40.8	32.9	30.9	50.5	32.4	36.4	40.0
	2.4	2.5	2.5	2.2	6.5	6.6	3.7	3.6
20	59.3	70.4	70.2	53.6	74.1	------	57.9	62.8
	5.4	4.1	5.5	3.8	9.1		5.9	5.6
50	102.4	126.6	124.5	98.6	123.0	------	98.6	109.6
	11.9	7.8	11.2	8.1	15.9		10.0	9.8
2C0	------	------	------	------	------	------	------	------
Maximum:	886	533	763	299	374	539	263	269

Table I.4, *cont.* Lead widths (m) and standard deviations (below) in the northeastern Canada Basin data by region, maximum draft (cm), minimum width (m). Also given are the maximum lead widths encountered. No statistics are given if fewer than 20 leads were found in a region.

MAX DRAFT/ MIN WIDTH	I	J	REGION K	L	M
30 / 3	116.9	9.6	10.2	------	5.4
	100.8	4.9	2.4		1.7
20	------	------	------	------	------
50	------	------	------	------	------
200	------	------	------	------	------
Maximum:	2181	153	83		42
70 / 3	30.8	14.4	17.6	8.7	15.9
	16.1	2.0	3.3	1.3	4.2
20	132.8	62.5	65.8	------	------
	81.4	9.3	13.7		
50	------	------	------	------	------
200	------	------	------	------	------
Maximum:	2274	234	342	72	510
100 / 3	28.7	17.9	18.8	9.4	16.5
	12.1	2.1	2.7	1.1	4.5
20	104.6	61.6	68.8	------	84.7
	52.9	7.4	10.8		29.9
50	------	------	------	------	------
200	------	------	------	------	------
Maximum:	2280	239	348	81	792

Table I.5. Lead spacings in the QUEENFISH data, by region, maximum draft (cm), minimum width (m). S=mean spacing (m) with standard deviation below, N=number of leads per kilometer. Also given are the maximum spacings encountered. No statistics are given if fewer than 20 leads were found in a region.

MAX DRAFT/ MIN WIDTH		REGION A	B	C	D	E	F	G	H
30 / 3	S:	462.9	428.5	929.9	739.4	685.9	------	2190.9	2551.0
		39.9	41.7	118.9	82.2	155.1		402.5	759.2
	N:	2.01	2.16	1.06	1.31	1.38		0.45	0.33
20	S:	1240.1	1014.0	2821.6	1897.2	1061.8	------	------	------
		150.1	125.6	601.9	307.5	240.6			
	N:	0.73	0.92	0.31	0.51	0.90			
50	S:	2552.6	2351.2	------	5493.8	------	------	------	------
		318.7	503.1		1436.6				
	N:	0.36	0.41		0.17				
200		------	------	------	------	------	------	------	------
Maximum:		4893	5842	9321	8594	7062		13523	24321
70 / 3	S:	339.7	369.8	364.1	513.0	504.7	553.1	859.6	737.7
		24.9	30.2	34.6	41.2	102.8	108.2	100.1	61.9
	N:	2.67	2.35	2.56	1.83	1.82	1.70	1.10	1.14
20	S:	783.2	568.2	926.6	1050.0	816.9	983.4	1775.5	1230.3
		70.6	50.3	97.9	102.5	173.1	221.0	264.0	131.4
	N:	1.16	1.53	1.02	0.91	1.14	0.98	0.54	0.67
50	S:	1818.8	1238.0	2935.7	3226.0	1868.1	------	3757.9	3029.1
		190.6	150.4	621.9	577.5	515.6		1200.8	653.3
	N:	0.50	0.73	0.33	0.29	0.48		0.22	0.27
200		------	------	------	------	------	------	------	------
Maximum:		3807	4792	4777	4488	6782	4996	6221	3304
100 / 3	S:	238.1	213.4	225.5	416.3	443.2	421.6	837.0	722.0
		14.8	13.1	17.9	31.5	88.4	84.4	97.6	72.3
	N:	3.73	3.93	3.86	2.24	2.04	2.20	1.13	1.31
20	S:	597.7	416.5	581.6	866.6	705.2	------	1587.7	1321.9
		46.4	33.7	59.9	78.7	147.0		227.5	213.0
	N:	1.51	2.05	1.54	1.09	1.30		0.60	0.72
50	S:	1468.9	1064.2	1449.1	2465.7	1591.7	------	3603.1	3251.1
		157.0	126.1	261.8	348.7	397.6		1158.5	723.5
	N:	0.61	0.83	0.63	0.37	0.60		0.23	0.29
200		------	------	------	------	------	------	------	------
Maximum:		2897	2808	3628	4478	6779	4993	6218	8918

Table I.5, *cont.* Lead spacings in the northeastern Canada Basin data, by region, maximum draft (cm), minimum width (m). S=mean spacing (m) with standard deviation below, N=number of leads per kilometer. Also given are the maximum spacings encountered. No statistics are given if fewer than 20 leads were found in a region.

MAX DRAFT/				REGION		
MIN WIDTH		I	J	K	L	M
30 / 3	S:	3381.9	4567.3	2477.4	------	2996.1
		1500.2	2495.0	913.9		1948.1
	N:	0.15	0.22	0.36		0.17
20		------	------	------	------	------
50		------	------	------	------	------
200		------	------	------	------	------
Maximum:		23429	71342	42161		37059
70 / 3	S:	994.4	700.1	928.5	1763.9	911.1
		229.6	129.7	159.7	449.3	169.6
	N:	0.96	1.37	1.01	0.53	1.07
20	S:	4476.4	4587.8	4479.7	------	------
		1396.3	1513.8	1513.3		
	N:	0.19	0.21	0.20		
50		------	------	------	------	------
200		------	------	------	------	------
Maximum:		24918	13508	10022	25355	14562
100 / 3	S:	739.6	585.6	635.4	858.2	709.5
		130.6	73.9	89.7	197.8	110.9
	N:	1.28	1.65	1.53	1.09	1.36
20	S:	2896.8	2765.0	2860.5	------	4493.1
		795.8	623.6	608.4		1214.4
	N:	0.29	0.35	0.31		0.19
50		------	------	------	------	------
200		------	------	------	------	------
Maximum:		12353	7298	10022	25212	11154

A methodology has been developed for estimating width distributions of linear features from measurements along a transect through a network of such features. A probabilistic determination of this error is described here, providing a starting point for the application of stochastic geometry theorems in the analysis of lead geometries. Errors in statistics derived for other lead and keel features are discussed briefly. While the application is to sea ice leads and sonar data, the methods also apply to the general problem of sampling linear features along a transect.

I.4.1 DEFINITIONS, NOTATION, AND AN ILLUSTRATION

In the following discussions, notation follows that used in probability theory, where $F_Z(z)$ denotes the distribution function (df) for the population random variable Z with specific instance z (i.e., $F_Z(z) \equiv P[Z < z]$) and $f_Z(z)$ is the probability density function (pdf). Additionally, $E[Z]$ and $Var[Z]$ are the expected value and variance of Z.

The problem is to relate a distribution of lead widths taken along a line perpendicular to the local orientation of a lead (the "actual" width) to the lead widths measured along a transect (the "apparent" lead width), taking into account lead orientations, and lead crossing angles. As illustrated in Figure I.27, the following continuous random variables are defined:

X - actual lead width,

X' - apparent lead width measured along a transect, $X' \geq X$,

Θ - lead orientation ($0 \leq \Theta < \pi$),

A - lead intersection angle ($0 \leq A < \pi$)

with specific realizations x, x', θ, and α. Additionally, let ϕ be the transect orientation ($0 \leq \phi < \pi$). The position and orientation of a lead within the plane are uniquely specified by the length of the perpendicular that connects the lead to the origin, and the angle that it makes with a fixed reference line. The *intersection* angle A is measured between the transect and the lead, anticlockwise, and is the difference between their orientations. Finally, define $A' = |\pi/2 - A|$ to be the *crossing* angle (α' in Figure I.27) measured between the transect and a perpendicular to the lead orientation ($0 \leq A' \leq \pi/2$). The relationship between apparent and actual lead widths is

$$X' = \frac{X}{\cos(A')} \qquad (12)$$

where $X \leq X'$. Rearranging terms, a lead crossing angle can be determined from the lead widths by

$$A' = \cos^{-1}\left(\frac{X}{X'}\right)$$

The potential inaccuracies of measuring lead widths along a transect can be illustrated by randomly choosing a transect orientation and location on a satellite image. Here we provide an example with a Landsat Multispectral Scanner (MSS) band 4 (0.5-0.6 μm) scene of the Beaufort Sea, March 1988 (Figure I.28). The pixel size is 80 m; image size is 80 x 80 km, a subset of a Landsat scene. To increase the sample size of lead widths measured along the transect, multiple transects of the same orientation are placed randomly on the image. It is assumed that the pattern of leads is similar beyond the image boundaries. Processing of the Landsat data for the retrieval of lead statistics is as follows. A dynamic threshold procedure is applied that estimates the probability density function of a mixture population (lead/ice) for small regions within the image, and a binary image results. Valid lead fragments are

identified, where "valid" refers to a linear feature for which a meaningful width and orientation can be determined. Linearity is determined through correlation/regression analysis. Lead widths are measured perpendicular to the regression line, every kilometer along the lead length, and the slope of the regression line is a measure of the lead orientation. Further details of this procedure are given in *Key et al.* [1990].
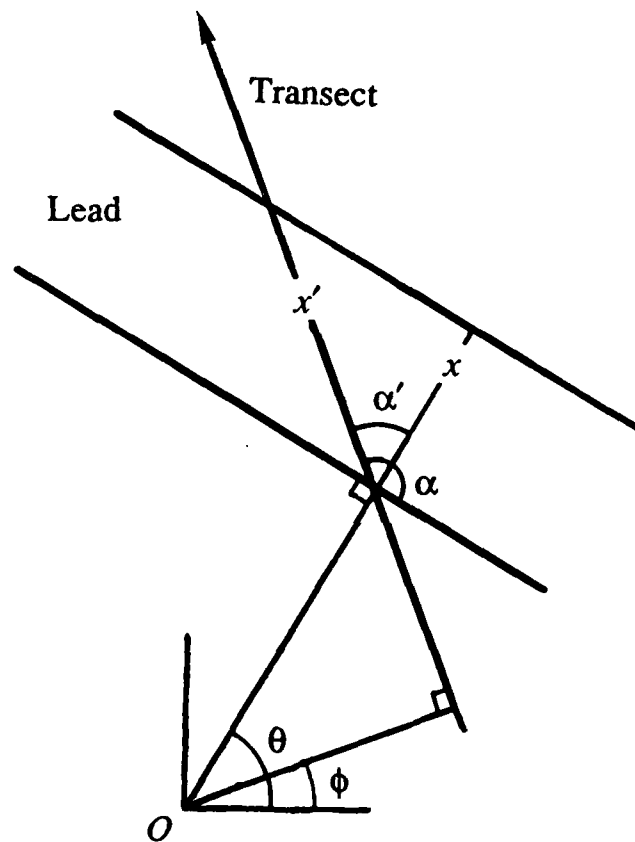
Fig. I.27. The geometrical relationships between a lead and a transect. See text for definition of angles and length variables.
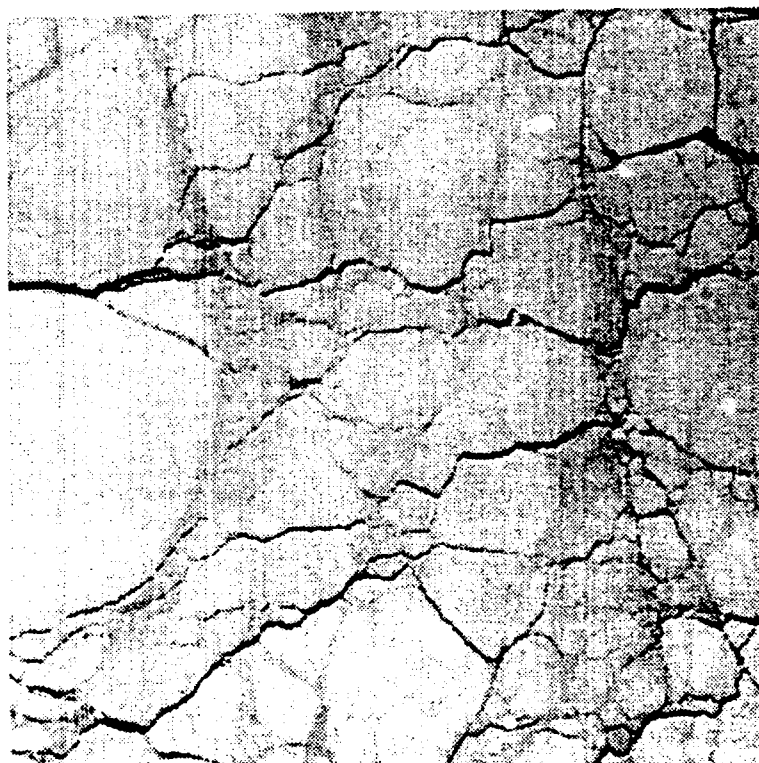
Fig. I.28. Landsat MSS band 4 scene of the ice pack north of Alaska in March 1988. Area covered is approximately (80 km)². Field-of-view is 80m.

The distribution of these actual lead widths x is shown in Figure I.29 and orientations θ in Figure I.30. The mean lead orientation is 0.67 radians (38°, approximately southeast to northwest where the top of the image is north). For a transect orientation ϕ=3.0 radians (172°, south-southwest to north-northeast), the distribution of apparent lead widths x' is illustrated in Figure I.31, with crossing angles α' shown in Figure I.32. The mean actual width is 348 m with a standard deviation of 201 m, while the mean apparent width is 368 m with a standard deviation of 474 m. Additionally, the maximum actual lead width in the image is 1,376 m, while the maximum width measured along the transect is 2,818 m. With a transect orientation of 0.13 radians (7.4°) the difference between the actual and apparent mean widths is 139 m and the maximum width is 2,670 m. From this example it is clear that significant errors can result from sampling along a transect. The following section presents a method to assess this error.

I.4.2 PROBABILITY MODELS

Theorems of stochastic geometry that are applicable here have been developed through the study of fibers as a stationary random process in the plane. If we use this analogy with lead networks, then after *Stoyan et al.* (1987, p. 240) the df of intersection angles is

$$F_A(\alpha) = \frac{\int_\phi^{\phi+\alpha} \sin (\theta' - \phi) \, dF_\Theta(\theta')}{\int_0^\pi |\sin (\theta' - \phi)| \, dF_\Theta(\theta')} \tag{13}$$

where $F_A(\alpha)$ is the probability of intersection angles between 0 and α, $F_\Theta(\theta)$ is distribution function for lead orientations, $dF_\Theta(\theta) = f_\Theta(\theta) \, d\theta$, α increases in an anticlockwise sense, and in the integral $F_\Theta(\pi + \alpha) = 1 + F_\Theta(\alpha)$. The pdf $f_\Theta(\theta)$ may be an assumed mathematical distribution or may be based on an observed rose of direction.

If the leads are isotropic then the corresponding orientations have a simple uniform probability distribution in the interval $0 \leq \theta < \pi$; i.e., $f_\Theta(\theta)=1/\pi$ for all θ. In this case the distribution of intersection angles is independent of the transect orientation. The probability of crossing a lead that is oriented across the transect ($\alpha \to \pi/2$) is greater than for one running more parallel ($\alpha \to 0$ or π). The associated intersection angles have density

$$f_A(\alpha) = \frac{1}{2} \sin \alpha \quad , \quad 0 \leq \alpha \leq \pi$$

which is not uniform but is symmetrical about $\alpha = \pi/2$. The corresponding distribution function is

$$F_A(\alpha) = \int_0^\alpha f_A(\psi) \, d\psi = \frac{1}{2} (1 - \cos \alpha) \quad , \quad 0 \leq \alpha \leq \pi$$

which is a special case of (13) for $f_\Theta(\theta) = 1/\pi$. In the anisotropic (preferred orientation) case we use (13) for the distribution of intersection angles, and the corresponding densities are determined numerically.

Two different intersection angles correspond to each crossing angle so that the distribution and density functions for the crossing angle are

$$\begin{aligned}
F_{A'}(\alpha') &\equiv P[A' \leq \alpha'] \\
&= P[|\tfrac{\pi}{2} - A| \leq \alpha'] \\
&= P[-\alpha' \leq (A - \tfrac{\pi}{2}) \leq \alpha'] \\
&= P[(\tfrac{\pi}{2} - \alpha') \leq A \leq (\tfrac{\pi}{2} + \alpha')] \\
&= F_A(\tfrac{\pi}{2} + \alpha') - F_A(\tfrac{\pi}{2} - \alpha')
\end{aligned}$$

and

$$f_{A'}(\alpha') = \frac{dF_{A'}}{d\alpha'} = f_A(\tfrac{\pi}{2} + \alpha') + f_A(\tfrac{\pi}{2} - \alpha')$$

which in the isotropic case yields $F_{A'}(\alpha') = \sin \alpha'$ and $f_{A'}(\alpha') = \cos \alpha'$.

An expression for the joint density function of the apparent and actual lead widths can be derived. Suppose that the joint pdf of X and A' are known, which will be $f_{X,A'}(x,\alpha') = f_X(x)f_{A'}(\alpha')$ if the two variables are independent. Then if Y and Z are two new random variables that are functions of X and A' such that $Y = X$ and $Z = X' = X/\cos A'$, then the joint pdf of Y and Z can be computed using a standard theorem (*Ross*, 1984, p. 217):

$$f_{Y,Z}(y,z) = f_{X,X'}(x,x') = f_{X,A'}[x,\cos^{-1}(\frac{x}{x'})]\, \frac{x}{x'}\, [(x')^2 - x^2]^{-\frac{1}{2}}$$

$$= f_X(x)\, f_{A'}[\cos^{-1}(\frac{x}{x'})]\, \frac{x}{x'}\, [(x')^2 - x^2]^{-\frac{1}{2}} \tag{14}$$

The first of these expressions is valid whether or not X and A' are independent. If, however, future research indicates that large leads are oriented differently than small leads, for example, then the joint density function must be determined in another manner (possibly from observations). Using (14) the pdf of apparent lead widths can be obtained:

$$f_{X'}(x') = \int_0^\infty f_{X,X'}(x,x')\, dx$$

$$= \int_0^{x'} f_X(x)\, \{f_{A'}[\cos^{-1}(\frac{x}{x'})]\, \frac{x}{x'}\, [(x')^2 - x^2]^{-\frac{1}{2}}\}\, dx \tag{15}$$

The df of apparent lead widths can be obtained by integrating (15) or by conditioning on the value of X, again assuming that X and A' are independent. The latter method yields

$$F_{X'}(x') = \int_0^{x'} F_{A'}[\cos^{-1}(\frac{x}{x'})]\, f_X(x)\, dx \tag{16}$$

which is based on the df rather than the pdf of A'. The functions can be discretized as arrays and the integral in (16) approximated as a sum:

$$F_{X'}(j) = \Delta \sum_{i=1}^{j} F_{A'}(j,i)\, f_X(i)\, , \quad i,\, j \in [1,N],\ x=i\Delta,\ y=j\Delta \tag{17}$$

where $F_{A'}(j,i) = F_{A'}[\cos^{-1}(i/j)]$, N is the number of discrete observations and Δ is the increment between observations. If these functions are expressed as matrices, (17) becomes

$$F_{X'} = \Delta\, F_{A'}\, f_X$$

$$f_X = \frac{1}{\Delta}\, F_{A'}^{-1}\, F_{X'}$$

whose derivation is given in *Key and Peckham* (1991).

In this study the error in measured lead width is defined as $X'-X$ (which is always positive), although other definitions such as X/X' would also be useful. Equation (14) allows us to compute the

distribution of the error as follows:

$$F_{X'-X}(a) \equiv P[X'-X \le a] = \int_0^\infty \int_x^{a+x} f_{X,X'}(x,x') \ dx' \ dx \ , \quad a \ge 0$$

For the isotropic case

$$F_{X'-X}(a) = \int_0^\infty f_X(x) \ \sqrt{a} \left[\frac{\sqrt{2x + a}}{x + a} \right] dx$$

All moments of $X'-X$ can be computed from $f_{X'-X}$.

Lead Widths in Landsat Image
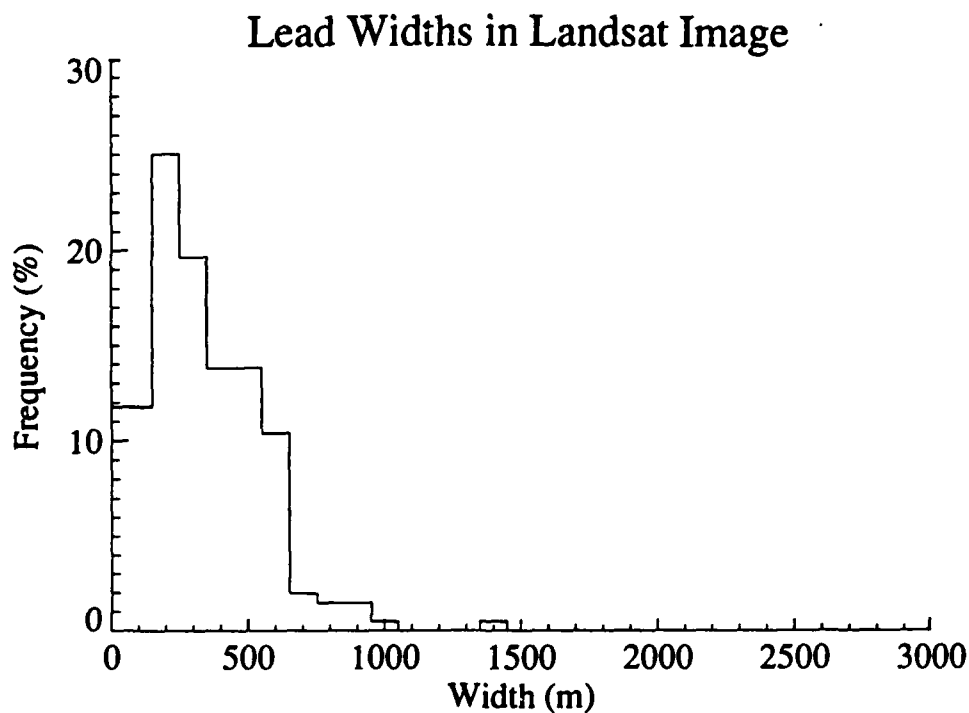
Fig. I.29. Lead width distribution for the scene in Figure I.28. Widths are measured along a perpendicular to the local orientation of the lead, and are grouped in 100 m bins. The mean width is 348 m, the standard deviation 201 m, and maximum width 1376 m.

Lead Orientations in Landsat Image
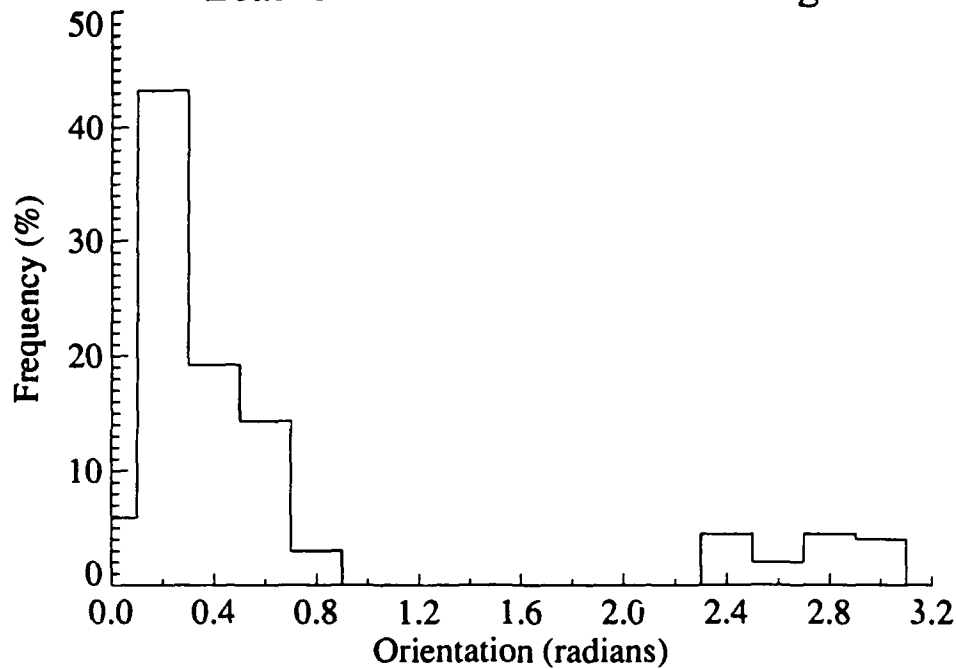
Fig. I.30. Lead orientations for the scence in Figure I.28. The mean orientation is 0.67ʳ (38.4°) with standard deviation 0.87ʳ (49.8°).
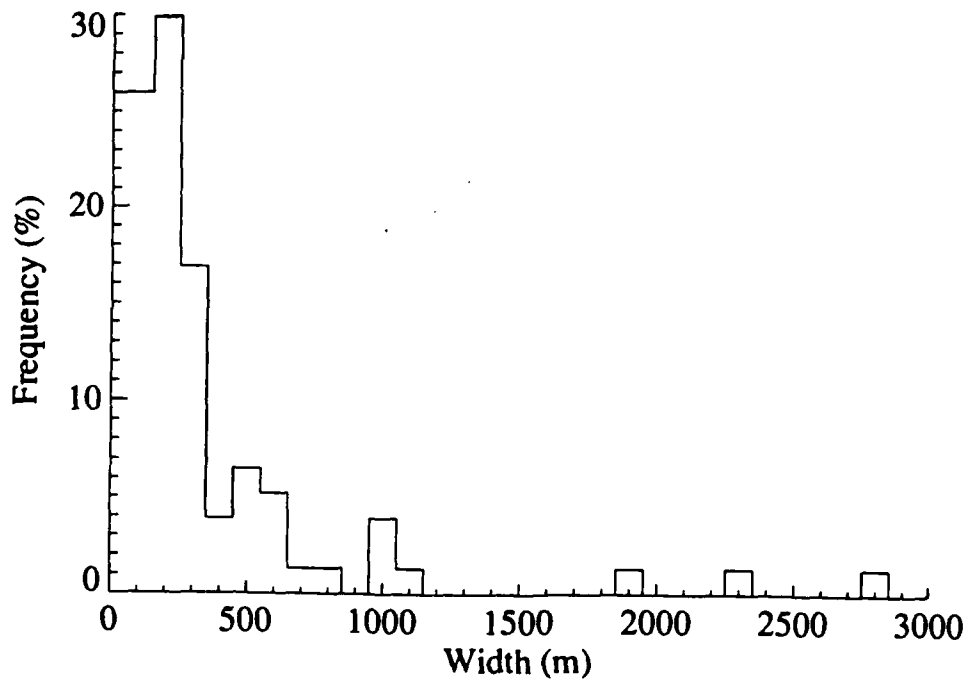
Fig. I.31. Lead widths from a randomly-chosen transect across Figure I.28. Transect orientation is 3.0ʳ (172°) or approximately south-southwest to north-northeast where the top of the image is north. The mean width is 368 m, the standard deviation 474 m, and maximum width 2818 m.

Lead Crossing Angles
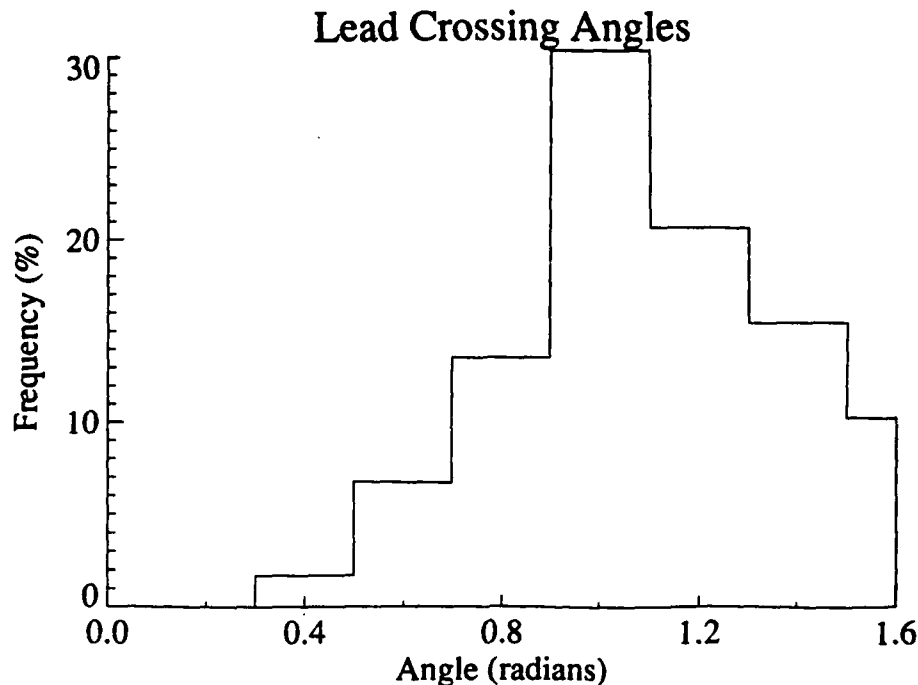
Fig. I.32. Lead crossing angles for a transect across Figure I.28. Transect orientation is the same as in Figure I.31. The mean crossing angle is 1.09^r (62°) with standard deviation 0.23^r (13°).

I.4.3 APPLICATION

These models are now applied. First, A lead width distribution measured from sonar data is used to estimate the actual lead width distribution, for both isotropic and anisotropic orientations. Lead orientation and actual width distributions are then assumed known, and the expected error in lead width is determined for a variety of situations.

Lead width distributions have been described by power laws (*Wadhams*, 1981; *Steffen*, 1987) as have floe sizes (*Rothrock and Thorndike*, 1984). The negative exponential distribution has also been used (*Dickins et al.*, 1986) with mean lead width λ and variance λ^2. The exponential model implies that there are a finite number of small leads, and that the field is characterized by a length scale λ. In fact, the lead width distribution may be scale-free, in which case a power law would be appropriate. There is, of course, a lower limit imposed by the resolution of the measuring instrument, and for this reason as well as for clarity of illustrating expected values, we use the negative exponential model.

Lead orientations may be random or may have a preferred orientation. A Gaussian model is used here for preferred orientations. It is recognized, however, that the actual shape of the distribution may be bimodal, where large leads with one orientation are intersected by smaller leads at another. Intersection angles of approximately 28° have been observed elsewhere (*Marko and Thompson*, 1977). This situation is not obvious in Figure I.30, although the distribution is not purely Gaussian either.

Table I.6 lists the expected error for a variety of conditions, where error is defined by the difference between the actual and measured lead widths. Case 1 considers the situation where the apparent

lead width distribution is known. The apparent lead widths are based on submarine sonar data recorded by the USS QUEENFISH in August of 1970 in the central Canada Basin (*McLaren*, 1989). Ice draft data were measured by an upward-beamed fathometer with a footprint diameter of approximately 2.7 m and a vertical accuracy of ±10 cm. Sequences of continuous points with drafts ≤30 cm constitute leads, an example of which is given in Figure I.33. Given a mean apparent lead width of 60.6 m, the expected value of the error is 65.7 m with a variance of 1466.1 m^2. For cases 2-7 in Table I.6 the actual width density function is assumed known, and the apparent lead width distribution is estimated. For cases 2 and 3, the crossing angle distributions are shown in Figure I.34, and the error distributions in Figure I.35. In the preferred orientation cases (2-5) the error means and variances are clearly dependent upon transect orientation.

Other applications of this procedure are possible. For example, laser profilometer transects are analogous to sonar transects, and the methods outlined above could be used for lead and ridge spacing distributions and their associated errors. As in the illustration with Landsat data, transect sampling of satellite imagery is a natural application. Similarly, heat flux through leads is in part a function of fetch, and fetch is a function of the actual lead width and the crossing angle of the wind. If the wind direction is constant as it travels across the network of leads, then the distribution of fetches can be determined from the distribution of actual lead widths. Finally, it may be possible to estimate open water fraction over a large area from the apparent lead width and spacing distributions measured along a transect. This research is currently in progress, with results to be presented subsequently.

Table I.6. Expected error in lead widths (m) under a variety of assumed distributions and mean values.

Case	f_X[1]	$f_{X'}$	f_Θ	ϕ^r	$E(X - X')$	$Var(X - X')$
1	?[2]	Sonar	Uniform	---	65.7	1466.1
2	λ=20m	?	Gaussian[3]	2.36 (135°)	3.7	3.1
3	λ=20m	?	"	0.52 (30°)	32.5	165.9
4	λ=40m	?	"	2.36 (135°)	4.8	6.4
5	λ=40m	?	"	0.52 (30°)	36.0	345.3
6	λ=20m	?	Uniform	---	43.2	653.1
7	λ=40m	?	"	---	64.2	1391.2

[1] Width distribution model is negative exponential.
[2] "?" refers to the unknown distribution.
[3] Parameters of the Gaussian model are $\mu=\pi/4^r$ (45°) and $\sigma=0.3^r$ (17°).

Ice Draft from Sonar
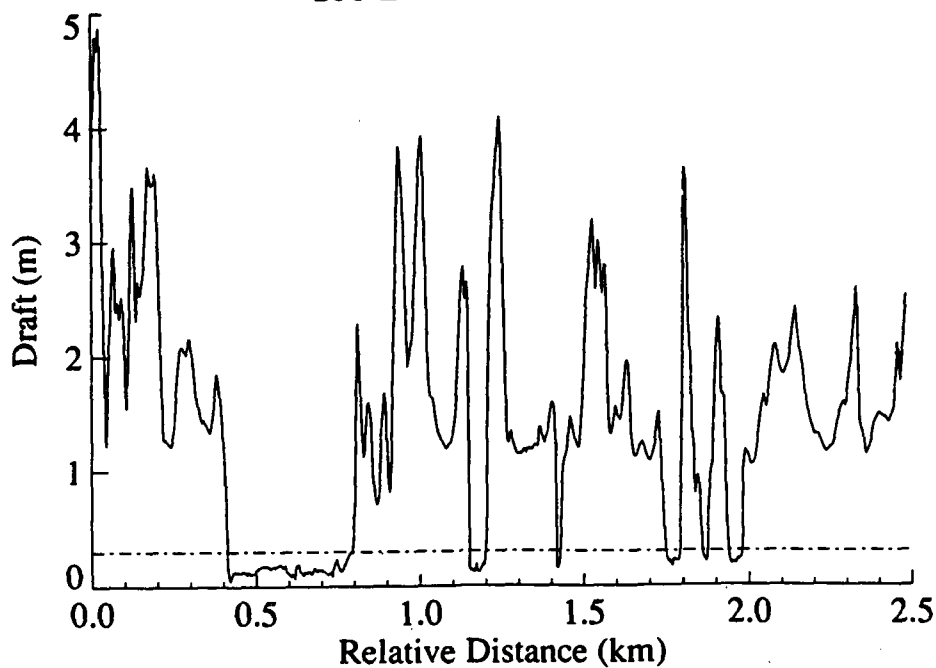
Fig. I.33. Submarine sonar ice draft data for a 2.5 km section within the Canada Basin north of Alaska. Leads are defined as continuous sequences of points with drafts no greater than 0.3 m (dashed line); six leads occur in this section.

Fig. I.34. The distribution functions of crossing angles F_A for cases 2 (solid) and 3 (dashed) in Table I.6.

Error Distributions
Transect Orientations: 2.36 (solid), 0.52 (dashed)
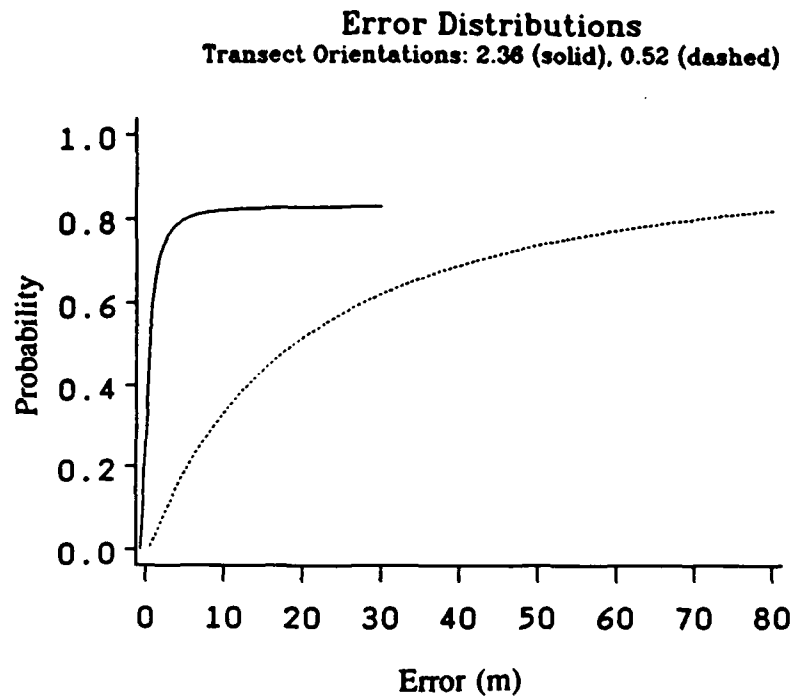
Fig. I.35. The distribution functions of the lead width errors, $F_{X'-X}$, for cases 2 (solid) and 3 (dashed) in Table I.6.

I.5 LEAD FRACTIONAL AREA COVERAGE ALONG A TRANSECT

In the previous section sea ice leads were modeled as a Poisson line process and a method was was presented for estimating the "actual" lead width distribution from a width distribution measured along a transect (the "apparent" lead width distribution). The purpose of this section is to extend that work to the estimation of the fractional area coverage of leads from measurements along a line. This line could be a submarine transect under the ice or on a satellite image. Two methods from stochastic geometry are presented although applications have not yet been performed. While the problem is illustrated with respect to sea ice leads it should be noted that the general lineal method described here is applicable to any geophysical parameter with known (or determinable) spatial structure.

I.5.1 GENERAL LINEAL METHOD

The general expression for the estimate of the fractional area coverage, p', of a geophysical parameter whose actual fractional coverage is p, regardless of the the spatial structure of that parameter is

$$p' = \mu_U^{-1} \int_U I(\mathbf{x}) \, d\mathbf{x}$$

where $I(\mathbf{x})$ is the indicator function for the underlying function $q(\mathbf{x})$ at location $\mathbf{x}$ and the factor μ_U is needed for normalization and depends on the shape of the structuring element U (e.g., it may be the length of a line or the area of a square). The indicator function takes on a value of 1 if $q(\mathbf{x})$ satisfies some condition and 0 otherwise. For example, if a thre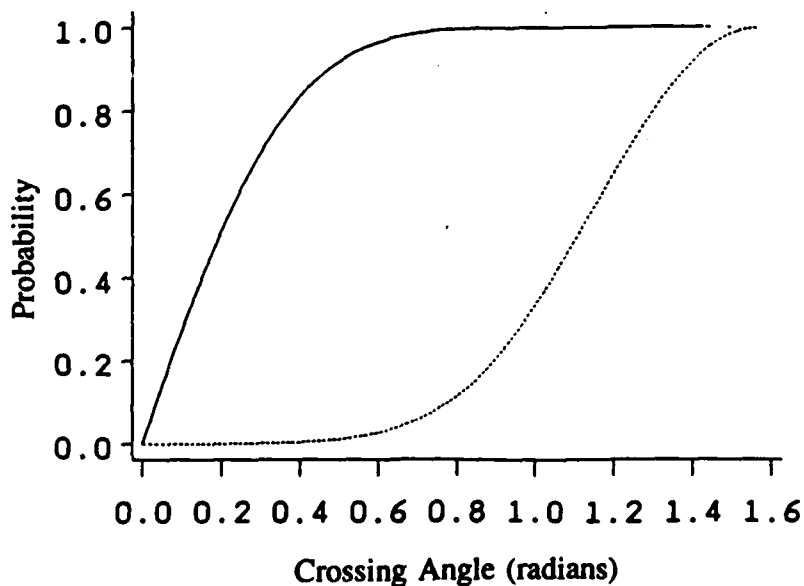sholding procedure is used to determine whether or not each pixel in an image or each data point in submarine sonar data represents some phenomenon, then $I(\mathbf{x})=1$ if the data value passes the threshold test and $I(\mathbf{x})=0$ otherwise. Again, this applies to any structuring element U.

Following *Stoyan et al.* (1989) the expected value of p', $E(p')$, is p and its variance is

$$\text{Var}(p') = E(p'-p)^2 = \mu_U^{-2} \int_U \int_U k_I(\|\mathbf{x}-\mathbf{y}\|) \, d\mathbf{x} \, d\mathbf{y}$$

where k_I is the autocovariance function of the indicator function I:

$$k_I(r) = E[I(\mathbf{x}) I(\mathbf{x}+r)] - E[I(\mathbf{x})]^2$$

The displacement or lag $r = \|\mathbf{x}-\mathbf{y}\|$ is such that the covariance depends only on the distance between the two points and not on direction. The assumptions are that the geophysical field $q(\mathbf{x})$ is stationary and isotropic.

Now we consider the case where the structuring element is a line. For measurements along an array of N parallel lines, each of length L, the unbiased estimate of the fractional area coverage is

$$p' = \frac{l}{NL} \tag{18}$$

where l is the total length of NL where $I(\mathbf{x}) = 1$. Extending the work of *Rothrock and Thorndike* (1984), *the estimation variance is*

$$\text{Var}(p') = N^{-1}L^{-2} \int_{\mathfrak{L}} \int_{\mathfrak{L}} k_f(|x-y|) \, dx \, dy \qquad (19a)$$

$$= 2N^{-1}L^{-2} \int_{\mathfrak{L}} (L-r) \, k_f(r) \, dr \qquad (19b)$$

where $\mathfrak{L}$ is the set containing the N lines and $r = |x-y|$, the distance between two locations x and y on the line.

Exponential covariance is a reasonable model for many geophysical parameters and is used here:

$$k_f(r) = p(1-p) e^{-\alpha r} \qquad (r, \alpha \geq 0) \qquad (20)$$

where α describes the dependence of the covariance on the distance r. The parameter α can be determined from observed autocovariances by rewriting (20) in linear form as

$$\ln[k_f(r)] = \ln[p(1-p)] - \alpha r \qquad (21)$$

and estimating α from the data through a least squares regression.

In the case of exponential covariance the estimation variance in (19) is

$$\text{Var}(p') = \frac{2p(1-p)(1 + \frac{e^{-\alpha L} - 1}{\alpha L})}{\alpha N L} \qquad (22a)$$

$$\approx \frac{2p(1-p)(1 - \frac{1}{\alpha L})}{\alpha N L} \qquad (22b)$$

I.5.2 APPLICATION

One real and two simulated images are used in the application of the above methods. The real image is a Landsat MSS band 4 (0.5-0.6μm) scene of the Beaufort Sea, March 1988. The binary image produced by applying a threshold to the original grey-scale image is shown in Figure I.36a. The pixel size is 80 m; image size is 24 x 24 km, a subset of a full Landsat scene. Next, a network of leads is simulated as a Poisson line process. The mean spacing between lines (leads) is 3000 m and their orientations are random. The lines are assigned thicknesses (widths) following the negative exponential density function:

$$f_w(w) = \frac{1}{\lambda} e^{-w/\lambda}$$

where w is lead width and λ is the mean width. For the simulation $\lambda = 200$ m. One realization of the Poisson line process is shown in Figure I.36b, again as a binary image, where the pixel size is 137.5 m. Lastly, a cloud field is simulated as an ensemble of disks whose diameters are approximately normally-distributed (in a true Gaussian distribution negative diameters would be possible) and whose center

locations follow a binomial point process. This model is appropriate for cumuliform clouds but is obviously not applicable to stratiform cloud decks. One realization is shown in Figure I.36c.

As stated earlier, the expected value of p' is p; i.e., the mean of the sampling distribution of sample proportions is the same as the population or true mean. The variance of the sample proportions is given by (19) in the general case and (22) for exponential covariance. How well does this theory compare to observations? As the first step, the "true" autocovariance functions were estimated from six random, horizontal transects through each image. The α coefficient in (21) was computed for each of the six transects and then averaged. With the simulated clouds and leads the horizontal transects should adequately represent the two-dimensional structure since the patterns are isotropic. This is less true, however, with the Landsat image where a preferred orientation is apparent. Table I.7 gives the results of the least squares fit of the exponential autocovariance function to the observed autocovariances in the images. Listed are the regression-estimated variance (the antilog of the y-intercept in (21)), α, and the correlation coefficient. Next the distributions of sample fractional area estimates and their first two moments (mean and variance) were determined by computing p' with (18) for each of 500 single, random, horizontal transects through each image (i.e., the number of transects used to calculate p' in (18), N, is 1 for each of 500 samples). Distributions of p' were also computed for sets of ten such parallel transects giving 5000 transects ($N=10$ for each of 500 samples). Figure I.37 shows how the distribution of the estimates changes as a function of the number of transects or, effectively, total transect length. For single transects (solid lines) a broad range of p' are possible.
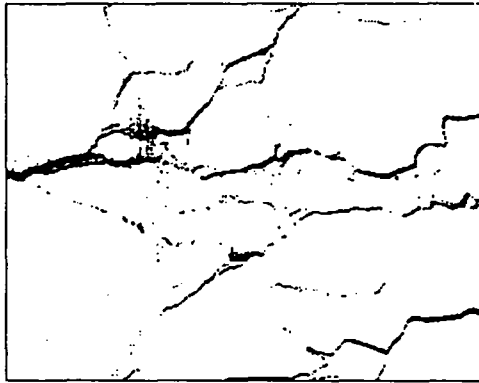
Fig. I.36. (a) Binary image based on a Landsat MSS band 4 scene of the ice pack north of Alaska in March 1988. Field-of-view is 80 m; area covered is approximately $(24 \text{ km})^2$. (b) A simulated lead network modeled as a Poisson line process with thick lines. Field-of-view is 137.5 m; image size is approximately $(42 \text{ km})^2$. (c) A simulated cloud field based on a random disk model. Field-of-view is 137.5 m; image size is approximately $(42 \text{ km})^2$.
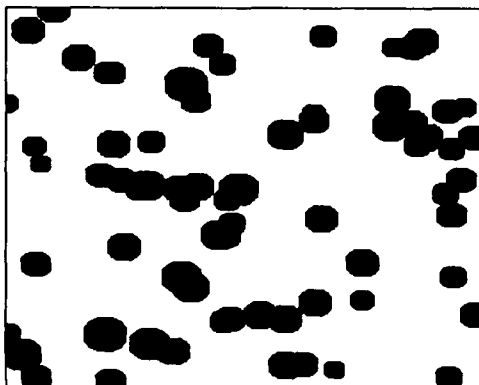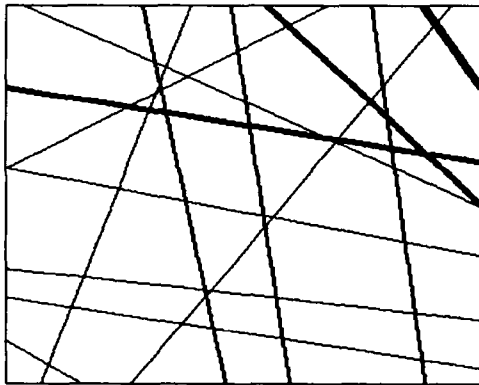
Fig. I.37. Relative frequency histograms of the distribution of estimated area fraction for different total line lengths. Plots correspond to the images in Figures I.36a-c.

Frequency of Area Fraction
Landsat

Frequency of Area Fraction
Simulated Leads

Frequency of Area Fraction
Simulated Clouds
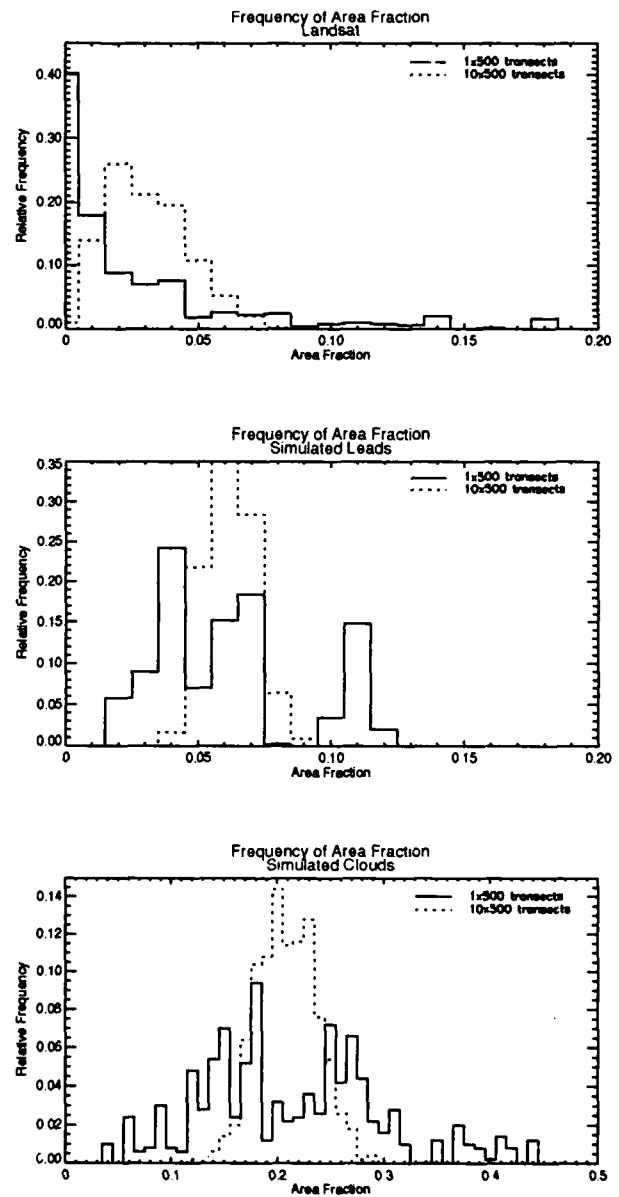
Table I.8 gives the true area fraction p, the means and variances of the estimated area fraction p' from the observed distributions in Figure I.37, and the variance computed from (22b), where $L=304$ pixels (same units as r in (21)). The true area fraction is the proportion of pixels in the binary image where $I(x)=1$. It is apparent that the theoretical variance of the estimate given in (22) is generally applicable for the simulated leads and clouds in Figures I.36b and I.36c. For the Landsat data, however, the variance of the estimate for the 500-set simulation is three times as large as that computed with (22) or a factor of 1.7 for the standard deviation. This is due to the anisotropic nature of the lead network in the image and the large variability in the autocovariance function computed for individual transects. A two-dimensional autocovariance function and a modification of (22) may be needed in such cases.

Table I.7. Regression-estimated parameters of the autocovariance function for the images in Figure I.36.

Figure	$p(1-p)^1$	α	R
1a	0.029	0.319	-0.99
1b	0.078	0.554	-0.96
1c	0.218	0.121	-0.92

[1] Estimated with (21).

Table I.8. Actual and estimated fraction area coverages for Figures I.36a-c using one and ten transects.

| Figure	p	$N = 1 \times 500$ E(p')	Var(p')	$N = 10 \times 500$ E(p')	Var(p')
1a	0.035	0.035	2.07e-3 (6.84e-4)[1]	0.036	2.35e-4 (6.84e-5)
1b	0.067	0.067	7.56e-4 (7.38e-4)	0.067	7.62e-5 (7.38e-5)
1c	0.215	0.218	7.28e-3 (8.93e-3)	0.214	7.78e-4 (8.93e-4)

[1] Values in parentheses are computed with (22b).

The fact that the distributions of area fraction estimates tends toward Gaussian as N increases suggests a method for hypothesis testing and confidence interval estimates. If a normal distribution is assumed to apply, then the probability that a particular area fraction estimate comes from a population with area fraction p can be determined. This is perhaps most useful for confidence interval estimates of the true area fraction, defined as

$$p' - z(\beta/2)\,\text{sd}(p') \quad \text{to} \quad p' + z(\beta/2)\,\text{sd}(p')$$

where $\text{sd}(p') = [\text{var}(p')]^{\frac{1}{2}}$ is the standard deviation of p' and $1-\beta$ is the level of confidence. Since the variance depends on an unknown p, p' is used as an estimate in (22). As an example, suppose that for Figure I.36b samples of one and ten transects are taken and for both $p'=0.05$. Assuming the autocovariance structure given in Table I.8 and computing the variance of the estimate with (22b) the confidence interval estimate of the true area fraction at the 90% confidence level is [0.011, 0.089] for a single transect and [0.038, 0.062] for a sample of ten transects. Neither of these intervals contains the true area fraction $p=0.067$. Of course, the probability of obtaining such a p' from a population with a true fraction of 0.067 is very small, particularly for the set of ten transects (0.01 as opposed to 0.24 for a single transect), so that this example is improbable but useful for illustration. If, on the other hand, we obtain a sample p' of 0.07 then the confidence interval estimate of p is [0.024, 0.116] for a single sample transect and [0.056, 0.084] for a set of ten. Both contain the true area fraction but the larger sample size gives a much smaller range for the estimate.

The shortcoming of this approach is that the autocovariance function must be known. It may be possible to estimate it from the data itself if the sample size is large enough, although this is somewhat circular. In some cases it may be possible to infer a covariance structure by assuming a simple model of the geophysical variable, as done in *Rothrock and Thorndike* (1984) for sea ice floes. Even so, some knowledge of the field is needed; in their case the diameter of the floes. If, however, some basic autocovariance structure can be assumed for different cloud types, sea ice leads, etc., then the above procedure is certainly useful for planning sampling studies, and probably applicable to data analysis as well.

I.5.3 SPECIAL CASE: POISSON PROCESSES

For certain stochastic processes it is possible to determine the fractional area coverage from measurements along a line without any *a priori* knowledge of the process. Here such a possibility is given for a Poisson line process like the one used above as a model of leads.

For a Poisson process the area fraction is related to the intensity[1] τ of the process and the mean "area" of the objects ζ:

$$p' = \text{Prob}[O \text{ is covered}] = 1 - e^{-\tau\zeta} \tag{23}$$

where O is an arbitrary origin. The area measure corresponds in units to the intensity measure; e.g., for leads the intensity is the number of points per unit distance and ζ is mean lead width.

The area fraction can be now estimated from lineal measurements through the use of the line (lead) thickness (width) distribution. The area term in (23) is the overall mean line thickness, W, defined as

---

[1]The *intensity* of a stochastic process is commonly called the *density* of the process. The former term is used here in order to avoid confusion with the concept of probability density.

$$W = \pi^{-1} \int_0^\pi w(\theta)\, d\theta$$

where $w(\theta)$ is the mean thickness of lines with orientation θ ($0 \le \theta \le \pi$) (*Miles*, 1964). This applies to lines oriented isotropically; i.e., with a uniform distribution such that $f_\Theta(\theta) = \pi^{-1}$ where f_Θ is the probability density function for line (lead) orientations. For anisotropic thick lines then

$$W = \int_0^\pi w(\theta)\, dF_\Theta(\theta)$$

where $dF_\Theta(\theta) = f_\Theta(\theta)\, d\theta$, and F_Θ is the cummulative distribution function for orientations. A method for determining the actual lead width distribution, and hence W, from the width distribution measured along a transect has been presented in (*Key and Peckham*, 1991).

As an example of the use of (23), the lead network in Figure I.36b was generated with $\tau = 1/3$ (3 km mean spacing) and $W = 0.2$ km. This gives a p' estimate using (23) of 0.064 compared to the value of 0.067 reported in Table I.8. The discrepency is a function of the image creation and thresholding process, where all leads must fill an entire pixel.

In practice the intensity of the process is not known. For leads modeled as a Poisson line process an estimate of τ can be obtained from the transect data, where the points of intersection of the transect with leads constitute a Poisson process of intensity $2\tau/\pi$. The accuracy of this estimate depends on the size of the region over which the measurements are made. For Figure I.36b estimates of τ range from 0.19 to upwards of 0.45 which results in an estimate of p' in the range of 0.037 to 0.086. There is, of course, some variability in the estimate of W as well, which is discussed in (*Key and Peckham*, 1991).

PART II: RADIATIVE TRANSFER MODELING STUDIES

II.1 RADIATIVE TRANSFER MODELING AND MODEL VALIDATION

In order to utilize radiative transfer models most effectively, we have reviewed how they treat factors such as ice cloud morphology, cloud optical thickness, low level inversions, boundary layer effects, and other aspects relevant to the polar regions. A particular concern is that existing models, cloud properties, standard atmospheres, etc. have typically been developed for low and mid-latitude applications, and may thus contain biases or shortcomings when applied to polar regions. Part of this effort involves incorporating polar atmospheres and cloud properties into the models. Arctic-specific temperature and humidity profiles have been obtained and are discussed in the next section. Unfortunately, little information on the microphysical characteristics of arctic clouds is available. Data that are available, however, were incorporated into the models where appropriate. This is limited primarily to arctic stratus experiments during the early 1980's, and some measurements of aerosols. Additional data is expected to be obtained during LEADEX by instruments on the NOAA P-3.

II.1.1 RADIATIVE TRANSFER MODEL

Work described in this part of the report relies heavily on simulating radiances measured by the AVHRR sensor. To simulate radiances in the AVHRR thermal channels, daily temperature and humidity profiles in each season are used with the LOWTRAN 7 radiative transfer model (*Kneizys et al.*, 1988). Radiances are modeled for sensor scan angles from 0° to 60° in 10° increments. The appropriate sensor response function is applied to the calculated radiances, and radiances are then converted to brightness temperatures. Atmosperic chemical composition, background tropospheric and stratospheric aerosols for the subarctic winter and summer models are used, since no such information is available from the ice islands. The optical properties of Arctic haze have not been extensively measured; model calculations (*Blanchet and List*, 1983) show that the volume extinction coefficient of Arctic haze is generally of the same order of magnitude as that of the tropospheric aerosols. Therefore, the use of tropospheric background aerosols is appropriate.

In order to test some sense of the validity of the radiative transfer model, downwelling longwave irradiances (fluxes) computed with LOWTRAN were compared to measurements at South Pole, Greenland and Denver. Radiosonde data from the three locations were used for the calculations. To obtain irradiance, E, from LOWTRAN (which outputs radiances, L) the calculation was done for four angles (8 streams) and employed the weighting function:

$$E = \pi(0.3626838L_1 + 0.3137066L_2 + 0.2223810L_3 + 0.1012285L_4)$$

where the subscripts of L refer to the sensor zenith angles 79.430°, 58.296°, 37.187°, and 16.201°, respectively. Additionally, a single-angle method (52.5°) was tested and found to give fairly accurate results. The bandwidth of 3.5 - 50 μm used in the calculations corresponds with the bandwidth in which a pyrgeometer measures. The LOWTRAN irradiances differed from the measurements by -4.7% to +5.6%. Assuming 5% accuracy for the pyrgeometer data these results are acceptable. Results for clear sky are listed in Table II.1.

Table II.1. Comparison between modeled and observed longwave fluxes under clear sky conditions.

Station and Date	Measured (W m^{-2})	4 Angles (W m^{-2})	Error (%)	52.5° (W m^{-2})	Error (%)
Denver, 9-30-89	334	336	+0.60	320	-4.19
South Pole, 12-28-86	128	124	-3.13	117	-8.60
South Pole, 7-31-86	71	75	+5.63	71	0.0
South Pole, 11-6-86	107	102	-4.67	96	-10.28

Calculations were also done for cloudy sky conditions. In comparisons of model results and observations, the observed cloud fraction, A_c, must be considered. Here the model is used to estimate clear and overcast fluxes, and these are weighted by the observed cloud fraction.

A remaining problem concerns the differences between the microphysical properties of LOWTRAN's cloud models and those of the observed clouds, which are unknown. Table II.2 gives the results of the cloudy sky comparisons.

Table II.2. Comparison between modeled and observed longwave fluxes under cloudy conditions.

Station and Date Cloud Fraction, Type	Measured (W m^{-2})	4 Angles (W m^{-2})	Error (%)	52.5° (W m^{-2})	Error (%)
Greenland, 7-23-90; 8/8, stratocumulus	309	301	-2.59	301	-2.59
Greenland, 7-26-90 3/8, stratocumulus	283	282	-0.35	275	-2.48
Greenland, 7-1-90 1/8, cirrus	225	227	+0.89	217	-3.56
South Pole, 7-16-86 8/8, cirrus	157	156	-0.64	156	-0.64
South Pole, 11-26-86 8/8, cirrus	126	129	+2.38	122	-3.17

To examine the effect of vertical temperature structure on upwelling longwave radiation, radiances in the three channels were estimated using arctic mean and subarctic standard winter and summer profiles (described below) with identical seasonal surface temperatures. The maximum difference in radiances was 0.05 W m^{-2} sr^{-1} indicating that the vertical temperature distribution of the relatively dry arctic atmosphere plays a very small role in the attenuation of upwelling longwave radiation.

II.1.2 ICE ISLAND DATA

Analyses are based on atmospheric temperature and humidity profiles collected by rawinsonde from a Soviet ice island (NP-26), located at approximately 85° N 170° W during 1983-1987 (Figure II.1). Generally two observations per day were collected covering a vertical range of 0-25 km. Profiles that have at least 10 levels are retained in the analysis. Observations include temperature, dew point depression, wind speed, and wind direction. For the years 1986-87 surface-based cloud observations are also available. These observations include low, middle, and high cloud types, height of the cloud base, and cloud fraction.

Only clear sky profiles are of interest in one of the studies below, and since the satellite thermal radiances under cloudy conditions will reflect cloud top temperature and a significant amount of cloud cover will affect the lower tropospheric temperature structure, clear sky "seasons" that differ in their vertical temperature and humidity structures are then defined. The seasons are determined objectively with a squared Euclidean distance clustering algorithm; the variables are temperature and humidity at each level. To reduce the degree of statistical dependence between levels, only one measurement per kilometer was used. The resulting seasons are winter: October through March, summer: June through August, and transition: April, May, and September. The resulting mean seasonal temperature profiles for clear, cloudy (greater than 75% cloud cover), and mixed conditions are shown in Figure II.2.
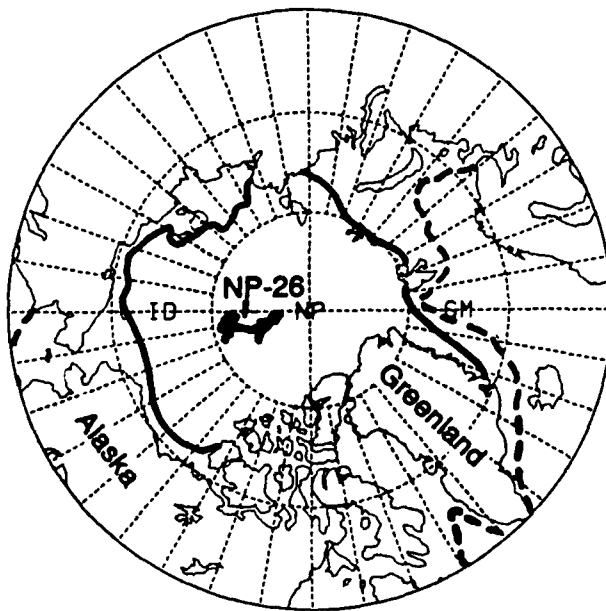

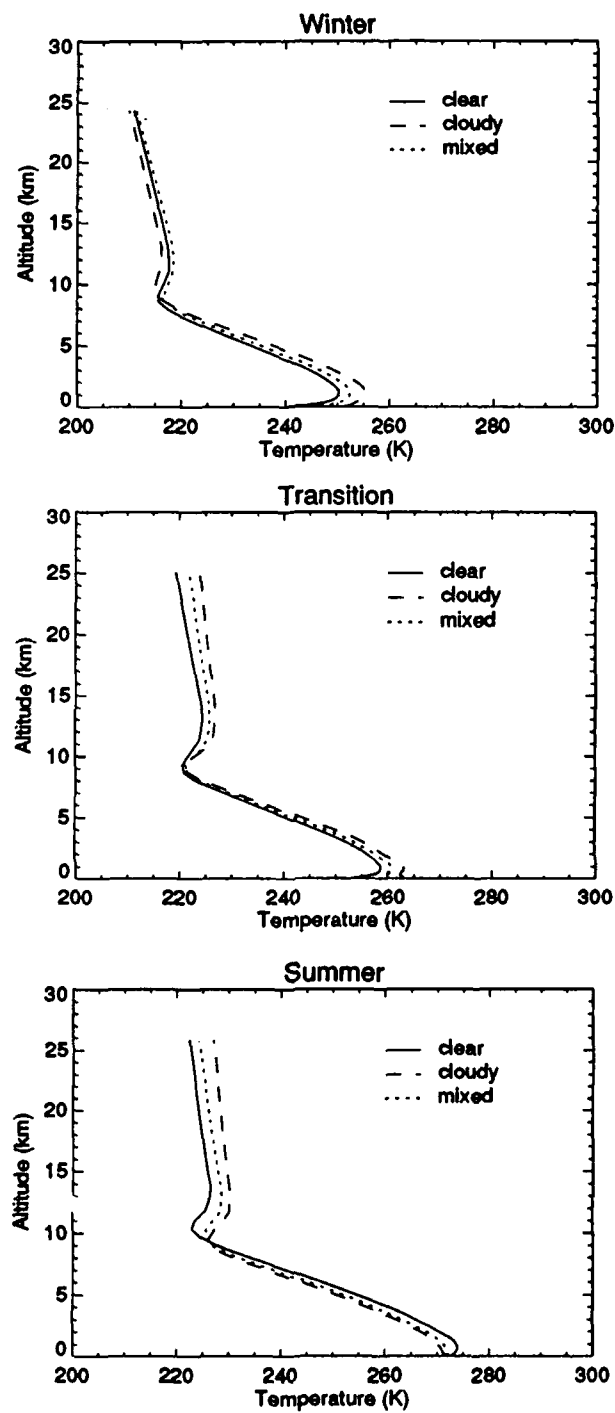Figure II.1. Location of the Soviet ice island NP-26.

Figure II.2. Arctic winter, transition, and summer temperature profiles under clear, cloudy, and mixed conditions from a Soviet ice island located in the Canada Basin.

II.2 ATMOSPHERIC INFLUENCE ON LEAD DETECTABILITY

Here we address the need to understand how different sensors respond radiometrically to varying surface types and intervening atmospheric layers by evaluating the combined use of multispectral image and contrast analyses to determine thresholds of lead detection under varying atmospheric conditions. Our objective is to estimate the narrowest resolvable lead under a given set of surface and atmospheric conditions, sensor FOV and viewing geometry. Although this investigation focuses on the use of AVHRR data, the approach should have general applicability to other thermal sensors of differing spectral response and view characteristics. The modeling results presented here contrast simulations of clear-sky conditions with those including the effects of various types of horizontally homogeneous cloud or aerosol layers. Cloud detection using AVHRR data is not addressed. For a discussion of polar cloud detection see *Key and Barry* (1989), *Sakellariou et al.* (1992) and *Yamanouchi et al.* (1987) and references therein.

Our overall approach is as follows. We first simulate top-of-the-atmosphere (TOA) radiances for three thermal channels of the AVHRR instrument. Average clear-sky January conditions for the central Arctic are assumed. Operating in the NIR and IR "atmospheric window" regions of the spectrum, these channels are especially sensitive to surface emissions, but are also affected by any intervening atmospheric layer that absorbs/emits thermal radiation. Thus, surface (or skin) temperatures and emissivities are varied to evaluate the effects of different surface types. All modeled radiances are converted to equivalent blackbody temperatures (brightness temperatures) by inverting the Planck function (*NOAA*, 1991) to facilitate comparisons with physical temperatures and the analyses of bispectral results (NIR-IR brightness temperature differences) and derived thermal contrasts. Next, model clouds or haze layers are hypothetically inserted into the atmosphere to examine the behavior of simulated brightness temperatures and brightness temperature differences (BTDs) as a function of layer optical depth. These "split window" results are then examined for signatures that characterize haze, stratiform water clouds, clear-sky ice crystal precipitation (ICP) or high level cirrus clouds. Finally, by normalizing the difference between channel brightness temperatures of a lead pixel and its background (i.e. the multiyear ice pack) by the brightness temperature of the background scene *normalized contrast* values are derived and evaluated as a means to determine the limits of lead detection given certain sensor characteristics and atmospheric/surface properties.

II.2.1 RADIANCE SIMULATIONS

The radiative transfer code LOWTRAN 7 (*Kneizys et al.*, 1988) (hereafter simply LOWTRAN) is used to compute top-of-the-atmosphere upwelling radiances from which satellite-derived brightness temperatures are simulated. In cases involving haze, changes in the properties of aerosols as a function of relative humidity (RH) are accounted for (e.g., *Shettle and Fenn*, 1979; *Blanchet and List*, 1987) by first modifying the effective refractive indices of the bimodal particle size distribution and then recomputing extinction and absorption coefficients based on Mie theory (*Kneizys et al.*, 1980).

In this study we simulate AVHRR radiances for channels 3, 4 and 5. Channel 3 measures in the NIR window region of the spectrum and is centered at 3.7 μm while the IR channels 4 and 5 are centered at 10.8 μm and 12.0 μm, respectively. All our calculations include the effects of multiple scattered thermal radiation and are made at steps of 5 cm^{-1} (equivalent to 0.06 μm at 11 μm). The angular and spectral dependencies of snow and water emissivities are also taken into account. In all cases, LOWTRAN was initialized for average clear-sky January temperature and humidity profiles based on an analysis of Soviet ice island data collected in the central Arctic (e.g., *Key and Haefliger*, 1992; *Serreze et al.*, 1992). The mean clear-sky January temperature and dewpoint temperature profiles are shown in Figure II.3 with the boundaries of subsequently prescribed hypothetical layers of haze, stratus cloud, cirrus

cloud and ice crystal precipitation indicated. Because there is essentially no information available on the vertical structure of atmospheric gases in the central Arctic, we assume that average "subarctic winter" concentrations of O_3, CH_4, CO and N_2O exist in the atmosphere when running LOWTRAN. Model subarctic winter background aerosol concentrations for the troposphere (2 to 10 km) and the stratosphere (10 to 30 km) were also prescribed. To simulate haze effects, boundary layer (0 to 2 km) aerosol concentrations were varied by specifying the layer visibility, but in all other cases the default "rural" aerosol model for the boundary layer was used. To examine the full range of AVHRR scan angles (0° to approximately 55°) we made calculations at 0° (nadir), 20° and 50°. Only results for 0° and/or 50° are presented here.
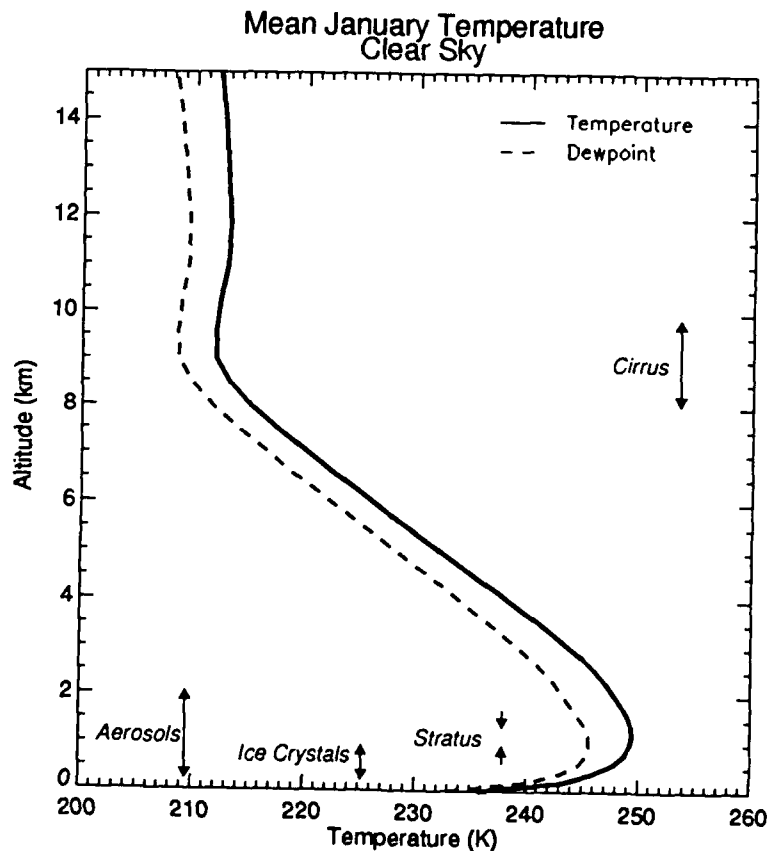

Fig. II.3. Mean clear-sky January temperature and dewpoint temperature profiles for the central Arctic. Also shown are the vertical positions of hypothetical layers of cirrus cloud, boundary layer haze, ice crystal precipitation and stratus cloud that are prescribed for radiative transfer simulations that are described in the text.

II.2.2 INTERVENING ATMOSPHERIC EFFECTS

The effects of four commonly observed atmospheric phenomena in the Arctic are considered: 1) Arctic haze (e.g., *Rahn and McCaffrey*, 1980; *Valero et al.*, 1989; *Valero et al.*, 1983) which persists over large regions of the Arctic, especially during late winter and early spring, 2) Arctic stratus cloud (e.g., *Tsay and Jayaweera*, 1984; *Tsay et al.*, 1989; *Curry et al.*, 1992) which commonly obscures satellite viewing of the sea ice surface in summer, but may be thin enough during the winter months to make lead detection feasible, 3) clear-sky ice crystal precipitation (ICP) which has a significant effect on the radiation balance of the surface/atmosphere system in the Arctic (*Curry et al.*, 1990; *Curry et al.*, 1989a; *Curry et al.*, 1989b) and 4) high level cirrus clouds which are the "most-frequently-occurring cloud type" observed in the central Arctic during winter and spring (*Warren et al.*, 1988). Each of these has a distinct effect on the upwelling thermal radiation emitted from the underlying surface and atmosphere depending on their microphysical properties, geometric thicknesses and positions within the atmosphere. The differences in the radiative properties of atmospheric aerosols (haze), water droplets or ice crystals result in varying degrees of scattering and absorption as a function of wavelength. These differences can be exploited using multispectral techniques to distinguish various types of attenuating layers that may exist in the Arctic atmosphere assuming that the underlying surface properties can be determined by other means.

II.2.2.1 Arctic Haze

The optical properties of Arctic haze have not been extensively measured, but model calculations indicate that the volume extinction coefficients of Arctic hazes are to a first approximation the same order of magnitude as those for tropospheric aerosols (e.g. *Blanchet and List*, 1983; *Tsay et al.*, 1989). Because Arctic haze generally contains an anthropogenic component of carbonaceous material transported from the lower latitudes (*Rosen et al.*, 1981; *Kahl and Hansen*, 1989), the "urban" aerosol model of LOWTRAN was selected to simulate low level haze layers. This model represents a mixture of 20% soot-like aerosols and 80% rural type aerosols contained in the 0 to 2 km boundary layer (*Kneizys et al.*, 1980). The extinction coefficient β for boundary layer haze as defined in LOWTRAN is determined from : prescribed atmospheric visibility V using Koschmieder's formula: $V = 1/\beta \ln(1/\varepsilon)$, where ε is a threshold contrast taken to be 0.02.

The infrared opacity of aerosol layers is known to increase quite dramatically with increasing relative humidity (*Blanchet and List*, 1987; *Shettle and Fenn*, 1979), thus an assessment of how water uptake by hygroscopic aerosols affects simulations of brightness temperatures and BTDs was also made. Results for a saturated haze layer (RH = 99.9%) composed of "wet" aerosol particles are contrasted with those for moderately dry (RH = 70%) haze layers found to characterize mean January conditions in the Arctic. LOWTRAN is designed to modify the absorption and scattering coefficients of aerosol distributions by 1) assuming growth of particulates as a function of RH based on the results of *Hanel* (1976), 2) adjusting their effective refractive indices and 3) recomputing their radiative properties based on Mie theory (*Kneizys et al.*, 1980).

II.2.2.2 Arctic Stratus

Arctic cloud climatologies show marked increases in average low cloud amounts during spring attributed to the presence of stratiform water clouds within the boundary layer which reach a maximum coverage of about 70% during the summer months (*Huschke*, 1969; *Vowinckel and Orvig*, 1970). Stratus clouds have a potentially dramatic impact on the surface-atmosphere heat budget depending on whether their shortwave albedo effects or longwave greenhouse effects dominate the lower tropospheric radiation

balance (*Curry et al.*, 1992). Summertime visible stratus optical depths tend to be large, in cases exceeding 20 (*Herman and Curry*, 1984), thus the use of visible imagery to detect leads is not practical, and because thermal contrasts between leads and multiyear sea ice tend toward zero as cloud opacity increases, detection using thermal imagery is also impractical in most cases. During winter, however, stratus cloud cover is often less than 20% and the cloud layers tend to be thin optically with visible optical depths on the order of 2 (*Curry et al.*, 1992). Detecting leads using thermal imagery in winter may, therefore, be possible. Using the LOWTRAN model for "stratus" we assess the feasibility of detecting leads during winter by assuming that a horizontally homogeneous cloud layer 380 m thick exists in the lower atmosphere as indicated in Figure 1. For stratus simulations the desired range of visible (0.55μm) optical depth τ was obtained by varying the conversion factor from equivalent LWC (g m⁻³) to extinction coefficient (km⁻¹) in the LOWTRAN code (*Kneizys et al.*, 1988). The stratus droplet size distribution is represented by a modified gamma distribution:

$$n(r) = 27 r^2 e^{-0.6r}$$

where r is the droplet radius and n is number density. The total number density is taken to be 250 cm⁻³ and the mode radius is 6.67μm (for mass distribution). Details of the LOWTRAN cloud models are given in *Shettle et al.* (1988).

II.2.2.3 Layers of Ice Crystals

Both the high level cirrus cloud and low level ice crystal precipitation simulations were made by inserting the LOWTRAN "standard" cirrus model (*Shettle et al.*, 1988) into the atmosphere at the vertical positions indicated in Figure II.3. For both conditions the desired range of optical depth was obtained by assuming the appropriate values of 0.55μm volume extinction coefficients for a 2 km thick cirrus based at 8 km and a 1 km thick ICP layer based at the surface. Note that ice crystal precipitation has been observed from the surface to heights exceeding 3 km in the Arctic, but it is most frequently observed below about 1 km (*Curry et al.*, 1990).

For all of the cases discussed above theoretical calculations were made for a visible optical depth range of 0 (clear-sky) to 100, but results are presented only for values between 0 and 10. Realistic layer thicknesses and extinction values of aerosols and ice crystals are such that visible optical depths rarely exceed 10 and although stratus optical depths may exceed this value during the summer months, low thermal contrasts and high visible opacity preclude lead detection at this time of year. In the winter, even when mixed-phase layers contain small amounts of liquid water, optical depths are generally within the range represented here.

II.2.3 SURFACE CHARACTERISTICS

Model runs were initialized for three different surface temperatures to characterize open or refrozen leads and a fourth temperature representing the surrounding ice pack which is assumed to be 2 m thick and in equilibrium with the surface air temperature. In the discussion that follows, the terms "skin" and "surface" temperature are used interchangeably and should not be confused with shelter temperature (measured 2 m above ground level) which is generally higher than the actual skin temperature when a surface-based temperature inversion exists. Shelter temperature may differ from skin temperature by more than 10°C depending on the region and time of year (e.g., *Stowe et al.*, 1988, *Rossow et al.*, 1989). The following temperatures were computed to represent a range of lead types: for open leads, 271 K; for leads covered by 5 cm thick ice, 256 K; and for 15 cm thick leads, 248 K. The ice pack was

assumed to be in thermal equilibrium with the surface air and was assigned the temperature of 235 K corresponding to the first rawinsonde level.

All surfaces with the exception of open leads are assumed to be snow-covered and directional snow emissivities were modeled following the procedure in *Dozier and Warren* (1982). This method involves calculating the single scattering albedo, asymmetry factor and phase function for snow grains using a Mie code before determining the directional, wavelength-dependent emissivities using the delta-Eddington approximation of the radiative transfer equation. These emissivities were then integrated over the response function for each channel *i*:

$$\varepsilon_i(\theta) = \frac{\int_{\lambda_1}^{\lambda_2} \varepsilon(\lambda,\theta)\phi_i(\lambda)\ d\lambda}{\int_{\lambda_1}^{\lambda_2} \phi_i(\lambda)\ d\lambda}$$

where $\varepsilon(\lambda,\theta)$ is the emissivity in direction θ at wavelength λ and ϕ_i is the ith sensor response function. *Key and Haefliger* (1992) note that differences between the integrated emissivities for the NOAA series 7, 9, and 11 AVHRR sensors are on the order of 0.0001. In the current study we use the NOAA 7 values only. For brightness temperature simulations over open leads, the angular dependence of channel emissivities of water are determined through Fresnel calculations. Table II.3 gives the angular emissivities used in the current analysis as a function of AVHRR scan angle and surface type. In reality, newly refrozen leads are clear of snow, thus pure ice emissivities should be used for best results. However, the authors are aware of no comprehensive set of measurements nor method from which the spectral, directional emissivities of planar ice can be determined. The emissivity of ice approaches unity and is often assumed to be 1.0 for field investigations (e.g., *Konig-Langlo and Zachek*, 1991). A more accurate value may be 0.97 (*Hobbs*, 1974) which is within 2% of the snow values listed in Table II.3. Thus, the assumption that all surfaces are snow-covered will not result in serious errors in simulated brightness temperatures nor will differences in channel brightness temperatures or contrast ratios be affected significantly.

TABLE II.3. Angular emissivities of snow and water in NOAA 7 AVHRR channels 3, 4 and 5 at two satellite scan angles.

Channel	Snow		Water	
	0°	50°	0°	50°
3	.998	.992	.976	.961
4	.999	.996	.992	.984
5	.996	.987	.986	.972

For even more accurate simulations of brightness temperatures, channel radiances should also be integrated over the appropriate sensor response functions. These vary from one satellite to another as

discussed in *Key and Haefliger* (1992). In that study, they found that by using the full response functions instead of assuming rectangular functions (i.e., 100% response at all wavelengths within the portion of the channel where the actual response is at least 50%) the brightness temperature differences were only on the order of 0.05 K for channel 4, but were about 0.5 K for channel 5 assuming typical January conditions in the central Arctic. Because we focus here on channel 4 results, we use the rectangular function for all simulations rather than performing this time-consuming integration. This is justified in that the computation of normalized contrasts are based on differences and ratios of brightness temperatures at one or another wavelength so that small absolute biases due to differences in response functions have a negligible effect on the final results.

II.2.4 RESULTS

II.2.4.1 *Simulated Brightness Temperatures*

Examples of channel brightness temperatures as a function of visible (0.55 μm) optical depth are shown in Figure II.4 for boundary layer haze, ice crystal precipitation and high-level cirrus clouds at 0° and 50° satellite scan angles for channels 3, 4, and 5 of the AVHRR instrument. These layers were positioned as shown in Figure 1 and mean January temperature and humidity profiles were assumed. Within each panel (from top to bottom) are plots that relate to the different prescribed surface temperatures representing open leads, leads of 5 cm and 15 cm thickness (271 K, 256 K and 248 K, respectively), and the multiyear pack ice (235 K). Note that the boundary layer is moderately dry during January in the central Arctic with RH averaging about 70% between the surface and 2 km suggesting a predominance of clear skies containing low concentrations of dry aerosols during this time of the year. At zero optical depth the physical surface temperatures are reasonably well represented by simulated channel brightness temperatures because the selected channels are all within NIR and IR window regions of the spectrum where sensitivity to the relatively dry Arctic atmosphere is least and because open water, newly refrozen leads and snow-covered surfaces all have high emissivities. Regardless of the underlying surface type, channel 3, 4 and 5 brightness temperatures tend to converge to the blackbody radiating temperature of the top of the intervening cloud or haze layers as optical depths increase, though the rate of convergence varies depending on the microphysical properties of the intervening layer and the layer's position and mean temperature relative to the surface. Scan angle effects are also apparent by comparing corresponding panels for 0° and 50° viewing angles. No matter what type of surface or intervening medium exists, the convergence of simulated brightness temperatures to layer top temperatures occurs faster when viewing off-nadir. This is due to the increase in optical path length by a factor $1/\cos(\theta)$, where θ is the satellite scan angle as viewing angles increase from nadir.
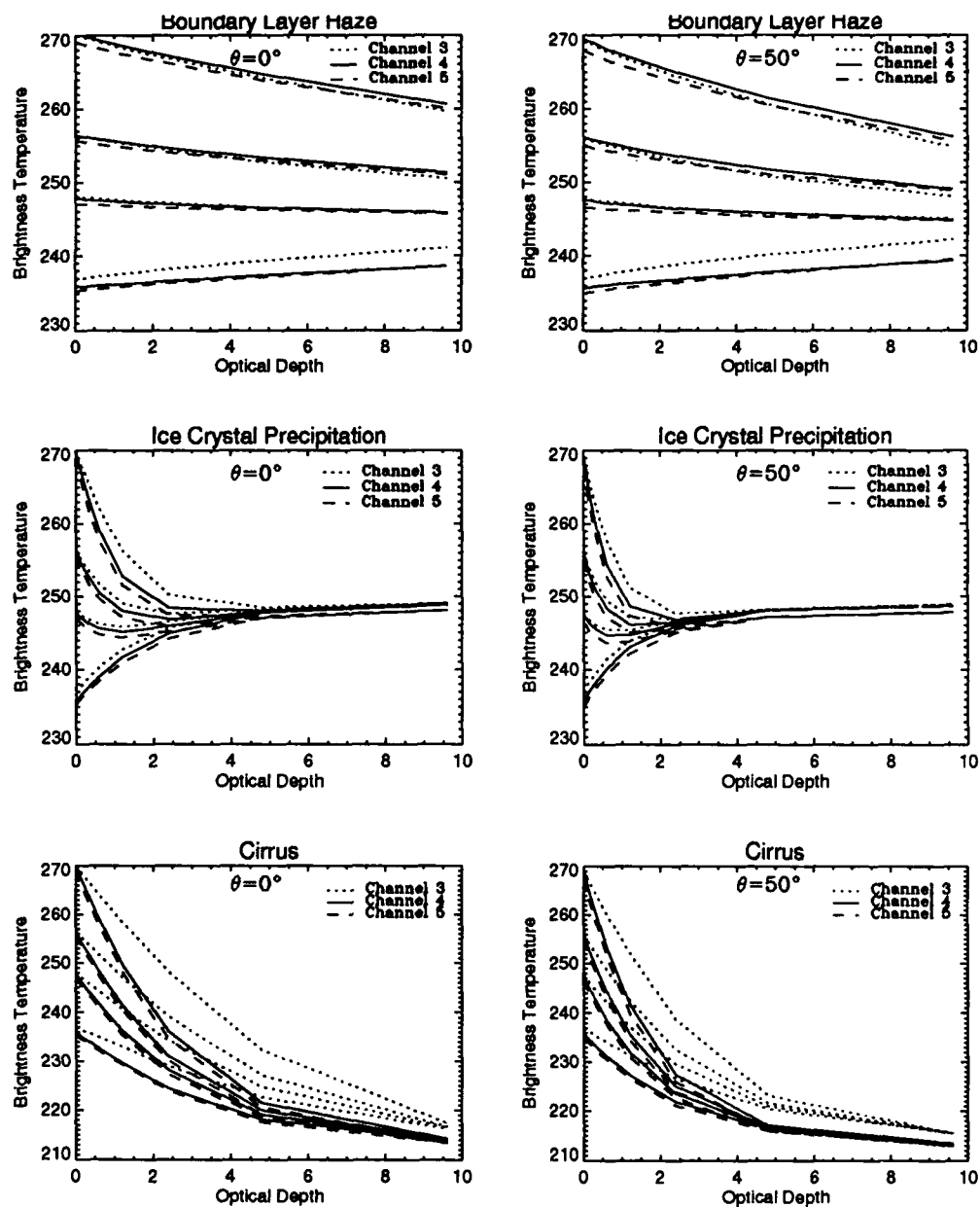
Fig. II.4. Simulated brightness temperatures for layers of boundary layer haze, ice crystal precipitation and high-level cirrus cloud for three AVHRR thermal channels assuming four surface types (from top to bottom at left of each panel): open water, 5, 15, and 200 cm thick ice. Results are shown for satellite view angles of 0° and 50° over a range of 0.55μm optical depths between 0 and 10. Mean clear-sky January temperature and humidity profiles for the central Arctic are assumed.

Because haze particles absorb and emit much less NIR and IR radiation than do ice particles or water droplets at a given visible optical depth, haze layers neither attenuate nor enhance significantly the thermal emissions from the surface. Thus, simulated NIR and IR brightness temperatures during typical winter conditions are not very sensitive to changes in aerosol loading in the boundary layer. In these situations, the relatively dry haze layers become essentially black at visible optical depths exceeding 95 (equivalent to an infrared optical depth of about 6). This extreme value corresponds to an unrealistic visibility of less than 85 m. As noted by *Blanchet and List* (1987), however, the infrared opacity of aerosols increases dramatically as relative humidity increases. In fact, IR optical depths may exceed those for visible wavelengths in saturated haze layers. This phenomenon occurs due to the uptake of available water by hygroscopic particles such as sulfuric acid and deliquescent compounds within the layer causing a shift to a larger particle size distribution and corresponding enhancements of the absorption and scattering cross sections of the particles.

We evaluated the effects of increasing relative humidity on aerosol layers by hypothetically saturating the 0 to 2 km layer and recalculating the brightness temperatures for a "wet" aerosol layer. This is easily accomplished using LOWTRAN because the absorption and scattering coefficients are modified in accordance with hygroscopic growth as described previously. The optical depth dependence of channel 4 brightness temperatures for a haze layer with mean RH = 99.9% was found to be virtually identical to that for a haze layer having RH = 70% while channel 5 brightness temperatures tended to converge slightly faster to the blackbody temperature of the layer. The NIR channel 3 simulations revealed the most pronounced change due to saturation. They indicated slightly faster convergence with increasing optical depth than either of the IR channels and also, interestingly, NIR values converge to a temperature below the physical temperature of the layer top. This leads to negative NIR-IR spectral differences. Qualitatively, an optically thick, saturated haze layer has similar radiative behavior as does a stratiform water cloud. As these layers increase in opacity they become black to infrared radiation resulting in a rapid convergence of brightness temperatures (no matter what the underlying surface is) to the physical temperature of the layer top; but in the NIR, thick layers totally attenuate the upwelling radiation from the surface while contributing little to TOA radiances because these layers have low NIR emissivities. Thus, NIR brightness temperatures are actually colder than corresponding IR values (e.g., *Yamanouchi et al.*, 1987). These are important considerations because the relative magnitudes of NIR-IR bispectral differences as a function of relative humidity, phase and optical depth may be exploited to distinguish different types of intervening atmospheric layers.

The importance of knowing the vertical position of an intervening layer is apparent by comparing the results for the low level ICP with those for high cirrus clouds. Both layers have identical microphysical and radiative properties based on the standard LOWTRAN cirrus model. However, their net radiative effect on the upwelling radiation field differs significantly because of their relative temperatures and proximity to the nearly black underlying surfaces. Brightness temperatures above the ICP layer converge more rapidly with increasing optical depth than do corresponding temperatures above cirrus because the top of the ICP layer coincides with the warmest region of the atmosphere which is directly influenced by surface emissions. Radiation emitted by the surface contributes significantly to the total upwelling radiation through absorption and secondary emission by the ICP layer at a relatively warm layer temperature. A similar radiative effect occurs in the case of cirrus, but the cold, dry atmosphere below the cirrus layer has little effect on the upward radiative flux and the cloud particles themselves absorb and re-emit this radiation at a much colder temperature. As with haze and stratiform water clouds, these different radiative effects give rise to distinct signatures of brightness temperatures and bispectral differences as a function of optical depth.

II.2.4.2 *NIR-IR Bispectral Differences*

Differences in BTD signatures for combinations of surface and layer types as a function of optical depth may be used to distinguish varying surface and atmospheric properties within a satellite scene, a necessary step in developing a lead detection algorithm. For example, at a cirrus optical depth of about 3.0 the BTD between channel 3 and channel 4 (T_{b3} - T_{b4}) over an open lead is approximately 13K whereas this difference is only about 2K if a low level ICP layer of equal optical depth is present as viewed at nadir.

To more clearly illustrate the potential use of split window imagery to distinguish between various cloud and aerosol layers that are common in the Arctic Figure II.5 was constructed. Shown are values of (T_{b3} - T_{b4}) for three different layers already discussed, dry (70% RH) and wet (99.9% RH) haze layers within the boundary layer and ICP in the lowest kilometer of the atmosphere, and in addition, results are given for the stratus layer described above and shown in Figure II.3. Each panel includes plots of the simulated T_{b3} - T_{b4} values for the four surface types assuming a scan angle of 0°. It is clear that bispectral differences are sensitive not only to optical depth but also to relative humidity and the phase of the particles. Bispectral signatures for dry aerosols are insensitive to increasing optical depth except for those related to multiyear ice. Under saturated hazy conditions there is a distinct monotonic decline in BTDs with increasing τ over all surface types with negative values observed except over multiyear ice when τ ≤ 5. Such separations between multiyear ice signatures and other surface types should permit better identification of background pixels needed to normalize thermal contrasts for the purpose of distinguishing leads. If a stratus layer is present within the warm region of the atmosphere a sharp fall-off to significantly large negative values occurs in the range of optical depths between 0 and about 2.5 with a converging upward signal as τ increases further. In the case of a low-lying ICP layer positive differences of 0.5K to 3.5K peaking between optical depths of 0.5 and 1.5, are apparent whereas for a similar (cirrus) layer placed high in the atmosphere BTDs as large as 13K were noted for τ ≈ 2.5 (see Figure II.4). In theory, if TOA NIR and IR radiances can be measured accurately much information can be extracted by analyzing bispectral images. Unfortunately, the AVHRR channel 3 data is reported to be too noisy to be useful for cloud detection at cold temperatures (*Yamanouchi et al.*, 1987), but hopefully, future spaceborne radiometers will provide data of sufficient quality to resolve the signatures described here.
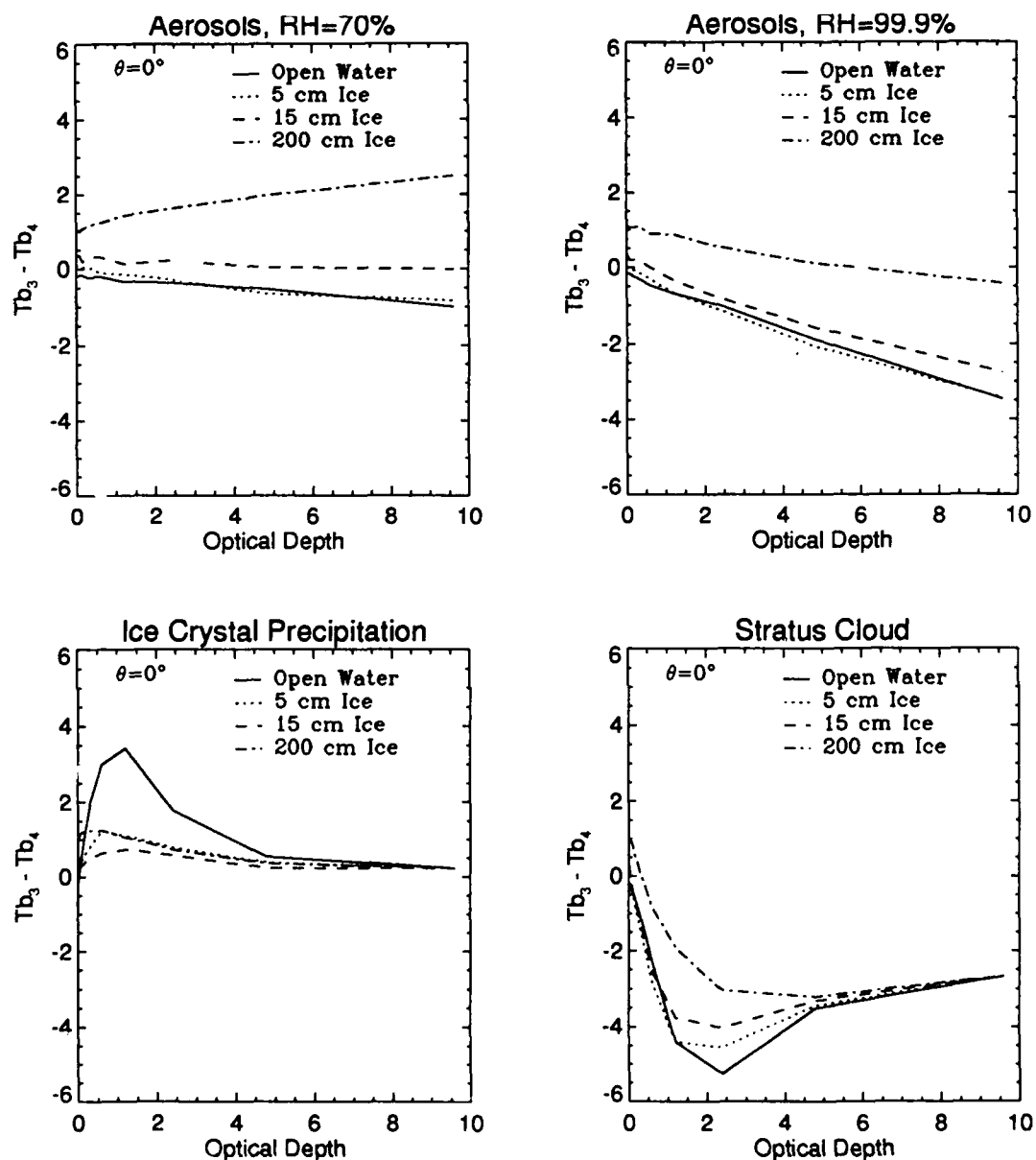
Fig. II.5. AVHRR channel 3 minus channel 4 brightness temperatures as a function of 0.55 μm optical depth for four intervening layer types: aerosol layers having mean relative humidities of 70% and 99.9%, respectively, ice crystal precipitation and stratus cloud. Brightness temperature differences are shown for the four surface types described in the text.

II.2.4.3 *Normalized Atmospheric Contrast*

Normalized atmospheric contrast is a wavelength dependent quantity, varying with atmospheric opacity, expressed in terms of the brightness temperature difference between any given pixel and the background scene normalized by the brightness temperature of the background (in this case taken to be the 2 m thick multiyear ice):

$$C(\tau,\lambda) = \frac{T_T(\tau,\lambda) - T_B(\tau,\lambda)}{T_B(\tau,\lambda)} \tag{1}$$

where T_T is the brightness temperature of the target (lead) and T_B is the back ..ound brightness temperature. Hereafter, in all expressions involving contrast the wavelength dependence is assumed and the λ is omitted. Figure II.7 shows the behavior of this quantity for IR channel 4 derived from the results presented in Figure II.4. This measure of contrast provides a potentially powerful means to detect leads using thermal imagery both for daytime and nighttime conditions. Although, in most cases, Figure II.6 indicates a rapid decrease in normalized contrasts as optical depth increases, realistic cirrus, ICP or haze optical depths are generally within a range that should permit the resolution of leads using thermal contrasts provided that radiances can be measured accurately, sensor field-of-view is small relative to lead widths and full use of ancillary data is made. *Curry et al.* (1990) for instance, measured ICP visible optical depths ranging from about 0.03 to 20, but in five out of seven cases τ was less than about 5, within a range in which thermal contrast should be measurable. With regard to cirrus, even for large extinction coefficients their optical depths are limited because they are confined to regions of the upper troposphere bounded above by the tropopause. As an example, a cirrus cloud having a large visible volume extinction coefficients, say $\kappa_{ext} = 0.2$, 7 km thick ($\Delta Z = 7.0$) would have an optical depth of only 1.4, where $\tau = \kappa_{ex}\Delta Z$. Such large extinctions would exist only for cirrus composed of very large ice crystals with proportionally large total ice .vater contents (IWCs) (e.g., *Stone et al.*, 1990) which occur rarely in extremely cold environments (e.g., *Stone*, 1992; *Platt and Harshvardhan*, 1988; *Heymsfield and Platt*, 1984). In cases involving haze, the aerosol loading would need to be extreme before thermal contrasts diminished significantly. There is no observational evidence that aerosol layers can attain optical depths that would preclude lead detection using thermal imagery. For instance, mean 0.5 µm optical depths for haze layers observed over Barrow, Alaska, even when nearly saturated, were only about 0.2 (*Mendonca et al.*, 1981) and the maximum 0.5 µm optical depth measured during what has been described as a "megahaze" event was about 0.7 (*Dutton et al.*, 1989). Of course, mixed phase haze layers containing large concentrations of ice crystals will tend to attenuate thermal radiation much like pure ICP layers do.

Fig. II.6. Differences between AVHRR channels 3 and 4 brightness temperatures as a function of boundary layer haze optical depth at 0.55μm during the day (thick lines) and at night (thin lines) over each of the four surface types described in the text. Satellite scan angle is 50°, solar zenith angle is 75° and solar azimuth angle is 30°.
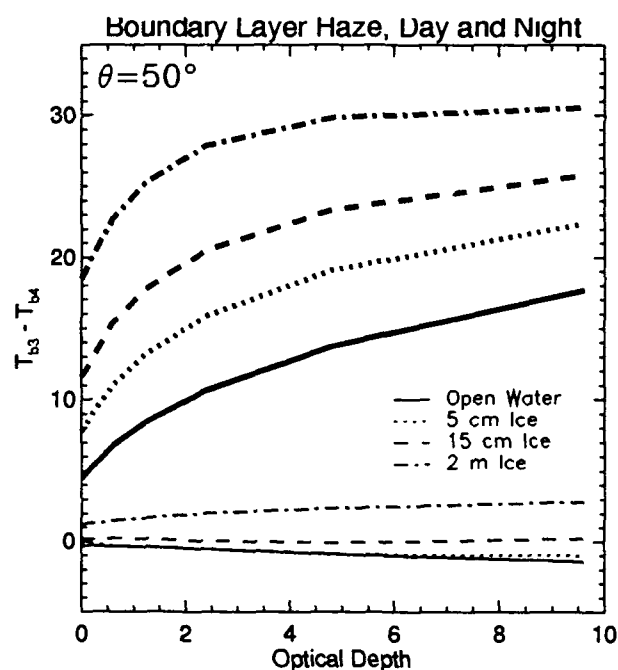
Finally, channel contrasts for the 380 m thick stratus cloud (computed but not shown) were also analyzed to evaluate whether or not leads are detectable during winter when stratus layers tend to be optically thin. IR channel brightness temperatures for the four surface types were observed to converge in a similar manner as was noted for the boundary layer ICP (Figure II.4), thus simulated IR contrasts under the influence of stratus clouds are nearly equal to those computed for the ice crystal precipitation layer shown in Figure II.7. The convergence of channel 3 brightness temperatures with optical depth was found to be even more rapid than for the IR channels so that NIR contrast values diminish more quickly with optical depth. Both IR and NIR contrasts are likely to be below measurable threshold values (discussed below) to make lead detection possible when stratus layers are present because their optical depths are typically in the range of 2 or greater. Our simulations indicate that normalized contrasts will be very difficult to resolve at this level of opacity.
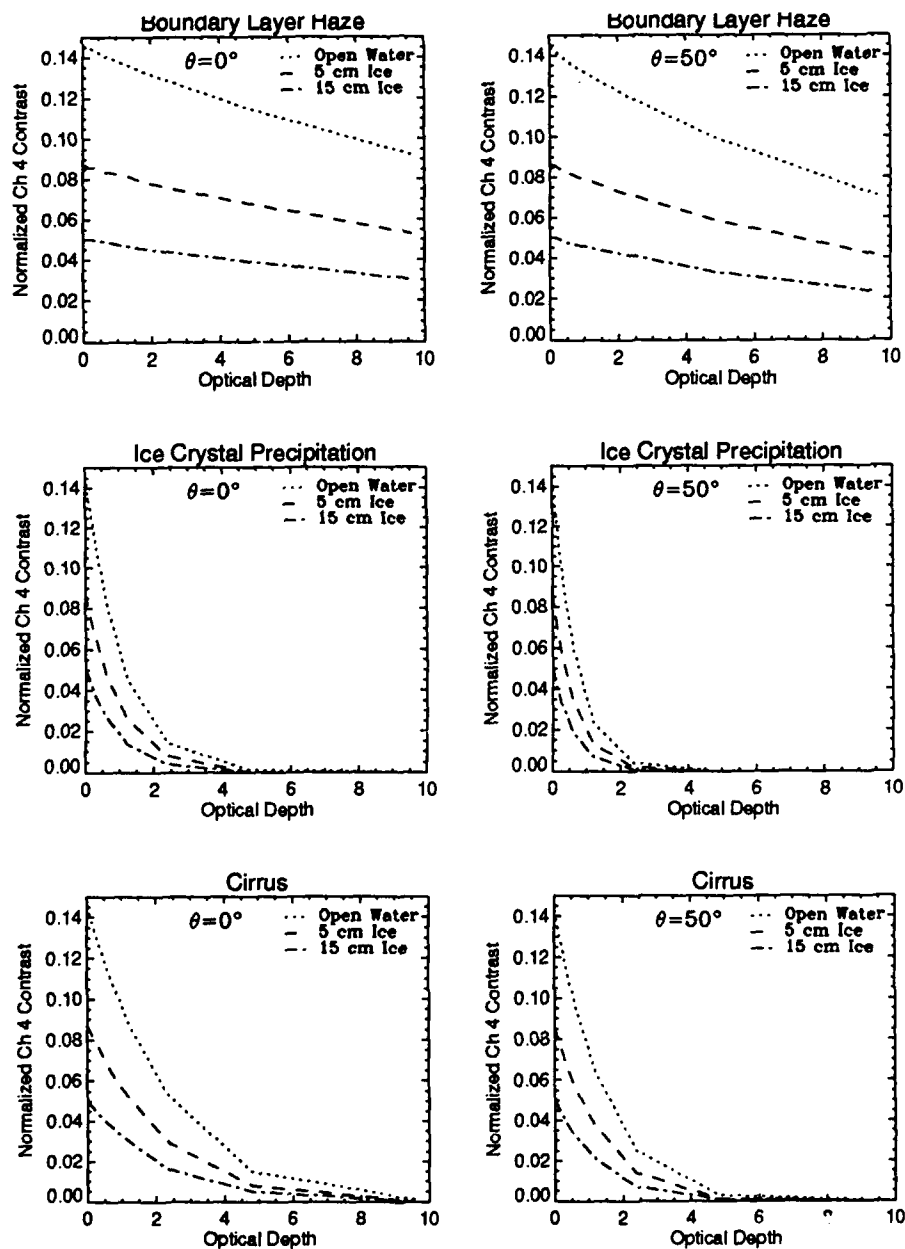
Fig. II.7. Normalized AVHRR channel 4 contrasts between three lead ice thicknesses (open water, 5 cm and 15 cm ice) and the background 2 m thick ice for boundary layer haze, ice crystal precipitation and high-level cirrus cloud as a function of 0.55μm optical depth. Results are shown for satellite view angles of 0° and 50° derived from the brightness temperatures shown in Figure II.4.

II.2.4.4 *Lead Detection Based on Critical Contrast*

The normalized contrast $C(\tau,\lambda)$ in (1) is defined in terms of the target (lead) and background (multiyear ice) temperatures but says nothing about the geometrical characteristics of the target or imaging system. In such a context it assumes that a given lead pixel is completely within the FOV of the satellite radiometer. We now examine how contrast varies as a function of lead width and sensor field-of-view to account for image pixels that contain both lead and multiyear ice surface types.

Letting p be the fractional area covered by a lead within a pixel; i.e., $p = width/FOV$, the *total contrast* C_{tot} that takes into account the reduction in temperature contrast due to atmospheric and spatial effects is

$$C_{tot}(\tau) = \frac{[pT_T(\tau) + (1-p)T_B(\tau)] - T_B(\tau)}{T_B(\tau)}$$
$$= pC(\tau)$$

If every pixel in the image is to be labeled as either a lead pixel or a background pixel, then some thresholding operation must be used. One possible method is to choose as a threshold the mean background temperature plus some multiple of its variability σ, say $T_B(\tau)+2\sigma$. (In reality σ may also be a function of τ.) As in (1), this threshold can also be expressed as a normalized (non-dimensional) contrast ratio:

$$\gamma = \frac{2\sigma}{T_B(\tau)}$$

If the observed total contrast of a pixel is less than this value, then the pixel is not a lead pixel. This *threshold contrast* includes implicitly the effect of the fractional area covered by a lead within a pixel; i.e., it is a total contrast. Low values of γ will generally result in more pixels being labelled as lead pixels because the background is more homogeneous if σ is small. Thermal features should be more distinguishable when contrasted with a more homogeneous background scene. γ can also be defined in terms of some critical normalized atmospheric contrast:

$$C^*(\tau,\gamma) = \frac{\gamma}{p}$$

where the asterisk represents a critical (cutoff) value. This expresses the normalized atmospheric contrast necessary for a lead to be detected if an intervening layer of optical depth τ is present.

To address the question of what minimum lead width can actually be resolved under specified atmospheric conditions and sensor FOV, we need to eliminate hypothetically the atmospheric effects and account for varying FOV. We therefore define the *critical contrast* of a lead as the normalized atmospheric contrast at zero optical depth $C^*(\tau=0,\gamma)$. We can relate $C^*(\tau,\gamma)$ back to the critical contrast $C^*(\tau=0,\gamma)$ with the data provided in Figure II.7 in the following manner. Nadir viewing is assumed. A log surface is fitted to the contrast data for ICP and cirrus cloud, while a planar surface is fitted to the aerosol contrast data. Least squares regression is employed where the independent variables are the actual brightness temperatures at $\tau=0$ of the three lead types and optical depth. The dependent variable is contrast:

$$C_i^{*'}(\tau) = a_i + b_i T_T(\tau) + c_i \tau$$

where the subscript i denotes aerosol, ICP or cirrus cloud; $C^*_i = \ln(C^*)$ for ICP or cirrus cloud and $C^*_i = C^*$ for an aerosol layer. For a given width to FOV ratio p, optical depth τ and threshold contrast γ, the target brightness temperature T_T is estimated for the appropriate background temperature from Figure II.4. T_T is then used in the regression equation above to determine the atmospheric contrast at that optical depth. Inverting the equation and setting τ equal to 0 gives the critical contrast $C^*(\tau=0,\gamma)$. As discussed earlier, IR brightness temperatures at $\tau=0$ are very close to the physical surface temperatures because these surfaces have emissivities approaching unity and the low water vapor content of the atmosphere has a negligible influence on the upwelling radiation.

Figure II.8 shows critical normalized contrast contours for leads as a function of p and optical depth for haze, ICP and cirrus cloud at two assumed values of γ. As mentioned above, it is unlikely that contrasts in the presence of stratus clouds can be sufficiently resolved for realistic values of stratus optical depth to permit lead detection, therefore stratus is omitted from this analysis. The contours in Figure II.8 indicate the critical contrast that a pixel must exceed in order to be designated as a lead pixel for the assumed threshold contrast γ, again assuming mean clear-sky January conditions in the central Arctic. Such plots can be used to estimate the minimum lead width resolvable in an AVHRR channel 4 image under certain conditions in the following manner. Assume, for example, that the sensor's resolution is 1.0 km (FOV = 1.0) at nadir and a 1 km thick ICP layer is present above the surface. If we prescribe a normalized contrast threshold of 0.04 and a critical contrast of 0.2 as detection criteria, then Figure II.8 can be used to estimate the narrowest resolvable lead in a channel 4 AVHRR image as a function of the layer's optical depth. For an optical depth of 8, the width/FOV ratio is 0.35 thus, the narrowest detectable lead would be 0.35 km wide. Under these conditions, any lead less than about 350 m wide would *not* be detectable if the ICP optical depth exceeded 8.0. Following the same procedure but assuming an ICP optical depth of 1, the minimum detectable lead width is about 0.22 km given equal threshold criteria. If we now relax the threshold criteria and do the same analysis for $\gamma = 0.02$, then a lead would need to be only about 180 m wide in order to be resolved at a pixel resolution of 1 km if $\tau = 8$, or 110 m wide if $\tau = 1$. For any given combination of optical depth, contrast threshold and critical contrast the minimum detectable lead width will be systematically smaller if, instead of ICP, a haze layer is present and slightly greater if cirrus cloud is present based on this technique and the theoretical results presented in Figure II.8.

It is suggested here that bispectral techniques be used in conjunction with image contrast analyses to develop an operational procedure to detect and map leads in the polar regions. However, because a continuum of signatures exist depending on atmospheric, surface and geometric effects, it will be essential to constrain the problem by first determining the state of the atmosphere and surface using a combination of multispectral techniques. Of particular importance will be the retrieval of surface temperatures (e.g., *Key and Haefliger*, 1992) because the thermal contrast between leads and the background ice pack may be a key parameter for determining the threshold of lead detection under various conditions.
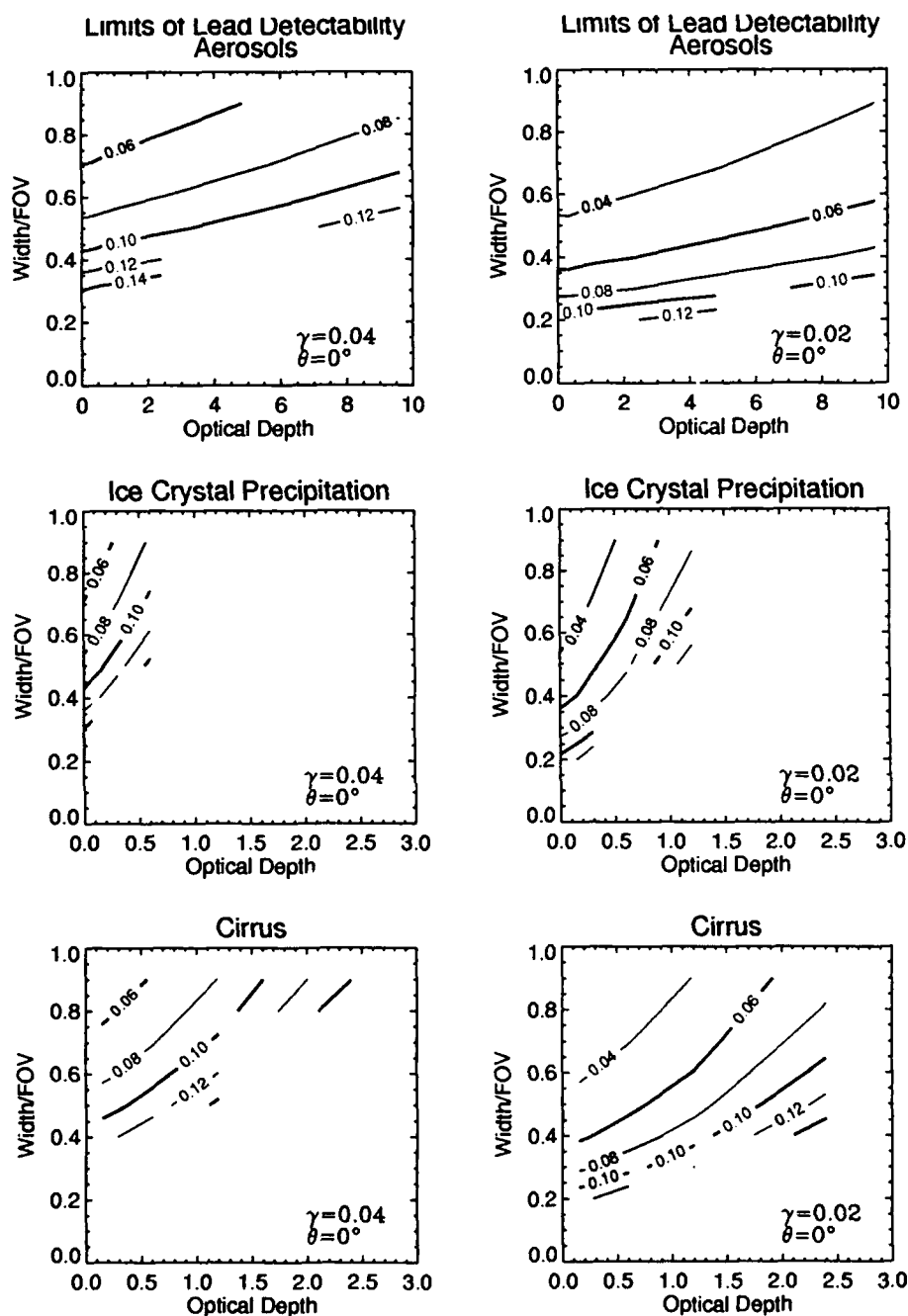
Fig. II.8. Critical contrast of a lead as a function of its fractional coverage within an image pixel (width/FOV) and the 0.55μm optical depth of aerosols (haze), ice crystal precipitation and cirrus cloud. For a given set of geometrical and atmospheric conditions the contours indicate the minimum contrast (at an optical depth of zero) that must exist in order for a lead to be detectable for specified values of threshold contr... γ assuming a satellite viewing angle of 0°. Mean clear-sky January conditions for the central Arctic are assumed. Results are given for two values of threshold contrast: γ=0.04 and γ=0.02 as defined in the text.

II.2.5 DISCUSSION

The theoretical results presented above are enlightening, but we have obviously oversimplified the problems associated with lead detection. We have presented results that only represent average January conditions in the central Arctic and consider only four discrete surface types and four idealized hypothetical models to simulate what in nature is a complicated mix of intervening atmospheric effects. In reality, any of these variables assume a continuum of values that change spatially and temporally. Clouds and aerosol layers are naturally inhomogeneous having physical, radiative and microphysical properties that vary in space and time and frequently occur as multiple layers of mixed phase particles. Intense winds, for example, dynamically force stratiform layers sometimes creating banded structures, especially for layers composed of condensed particles downwind of leads. The detection of leads is further complicated by constantly changing viewing geometries related to sensor FOV, satellite scan angle (and sun angle if daytime conditions exist). Non-linear radiative effects are caused by increasing optical paths at the same time that pixel resolution degrades with increasing scan angle. To develop an operational lead detection algorithm, highly parameterized models will need to be used, perhaps in conjunction with comprehensive "look-up" tables listing expected contrast values and corresponding BTDs for a realistic range of combined surface and atmospheric properties. Furthermore, a step-wise approach will be necessary utilizing ancillary information to further constrain the problem. The use of cloud clearing algorithms is essential to assure accurate surface temperature retrievals and remote sounding techniques need to be improved in order to resolve atmospheric temperature and humidity profiles and to determine the physical, radiative and microphysical properties of intervening layers. Theoretically, multispectral analyses provide a basis for estimating these properties, but in reality it may be years before prototype methods are validated and approved for operational use.

II.3 ICE SURFACE TEMPERATURE RETRIEVAL

The ability to retrieve surface parameters from satellite data in the polar regions is constrained by our limited knowledge of atmospheric temperature, humidity, and aerosol profiles, the microphysical properties of polar clouds, and the spectral characteristics of the wide variety of surface types found there. In this section we present results in the retrieval of ice surface temperature (IST) from the thermal channels of the Advanced Very High Resolution Radiometer (AVHRR) sensors on-board the NOAA series satellites.

Sea and land surface temperature (SST and LST) retrieval algorithms have been developed using the thermal infrared window portion of the spectrum, with the degree of success dependent primarily upon the variability of the surface and atmospheric characteristics. The general approach to estimating surface temperature is to relate satellite observations to surface temperature observations with a regression model. Lacking sufficient observations, however, satellite radiances or brightness temperatures can be modeled by application of the radiative transfer equation. This approach is commonly used for SST retrieval.

To our knowledge, little effort has been directed to the retrieval of the sea ice surface temperature (IST) in the arctic, an area where the first effects of a changing climate are expected to be seen. The reason is not one of methodology, but rather our limited knowledge of atmospheric temperature, humidity, and aerosol profiles, the microphysical properties of polar clouds, and the spectral characteristics of the wide variety of surface types found there. We have developed a means to correct for the atmospheric attenuation of satellite-measured clear sky brightness temperatures used in the retrieval of ice surface temperature from the split-window thermal channels of the AVHRR sensors on-board three of the NOAA series satellites. These corrections are specified for three different "seasons" and as a function of satellite viewing angle, and are expected to be applicable to the perennial ice pack in the central Arctic Basin (Figure II.1). We do not develop a completely new methodology; instead we modify a standard procedure for use with arctic-specific data. It is assumed that a valid cloud-clearing algorithm exists and that only clear sky radiances are being examined. The cloud clearing problem in polar satellite data is not trivial, however. For a review of polar cloud detection algorithms, see *Key and Barry* (1989) and *Sakellariou et al.* (1991).

For the retrieval of IST a multi-channel algorithm that uses empirical relationships to correct for water vapor absorption is employed:

$$T_{ice} = a + bT_4 + cT_5 + d[(T_4 - T_5)\sec\theta]$$

where T_4 and T_5 are the satellite-measured brightness temperatures (K) in the AVHRR thermal channels and θ is the sensor scan angle. The coefficients are determined through a least squares regression procedure, where surface temperatures are regressed against modeled brightness temperatures.

AVHRR thermal channel radiances are simulated with LOWTRAN as described previously. Directional surface emissivities for snow are modeled (*Dozier and Warren*, 1982): the single scattering albedo and asymmetry factor in the scattering phase function are calculated from the Mie equations and the directional, wavelength-dependent emissivities are derived from the delta-Eddington approximation to the equation of radiative transfer. The directional emissivities are then integrated with the response function for each channel as described previously.

The use of the rawinsonde profiles in modeling the surface temperature requires an additional step since the first measurement in each profile is the shelter temperature, not the surface temperature. Therefore, the (unknown) surface temperature for each profile is assigned a series of values representing the range of possible surface temperatures for the observed conditions during the month to which the profile belongs. An energy balance model (*Maykut*, 1982) is used to determine these surface temperatures, based on the observed range of shelter temperatures and wind speeds (the mean ±1 standard deviation)

in the ice island data for each month.

The seasonal dependence of the coefficients is illustrated in Table II.4, where coefficients from each season were applied to data from every other season. Results are shown for NOAA 9 and indicate errors between 0.1 K for transition coefficients with winter data and 0.6 K when summer coefficients are used with winter data. Similarly, the satellite dependence of the coefficients is shown in Table II.5 for summer conditions. On the average, errors ranging from 0.1 to 1.0 K, depending on season, can be expected when applying coefficients derived for one satellite to data from another, the smallest errors occurring between NOAA 7 and 9 coefficients and data. Using SST coefficients developed for the North Atlantic and the Greenland Sea area to estimate IST would result in an underestimate of up to 0.7 K, largest in winter and at scan angles of 40° and greater. While the sensor scan angle is included explicitly in the correction equation, its effect in the dry arctic atmosphere is small, generally less than 0.1 K.

Surface temperature measurements taken by a PRT-5 thermal radiometer during CEAREX in March 1989 were compared to estimated ISTs from NOAA 11 AVHRR data. The mean IST for a sample of four AVHRR pixels was 258.9 K while the mean PRT-5 temperature (adjusted for an emissivity of 0.998) of four consecutive measurements one kilometer apart was 259.04 K. Given the difficulties in comparing the two data sets these results are encouraging.

In summary, using the split window channels and scan angle, the rms error in the estimated ice surface temperature is less than 0.1 K in all seasons. Inclusion of channel 3 (3.7 µm) during the winter decreases the rms error by less than 0.003 K. Overall, employing the IST coefficients results in increased accuracy of up to 0.6 K over SST coefficients developed for the North Atlantic and the Greenland Sea areas.

Additional details are provided in *Key and Haefliger* (1992).

Table II.4. RMS error in applying coefficients (NOAA 9) developed for one season (left) to data from another (top).

| Coefficients: | Data from: | | |
	Winter	Summer	Transition
Winter	0	0.403	0.128
Summer	0.587	0	0.342
Transition	0.117	0.219	0

Table II.5. RMS error applying coefficients (summer) developed for one satellite (left) to data from another (top).

| Coefficients: | Data from: | | |
	NOAA 7	NOAA 9	NOAA 11
NOAA 7	0	0.272	0.655
NOAA 9	0.296	0	1.017
NOAA 11	0.682	0.96!	0

PART III: ANALYSIS OF LEADEX AND OTHER *IN SITU* DATA

In this section we discuss data collected during LEADEX and its application to some of the procedures and models described in the previous sections. These applications are not exhaustive, but do provide some insight into problems that remain in the satellite remote sensing of leads.

III.1 ARCTIC AEROSOLS

The June 1991 eruptions of Mount Pinatubo ejected massive amounts of debris and sulfur dioxide gas into the stratosphere. Increased concentrations of aerosols in the stratosphere can perturb the radiative balance of the entire earth/atmosphere system (e.g., *Minnis et al.*, 1993; *Hansen et al.*, 1992; *Dutton and Christy*, 1992). This "volcanic forcing" is characterized by tropospheric cooling caused by an increase in the planetary albedo and by stratospheric warming primarily due to infrared absorption by aerosol particles. After reach ง a peak, the stratosphere's opacity normally decays exponentially in time at a rate dependent on the magnitude, time of year and location of the eruption (e.g., *Gerber and Deepak*, 1984; *Hofmann and Rose::*, 1987). Although the net radiative effect of atmospheric aerosols depends on many factors, the optical thickness and effective size distribution of the aerosols are most important (*Lacis et al.*, 1992). Aerosol optical thickness is a nondimensional parameter used to quantify the spectral extinction of direct solar irradiance by aerosols integrated along a path between an observer and the sun. If measurements of extinction can be obtained over a suitable range of wavelengths, then an effective size distribution of an aerosol layer can he inferred (*King et al.*, 1978).

During the spring of 1992 an extensive series of *in situ* measurements were made using airborne techniques as part of the Fourth Arctic Gas and Aerosol Sampling Program (AGASP-IV) in conjunction with the Arctic Leads Experiment (LEADEX). Nearly 1300 spectral measurements of solar irradiance were made from near the surface into the stratosphere using handheld sunphotometers during seven flights of the NOAA WP-3D aircraft. We focus here on an analysis of the stratospheric data to quantify the spectral opacity and infer effective size distributions for the Pinatubo aerosols present in the Arctic. Ancillary surface measurements are presented in support of the aircraft data analysis and are further used to estimate a decay rate of stratospheric optical depth following the period of peak aerosol concentration.

While the radiative transfer modeling results presented in previous sections indicates that aerosols play a relatively small role in the remote sensing of leads using thermal data, the results presented in this section are important because

1. the aerosol amounts measured are twice the value typical of the Arctic so that their impact on leads remote sensing in the thermal portion of the spectrum cannot be ignored, and
2. multiple scattering of shortwave radiation by aerosols is significant, especially at the levels measured.

While we have not emphasized remote sensing with shortwave sensor channels, they provide a potentially valuable source of information and should be the focus of future research.

III.1.1 MEASUREMENTS

The data are derived from two types of radiometric observations: (1) airborne and surface-based measurements made using sunphotometers, and (2) direct beam, wideband solar irradiance measurements made at a ground station. The primary data are derived from spectral measurements made during flight segments flown above the tropopause. Additional sunphotometer measurements were made at the surface near Resolute, N.W.T., as part of the 1992 and 1993 Seasonal Sea Ice Monitoring and Modeling Site (SIMMS) field programs (*Reddan et al.*, 1992), and in the vicinity of Anchorage, Alaska. The sunphotometer observations were made using two handheld, dual-channel instruments that sense directly transmitted solar irradiance at 380 and 500 nm, and at 778 and 862 nm, respectively; each channel having a nominal half-bandwidth of 5 nm and a field of view of 2.4°. The wideband (350-695 nm) pyrheliometer data were collected at the NOAA Climate Monitoring and Diagnostics Laboratory's Barrow Observatory (CMDL/BRW). The "wideband method" used to estimate optical depth was described by *Dutton and Christy* (1992). Only data collected during cloud-free periods are analyzed. The locations and dates corresponding to the various measurement periods are shown in Figure III.1. The curved vectors are back-trajectories representing stratospheric winds prior to each flight.
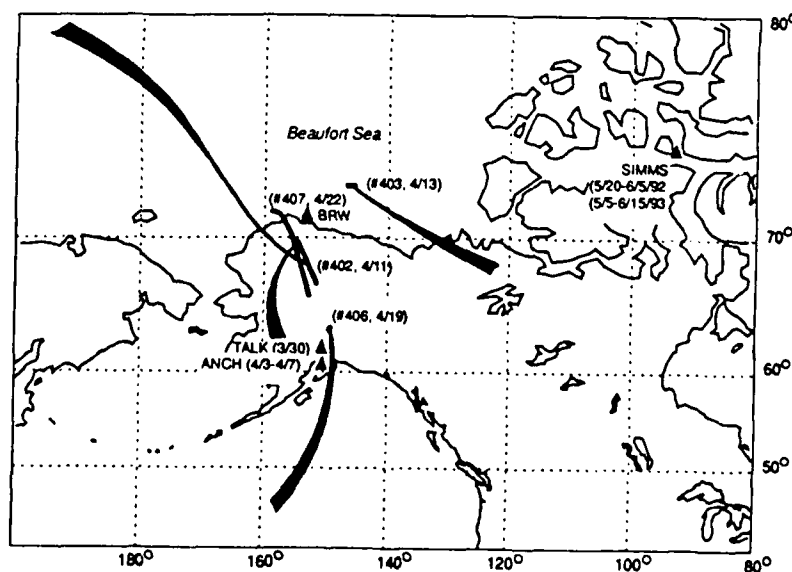

Fig. III.1. Distribution of sunphotometer measurements made during AGASP-IV/LEADEX stratospheric flight segments and at surface locations (ANCH, TALK, and SIMMS). Wideband pyrheliometric measurements were made at the Barrow Observatory (BRW). Curved vectors represent stratospheric winds for 36 hours prior to each flight (back-trajectories).

Airborne observations were made through optical glass windows whenever viewing was possible within ±30° of the solar azimuth relative to a plane perpendicular to the aircraft heading (e.g., *Dutton et al.*, 1989). The sunphotometers were carefully calibrated at high-altitude sites before and after AGASP-IV and again prior to SIMMS'93 in accordance with recommended procedures using the Langley plot method (*Shaw*, 1983). Each instrument was determined to be stable with precision of about 0.002 optical depth units (ODUs). All optical depth values reported in this paper account for Rayleigh scattering, ozone absorption at 500 nm, and changes in relative airmass as a function of time and location. Attenuation by the optical glass was also accounted for when reducing the aircraft data. Thus, from total slant-path irradiance measurements, columnar aerosol optical depths were computed. Estimated uncertainties due to all sources of error are no more than 0.02 ODUs (*Reddy et al.*, 1990), or less than 10% of typical values reported here. The wideband measurements are accurate to within ±0.04 ODUs (*Dutton and Christy*, 1992).

III.1.2 RESULTS

III.1.2.1 *Stratospheric Aerosol Optical Depths*

Only direct measurements made above the tropopause and the clear-sky, ground-based measurements were selected for analysis. Tropopause heights for each flight were determined on the basis of the analyses of *Herbert et al.* (1993); these range from about 7 km to 10 km, depending on geographical location and synoptic conditions. Stratospheric components were estimated from the surface measurements of total-column optical depth by subtracting predetermined "background" values for the troposphere, a method also used by *Asano et al.* (1993). For our purposes the March 1979-1982 monthly mean background values of spectral aerosol optical depth estimated for BRW (*Dutton et al.*, 1984) were systematically subtracted from the respective measured values. Note, however, that March background values are typically smaller than those for April and larger than those for May or June based on recent wideband analyses (Dutton, unpublished data). Figure III.2 shows the mean stratospheric aerosol optical depths, plus and minus one standard deviation (±1σ), derived from observations made at the corresponding times and locations shown in Figure III.1. The tropospheric background values used to correct the surface measurements are also shown with ranges of uncertainty indicated.

Several features of Figure III.2 are notable. First and most important, the values derived for all times and locations are 1 to 2 orders of magnitude greater than stratospheric background levels (*Toon and Pollack*, 1976); these values also exceed similar measurements made in the Arctic approximately a year after El Chichon erupted (*Spinhirne and King*, 1985; *Dutton et al.*, 1984). Second, optical depths derived from the aircraft observations tend to be rather flat spectrally in the visible range compared with the 1992 surface results. Third, three of the flights, 403, 406 and 407, indicate a high degree of homogeneity in time and space, as evidenced by their small standard deviations, similar magnitudes, and spectral dependencies. Fourth, the values for flight 402 are about 60% lower than those measured during flight 407 despite their having similar flight tracks and altitudes relative to the tropopause. Fifth, the curve for SIMMS'92 also falls below all of the AGASP curves except for that of flight 402, suggesting that either temporal and/or spatial variations occurred over the period and geographical region represented by these data, or that the SIMMS data are negatively biased due to incorrect assumptions made regarding the tropospheric background corrections. And last, the values for SIMMS'93 are significantly lower and have a different spectral signature than those for SIMMS'92, indicating a decay in opacity from one year to the next as well as a change in microphysical characteristics.
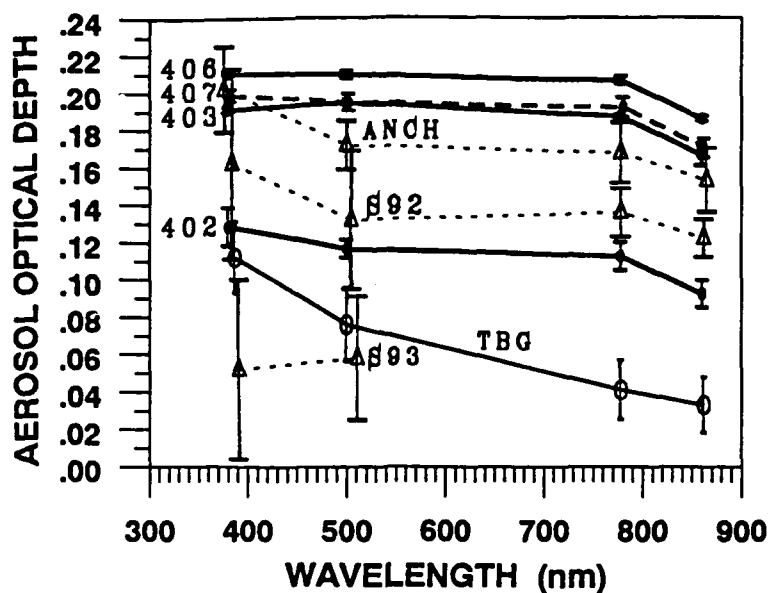
Fig. III.2. Mean stratospheric spectral aerosol optical depths derived for the flight segments and surface locations shown in Figure III.1. Slight spectral offsets are used to clearly indicate values at plus and minus one standard deviation (vertical bars). S92 and S93 are averages of the SIMM'92 and SIMMS'93 data, respectively (only 380 and 500 nm measurements were made in 1993); ANCH is the average of the Anchorage (ANCH) and Talkeetna (TALK) data. The TBG curve (adapted from Dutton et al. (1984)) gives the values and estimated ranges of the tropospheric background corrections used to derive stratospheric optical depths from the surface-based measurements.

III.1.2.2 *Inferred Aerosol Size Distributions*

Based on the data presented in Figure III.2, effective aerosol size distributions were inferred using the constrained linear inversion algorithm of *King et al.* (1978). The radius sensitivity $(r_{min} \leq r \leq r_{max})$ (*Spinhirne and King*, 1985) determined for our particular set of measurements was within the range $r_{min}=0.10 \pm 0.02$ µm and $r_{max}=1.10 \pm 0.10$ µm. We assumed an index of refraction of 1.45-0.0*i* based on earlier *in situ* observations of the Pinatubo aerosol layers (*Deshler et al.*, 1992). The inversion results are presented in Figure III.3. Each curve shows the total number concentration dN (cm^{-2}) for seven radius increments $[dlog(r)]$. The vertical bars indicate the range of number density determined by inverting the mean spectral optical depth data $\pm 1\sigma$. We find that, for the period and geographical region of interest, the inferred size spectra tend to fall into two groups. Both are bimodal, having a large-particle mode centered at about 0.50 µm radius and a small-particle mode of higher concentration peaking below about 0.18 µm. These results suggest that the volcanic aerosols present in the Arctic about 10 months after

Pinatubo erupted were slightly larger than the newly formed particles observed over Laramie, Wyoming several weeks after the eruption (*Deshler et al.*, 1992) but were smaller than those estimated by *Asano et al.* (1993) in Japan approximately 2 months before the Arctic observations were made. Their independent determinations of size spectra also show the bimodal feature noted here attributed to the superposition of a monodisperse large-particle (volcanic) mode onto a small-particle (background) mode. Similar bimodal size spectra were inferred using photometric measurements made at high northern latitudes about a year after El Chichon erupted (*Spinhirne and King*, 1985).
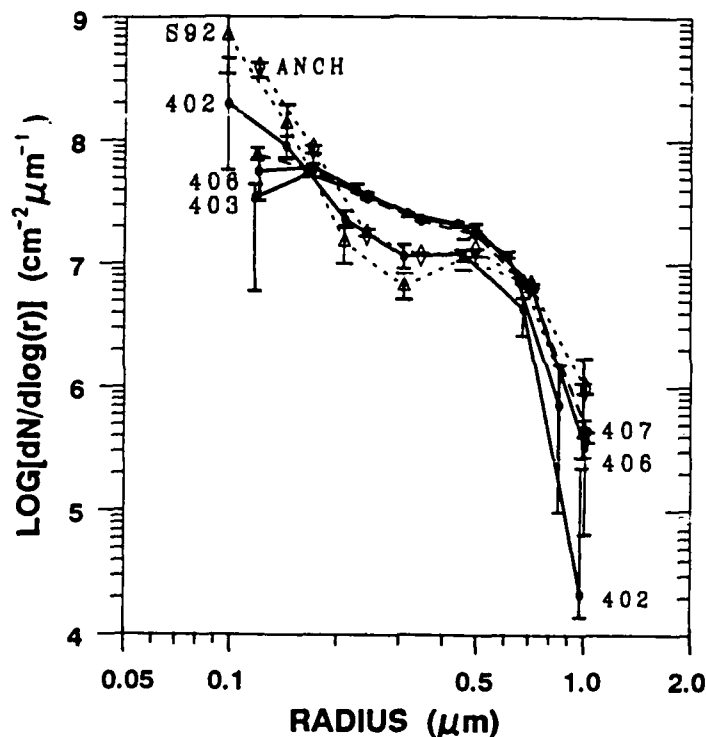
Fig. III.3. Effective aerosol size distributions showing the range of number concentrations *dN* (cm⁻²) at each radius interval [*dlog(r)*] inferred from the optical depth data shown in Figure III.2.

III.1.2.3 *Time Decay of Stratospheric Opacity*

To evaluate the decay of the Pinatubo aerosol layer(s), we analyzed the BRW optical depth data and the spectrally-weighted average of the 380 and 500 nm SIMMS observations for the successive 1992 and 1993 spring periods. At BRW the optical depth reached an average peak value of about 0.19 during early May 1992 and declined thereafter (updated from *Dutton and Christy* (1992)). Assuming that optical

depth τ decays exponentially in time t after reaching its peak value τ_{peak}, i.e., $\tau(t) = \tau_{peak}\exp(-t/T)$, a fit to the BRW data yields a time constant T of 13.3 months. A corresponding fit to the SIMMS data yields a time constant of 13.7 months, assuming that the peak opacity also occurred during May 1992 and that the BRW seasonal background tropospheric corrections were valid for the SIMMS site. We give credence to these estimates because independent measurements from geographically distinct sites were used to obtain very similar results noting, however, that the actual overall decay of volcanic aerosols may not be well represented by a smooth exponential function (*Hofmann and Deshler*, 1987). At least another year of monitoring is needed before our results can be corroborated. Our preliminary analysis suggests that the Pinatubo aerosols are being systematically removed from the Arctic stratosphere, but at a slower rate than estimated following earlier volcanic eruptions. On the basis of *in situ* midlatitude measurements of aerosol size distributions, *Hofmann and Deshler* (1987) estimated the decay rate (e-folding time) of total stratospheric mass after the El Chichon eruption to be about 10.3 months and between 8 and 10 months following the 1974 eruption of Fuego in Guatemala. High-latitude satellite observations of 1.0 µm stratospheric aerosol optical depth (*McCormick and Trepte*, 1987) also exhibited faster decay rates following the 1980 Mt. St. Helens and the El Chichon post-volcanic periods than we report here.

III.1.3 DISCUSSION

It appears from Figure III.2 that temporal and/or spatial variations in stratospheric aerosols occurred in the Arctic during spring 1992. The lower relative opacity noted for flight 402 can be explained by differences in synoptic conditions during the respective flight periods (*Herbert et al.*, 1993). During flight 402 strong northerly winds transported polar air into the region whereas for the later three flights moderately weak southerly flow was generally observed. An analysis of isentropic back-trajectories (e.g., *Harris and Bodhaine*, 1983) based on the ECMWF 2.5° gridded data supports the synoptic analyses. Figure III.1 shows 36 hour back-trajectories representing the flow at altitudes ranging from about 14.5 to 15.8 km referenced to the respective midflight segments. This analysis suggests that relatively clean Arctic air displaced or mixed with lower latitude air, effectively reducing the stratosphere's opacity prior to flight 402. The formation of the polar vortex during the previous autumn/winter probably prevented high concentrations of Pinatubo aerosols from penetrating the central Arctic. Similar gradients related to the position, size, and shape of the polar vortex were observed several months after El Chichon erupted (*McCormick et al.*, 1983).

The relatively large 380 nm optical depths measured during flight 402 and at all the surface locations during spring 1992 (Figure III.2) indicate fundamental differences in the aerosols' microphysical properties compared with the results of other flights or the SIMMS'93 data which show less variation over the visible wavelengths. The apparent increase in attenuation at 380 nm is most likely due to the presence of higher concentrations of small particles (Figure III.3) that have greater extinction efficiencies as the ratio of size-to-wavelength (r/λ) increases (*van de Hulst*, 1981). Because such enhancements are most pronounced in the results derived from highly variable surface measurements we suspect that tropospheric haze, not visible against the "milky" appearing stratosphere, may have contaminated these particular results. The sharp decreases evident at the large-particle end of the inferred size spectra are attributed to the observed decreases in opacity for $\lambda > 778$ nm.

Finally, we speculate that the apparent longevity of the relatively large Pinatubo aerosols in the Arctic may be due to the vaporization and regrowth processes discussed by *Hofmann and Rosen* (1987), possibly augmented by general circulation patterns that favor the heating of the Arctic stratosphere during winter (*Robock and Mao*, 1992) and the accumulation of aerosols at high latitudes.

III.2 LEAD CHARACTERISTICS FROM CO-LOCATED
AVHRR, DMSP OLS, LANDSAT TM, AND ERS-1 SAR

In Section I we describe theory and observations outlining the effects of spatial resolution on lead statistics. Here we apply and extend those results to additional data sets. To compare whether substantial differences might exist in lead statistics derived from different image types, we have assembled a data set consisting of AVHRR direct-readout imagery, Defense Meteorological Satellite Program (DMSP) Operational Line-scan System (OLS) data, Landsat Thematic Mapper (TM) images, and ERS-1 synthetic aperture radar (SAR) data for 15 April, 16 April, and 18 April 1992. The TM and SAR imagery were co-registered as part of a separate NASA-funded effort. The AVHRR imagery were obtained from Ron Lindsay (Univ. of Washington), with additional AVHRR and OLS provided by Florence Fetterer of NRL. Pixel sizes for the georeferenced data were 1 km (AVHRR), 0.5 km (OLS), and 25 m (SAR and TM). For comparison, the AVHRR and OLS sections corresponding the the SAR and TM coverages were subsectioned out, and the SAR and TM resampled to 1 km pixels. For a variety of reasons, not all data sets were co-registered with each other. The matching data sets are OLS and AVHRR thermal channels for 15 April; AVHRR (all channels) and TM (all channels for 16 April; SAR (15 April) coregistered with the 16 April AVHRR and TM; and all AVHRR and TM channels for 18 April. The image sets for 15 and 16 April are discussed here.

The lead-statistics program (hereafter "LEADSTATS") described in Section I.3.1 was used to calculate leads data from each image section. The images were first converted to binary "lead/not-lead" images using an interactive thresholding procedure. Thresholds were set to capture as many apparent leads as possible (open water and thin-ice leads) in each image. While this procedure is subjective, it allowed us to maximize the information content in each image. The resulting binary images were then processed.

III.2.1 AVHRR AND OLS: EFFECTS OF SPATIAL AND RADIOMETRIC RESOLUTION

Figures III.4a and III.4b show co-located OLS and AVHRR thermal-band imagery, with a portion of each image resampled (nearest-neighbor sampling) to equivalent pixel sizes of 250 m (Figure III.5a and III.5b). In this example, the greater radiometric resolution of AVHRR tends to outweigh the effects of lower spatial resolution; the AVHRR data capture the same lead patterns as visible in the OLS, as well as showing additional lower-contrast leads (either refrozen or narrow open-water leads) that are not resolved in the OLS image. However, the effect of the lower spatial resolution of AVHRR vs. OLS is shown in the apparent lead widths in the two images, where the AVHRR data suggests wider leads than is indicated in the OLS. Both the radiometric and spatial resolution effects are depicted in a transect through the two images (Figure III.6). In this example, most of the leads are 2 digital numbers (DN) or less of the ice background DN value in the OLS data. The tendency for AVHRR to overestimate lead width relative to OLS is apparent at locations 150 and 725 along the transect. This difference obviously depends on the threshold selected to define leads. In Figure III.7, for example, selecting a threshold for each image type to capture only the warmest pixels yields quite similar results. Along this transect, the thresholds used in Figure III.7 results in 8.0% of the transect mapped as leads in the AVHRR data, and 7.0% in the OLS data When the same thresholds are applied to the full image subsets in Figure III.4, the difference in lead area is greater (total lead area of 18.2% in the OLS and 28.5% in the AVHRR), indicating the difficulty of selecting a single threshold to yield uniform results across even a relatively small portion of images.

The detail in the AVHRR data due to the greater radiometric resolution compared to OLS has a large effect on the ability of the LEADSTATS routine to define leads with high confidence. For example, when cloud cover is excluded from the images shown in Figure III.4, and thresholds manually selected

to highlight leads, LEADSTATS identifies only a single clearly-defined lead and 3 ill-determined leads. In the AVHRR image, 87 leads are clearly defined, with another 130 ill-determined leads. While this difference might be reduced by trying a variety of thresholds, it points out that mapping of lead area using spatial patterns and context is even more sensitive to radiometric information than is lead-area mapping using thresholds only.

III.2.2 LANDSAT THEMATIC MAPPER, AVHRR, AND SAR: EFFECTS OF RESAMPLING, WAVELENGTH, AND SCALE

As noted above, a set of Landsat TM, AVHRR, and SAR data were assembled to allow lead features to be intercompared at different spectral wavelengths and spatial sampling (Figure III.8). Obvious features of this set are the close correspondence between the AVHRR and Landsat TM Ch. 2 image (originally 30 m field-of-view resampled to 1 km pixel size) and the utility of the Landsat thermal channel (Ch. 6; originally 200 m field-of-view) to discriminate open water from refrozen leads. Also apparent are large differences between the SAR image and the TM and AVHRR data. The SAR image was acquired one day earlier, but the lack of direct correspondence to the TM and AVHRR imagery is typical of data compared elsewhere. Figure III.9 highlights the differences between the SAR and TM Ch. 2. These differences are apparently due to a large range in surface backscatter that is not necessarily related to ice thickness, whereas the albedo and temperature information in the TM and AVHRR data appear to be more directly related to open-water and refrozen leads. The intermediate backscatter of areas indicated as open water in the TM and AVHRR suggests that the open-water areas are being roughened by wind, and thus not spectrally distinguishable from thin ice. Differences between ERS-1 SAR and optical and thermal-wavelength data are discussed in further detail in the following section on the evolution of lead patterns in response to atmospheric circulation. A comparison of Landsat thermal channel 6 and AVHRR thermal channel 4 (Figure III.10) points out the effects of the higher radiometric resolution of AVHRR, which shows more lead detail in spite of AVHRR's lower spatial resolution. The effects of this lower spatial resolution on apparent lead width is also demonstrated in this figure.

While the TM and AVHRR data are qualitatively similar when mapped to equivalent pixel sizes, comparisons of statistics of lead-covered area can vary considerably depending on the threshold used to define lead area in the AVHRR data. Selecting a threshold that delineates most of the leads in the AVHRR data yields substantial overestimates of lead area compared to lead area mapped from TM data gridded to a 50 m pixel size. For example, selecting thresholds in this manner for AVHRR Ch. 2 and Ch. 4 yields lead areas of 4.7% and 3.0%, compared to 0.8% in the 50 m TM Ch. 2 data. To explore this issue of how lead statistics intercompare across different fields-of-view, we apply a method discussed in *Key et al.* (1993b) and in Section I.3.5.2 of this report. In this approach, it was noted that lead area mapped using a single threshold tends to decrease roughly linearly with pixel size. This decrease is due to the progressive loss of radiometric contrast of lead pixels with surrounding ice pixels as spatial resolution decreases. Thus, by calculating lead area L at resolution K, and K', where K' is a resolution degraded following some spatial interpolation method, then the resulting slope can be used to estimate L at some finer spatial resolution.

To test this approach as a means of intercomparing lead area estimated at difference pixel sizes, we degraded the 1 km AVHRR for 16 April to pixel sizes of 2, 3, and 4 km using bilinear interpolation. The TM data were also degraded to 50, 100, 200, 500, and 1000 m pixels. In keeping with the assumption of loss of lead area with decreasing resolution, a threshold should be selected such that only the darkest (in optical wavelengths) or warmest lead pixels are flagged as lead area. The alternate approach of selecting a threshold to maximize the apparent lead coverage produces an overestimate of lead area. Given that radiometric contrast decreases as leads no longer fill a single pixel, attempting to select

an intermediate threshold value then places entire pixels into a lead-area class, when in fact only a portion of that pixel (or perhaps none of the pixel, depending on the spatial interpolation used) actually consists of lead area. Thus, when as above, we select a threshold in the AVHRR data to highlight the lead patterns, the result was about 5 times more lead area than actually exists, based on the Landsat TM data. While this effect of threshold selection may be intuitively obvious, the tendency nontheless is present to select thresholds that give the most visually pleasing maps of lead networks. However, selecting a threshold by the "minimum rule" given above is not only more realistic of the true situation, but also lends itself to automated processing, where the image can be scanned for minimum reflectances or maximum temperatures to provide the appropriate thresholds.

Thresholds selected in this manner produced the following lead-area proportions in the full-resolution and degraded AVHRR and Landsat data. In the case of the Landsat data, a threshold was first selected using the 50 m image, and then applied to the degraded data, e.g., as a test of what happens when the true reflectence of an open lead is known.

Table III.1. Lead area as a proportion of total ice area, estimated using a "minimum-rule" threshold from AVHRR imagery degraded from 1 km to 4 km pixel sizes using bilinear interpolation.

Channel	1 km	2 km	3 km	4 km
Ch. 2	0.63%	0.31%	0%	0%
Ch. 4	0.28%	0.19%	0.14%	0%

Table III.2. Lead area as a proportion of total ice area, estimated using a "minimum-rule" threshold from Landsat TM imagery degraded from 50 m to 1 km pixel sizes using bilinear interpolation.

Channel	50 m	100 m	200 m	500 m	1 km
Landsat TM 2	0.78%	0.72%	0.63%	0.44%	0.23%

The change in lead area with pixel size is essentially linear in the AVHRR data. From the slopes of these lines, we can estimate the lead area at a pixel size of 50 m, which we can take to represent the true areal coverage of leads. Applying this to the AVHRR Ch. 2 and Ch. 4 data yields estimated lead area at 50 m pixel sizes of 0.93% for Ch. 2 and 0.37% for Ch. 4. The combination of the minimum-rule threshold selection and this adjustment for pixel size takes the lead area proportion in the correct direction, although with the small lead fractions in these data, the effect of the change is fairly small. Using the Landsat data as, for example, a MODIS-type product where one wished to estimate lead area from 500 m data, and was able to use a subset of a higher-resolution MODIS channel or coincident Landsat data to define a "true" lead reflectance threshold, then by degrading the 500 m data to 1 km, the resulting slope results in an estimated lead area of 0.63% for a 50 m pixel size. This is clearly an improvement over simply using the lead-area estimate from the 500 m data alone. If nothing else, this approach helps to avoid overestimating lead area from low-resolution data, while offering an adjustment that compensates at least partly for the loss of contrast with interpolation.

The detail present in the full-resolution TM data (not shown) make the TM imagery particularly well-suited to test the effects on lead statistics of spatial resampling. Using LEADSTATS, 177 well-defined leads (representing 1.7% of the total area) were identified in the full-resolution TM image, 43 leads (also 1.7% of the image area) at 100 m pixel size resampled using nearest-neighbor sampling, and 48 leads (1.5% of the area) at 100 m resampled using bilinear interpolation. The difference between the sampling methods is typical of the loss of spatial pattern but retention of radiometric integrity offered by nearest-neighbor sampling, whereas bilinear interpolation tends to retain the linearity of leads but due to interpolation, a portion of lead pixels are lost due to radiometric averaging with surrounding ice pixels. This trade-off between retaining spatial patterns and preserving the spectral signatures will depend on lead width, since the detectability of narrow leads will be more affected by spatial interpolation than will large leads. The effects of interpolation are also dependent on the contrast between leads and the surrounding ice cover.

To investigate the effects of AVHRR spectral channel on lead retrieval, lead statistics were calculated from AVHRR channels 1-4 at 1 km pixel size, and from the SAR image resampled to 1 km pixels (e.g., the image sets in Figure III.8). More lead segments are defined using AVHRR Ch. 1 (39 leads) than Ch. 2 (29 leads) perhaps due to the slightly greater contrast between open water/thin ice and snowcover in Ch. 2. The total lead area is about the same (approximately 4% of the image area). With the AVHRR thermal channel 4, 15 leads are found (about 1% of the area). The difference between the lead-area estimates at the optical and thermal wavelengths appears to be a reasonable estimate of the differences between the proportions of open water and thin ice within the pack. In the SAR image, the total number of lead fragments identified (15) and total lead area (1%) were similar to the AVHRR data, although the actual areas classified as lead bore little resemblance to leads mapped in the AVHRR data.

III.2.3 EVOLUTION OF LEAD PATTERNS IN AVHRR AND ERS-1 SAR DATA

Spaceborne SAR is the only sensor that can produce sequential coverage of the ice pack under all weather conditions at spatial resolutions suitable to detect individual leads. In principal then, SAR data should be well-suited for observing the evolution of leads under different wind and ice-motion regimes. However, as demonstrated above, substantial uncertainties exist in how leads actually appear in terms of backscatter properties, compared to lead patterns apparent in optical and thermal-wavelength imagery. To investigate whether the analysis of a sequence of SAR images rather than a single scene can aid in interpreting lead patterns, a time series of SAR data has been interpreted for locations in the Beaufort Sea during periods of strong synoptic activity during 15-31 October 1991, and for an annual cycle from October 1991 through October 1992 (Maslanik et al., 1993; Heinrichs et al., 1993). Results from the October case study is discussed below. This work was also supported by NASA funds, where the SAR-derived lead fractions and ice concentrations were compared to SSM/I, AVHRR, and ice model output. Here, we focus on the leads-mapping issue.

For the 15-31 October case study, three sets of SAR imagery resampled to 100 m pixels were acquired for three locations in the central Beaufort Sea. Three to four overlapping images were selected for each site. As in the examples cited above, a backscatter threshold was selected for each image to discriminate as well possible open water/thin ice from first-year and old ice in the uncalibrated SAR images. Statistics on numbers of leads, lead width, and orientation were derived for each image using the LEADSTATS program. Visual interpretation of the SAR time series sets provides the best indication of how lead patterns evolve under the different wind regimes in the October case. Ice motion is slow enough to allow observation of the same features in the ice pack over most of the sampling period. At all three sites, no leads are visible in imagery acquired on 17 October, prior to the passages of deep low-pressure systems on 21-23 October. As the lows move through the region, leads develop in the

central Beaufort oriented in nearly the same direction as the geostrophic winds. By 26 October, the lead orientations have changed to primarily north-south in the northern and central Beaufort sites, with no leads visible at the southern site. The same pattern is present on 29 October at each site.

Using the LEADSTATS routine, the maximum amount of any of the SAR images classified definitely as lead area did not exceed 0.7%. When all pixels with backscatter values below the classification threshold were included, the estimate of open water/thin ice area is still small for all the SAR images studied for the October case, with little evidence of a large-scale opening of the pack due to passage of the strong synoptic systems. Either little change in open-water fraction occurs due to the variable winds, or the changing ice conditions are not apparent in the SAR data. The time span between images is long enough to allow refreezing. However, since some leads remain visible over 5 to 9 days, it is likely that some evidence of a substantial opening of leads would be apparent. It is also possible that openings occur that are sufficiently small to be undetected at the SAR pixel size (100 m in the Lo-Res imagery used here). Analyses using full-resolution (25 m) ERS-1 SAR imagery for a different application (Steffen et al., 1993) did not suggest that the resampling to 100 m resulted in a significant change in open-water/thin ice fraction. However, this comparison needs to be repeated for the specific cases considered here.

Discrimination of leads in SAR data is complicated by the complex backscatter properties of open water and thin ice. As noted above, the main sources of uncertainty and lack of unique backscatter signature are the effects of wind speed (affecting open water areas), and variability in surface dielectric properties and surface roughness that can occur in thin ice forming in leads. Open-water areas can have very low backscatter under calm conditions with backscatter increasing as wind speed increases, such that open-water leads can be indistinguishable from surrounding ice, as is apparently the case in the comparison of Landsat TM, AVHRR, and SAR discussed earlier. If wind speeds are high enough, and perhaps depending on wind direction and lead orientation, open-water areas can be the highest-backscatter features in SAR images (Steffen, et al., 1993).

AVHRR data for the October case study provide a qualitative look at sea ice conditions, although cloudiness is too extensive to permit digital classification of ice concentration from AVHRR during much of the period. In general, as was the case with the comparison with TM and SAR, the AVHRR data suggest greater amounts of leads than the SAR data indicate. Given the relationships of SAR backscatter to a number of factors such as wind speed, surface brine expulsion, and frost-flower formation, it is quite possible that leads apparent in AVHRR thermal-channel data will not be visible in the SAR. For example, Figure III.11 shows co-registered AVHRR and SAR coverages for 29 October. While the large leads in the SAR are also visible in the AVHRR thermal-band data, other leads apparent in the AVHRR image do not appear in the SAR. The physical temperatures of the leads in this AVHRR image average about 5 K warmer than the surrounding ice (245 K vs. 240 K), indicating that the leads either consist of young ice (rather than open water), or are narrower open-water leads that, through resampling and interpolation, appear as wider, lower-temperature features. A threshold classification of this portion of the AVHRR image corresponding the the SAR scene yields about 7% of the area as open-water/thin ice ("warm" ice) 65% first-year ice (mid- temperature ice), and 28% old ice ("cool" ice).

Since the apparent lead temperature at the AVHRR field-of-view is a function of lead width, lead-surface temperature, and ice-surface temperature (e.g., the observed pixel temperature is a mixture of temperatures of the lead and ice surface), then knowledge of lead width reduces this system to a single unknown (lead-surface temperature) if we assume that accurate lead width can be estimated from SAR, and ice-surface temperature can be reasonably estimated from AVHRR data elsewhere in the image. Thus,

$$T_L = (T_B - T_I P_I)/P_L ,$$

where T_L is the lead-surface tempeature, T_B is the observed AVHRR pixel temperature, T_I is the thick-ice surface temperature. P_I is the proportion of thick ice in the pixel, and P_L is the proportion of lead in the pixel. For the image in Figure III.11, using the large lead in the center of the images, T_B = approximately 243 K, T_I = 240 K, and since lead width from the SAR is about 400 m and the AVHRR pixels are 2 km by 2 km, P_L = 400 m/2000 m and P_I = (2000 m - 400 m)/2000 m. From the above equation, T_L thus equals 255 K, suggesting that the lead is in fact refrozen. The single example given here could be refined by using full-resolution (12.5 m) SAR to get estimate lead width as accurately as possible, since if the lead is in fact 200 m wide, then T_L is near 270 K. Alternatively, if it is known that the lead is actually open water, such as if wind roughening yielded a very high backscatter clearly due to wavelets on the water surface, then this knowledge can be used to constrain the estimate of lead width. In the case given above, for example, the lead would be unlikely to be much smaller than 200 m, since T_L then becomes greater than the freezing temperature. A 100 m lead would require a T_L of about 300 K. Given this surface temperature, and also wind speed, radiation, conductivity, and ocean heat flux, a rough estimate could be made of the ice thickness within the lead. Another application of this pixel "unmixing" through combination of SAR and AVHRR might be to define a true reflectance or surface temperature for leads, which could then be used in the procedure discussed earlier to correct lead-area estmates for pixel size. This would be equivalent to the degraded-Landsat example, where the best threshold to use was known (since it was determined from the 50 m TM data). In this case, however, the threshold does not require a high-resolution image such as Landsat, and can make use of the wider availability of SAR data.

As one would expect from the operation of the leads-mapping routine, area classified as leads is substantially smaller than total open water/thin ice area defined by a simple threshold. In the case of the SAR data studied here, the "spatial coherence" criteria that the leads-mapping routine uses to define leads is particularly important, since manual interpretation of the SAR data shows that much of the area classified as open water/thin retain a consistently low backscatter over the full 15-day study period, which is unlikely given the expected refreezing of open water areas. The lead areas, however, evolve in a logical manner over time. These results indicate that, as suggested by other investigators, some of the uncertainty in SAR classification can be alleviated using pattern recognition tools in addition to simple backscatter thresholds.

III.2.4 SUMMARY

Comparisons of the different image types allows us to assess the effects of spatial resolution, radiometric resolution, resampling method, and temporal information on leads mapping. AVHRR and Landsat Thematic Mapper imagery (resampled to match the AVHRR pixel size) contain essentially the same information in terms of discimination of leads. The choice of resampling methods (bilinear interpolation or nearest-neighbor sampling) depends on whether retention of spatial patterns or radiometric information is most critical.

While SAR data clearly contain leads information, comparison to the other image types shows that the variable backscatter of thin ice and open water in the single-channel, single-polarization ERS-1 SAR substantially complicate the interpretation of leads, and can potentially cause large errors when automated leads mapping routines. Accurate discrimination of lead features in single- channel SAR data will likely require spatial operators. However, even when spatial features such as linearity and orientation are used, SAR classification is limited by a variety of factors that can render lead backscatter indistinguishable from the backscatter of the surrounding ice. It is likely that the best classifiers will consider both spatial and temporal patterns and changes in backscatter, as well as the actual backscatter values themselves.

For cases where the same leads are apparent in both SAR data and AVHRR, then it should be possible to estimate the lead surface temperature from the AVHRR thermal channels, given the "true" lead

width as estimated from the SAR data. An example is given for a matched set of AVHRR and SAR images. This combination could unambiguously define open-water leads from refrozen leads. Also, with additional information such as air temperature, winds, and oceanic heat flux, this surface temperature could be used to derive the ice thickness within refrozen leads. In practical terms, the accuracy of this approach is limited by differences in acquisition time between the SAR and AVHRR data and, to a much less extent, errors in retrievals of surface temperature from AVHRR. Other potentially valuable approaches exist that take advantage of combinations of data and ancillary information to, for example, estimate lead fraction when wind speeds are known (Heinrichs et al., 1993), or to calculate wind speeds when leads are known to be open water (Steffen et al., 1993).
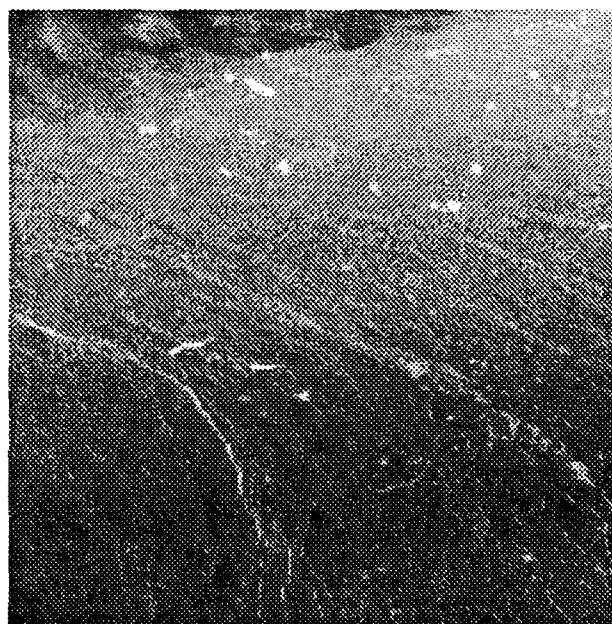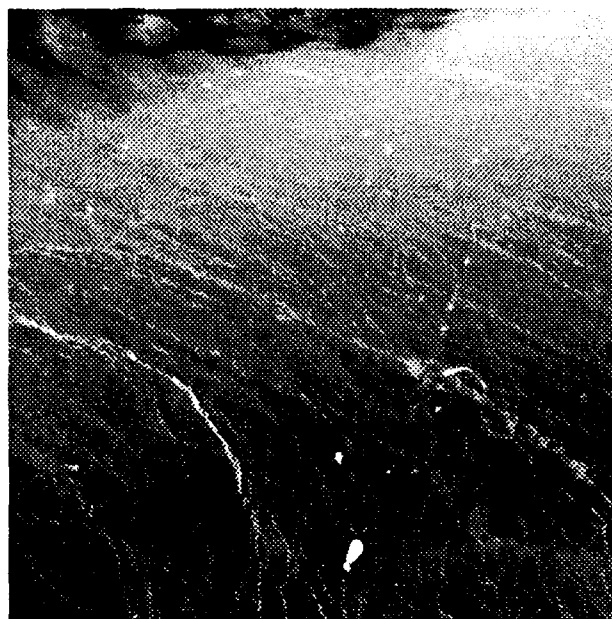
Fig. III.4. Co-located DMSP OLS (a, top) and AVHRR (b, bottom) thermal-wavelength imagery for the central Beaufort Sea on 15 April 1992. Pixel dimensions are 1 km for AVHRR and 250 m for OLS. Warmer areas appear brighter.
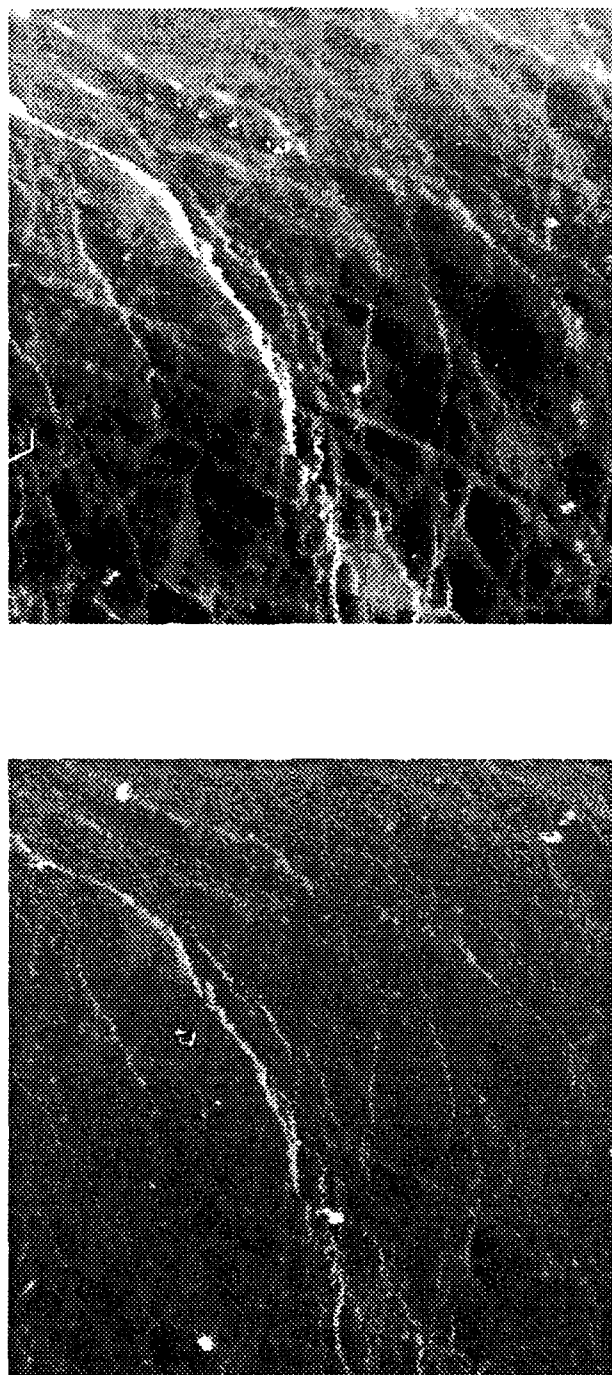
Fig. III.5. Enlarged portions of OLS (a, top) and AVHRR (b, bottom) for 15 April 1992, with both image types resampled to 250 m pixels. Location of the transect plotted in Figure III.6 is indicated on (b).
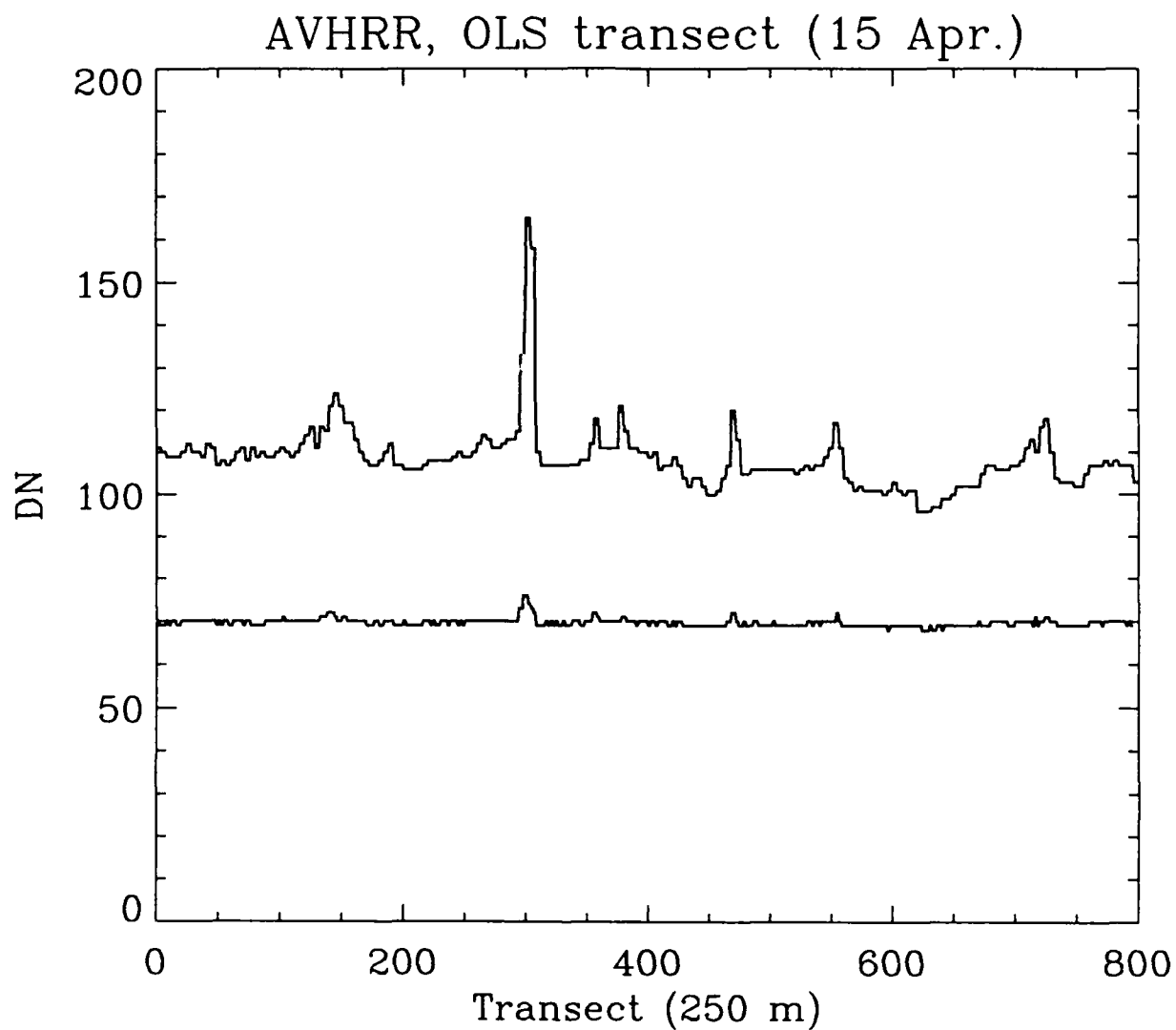
AVHRR, OLS transect (15 Apr.)

Fig. III.6.   Transect of AVHRR and OLS digital numbers along the transect shown in Fig. III.5.   The AVHRR transect is plotted above the OLS transect.   An offset of 50 was added to the OLS digital numbers for plotting purposes.

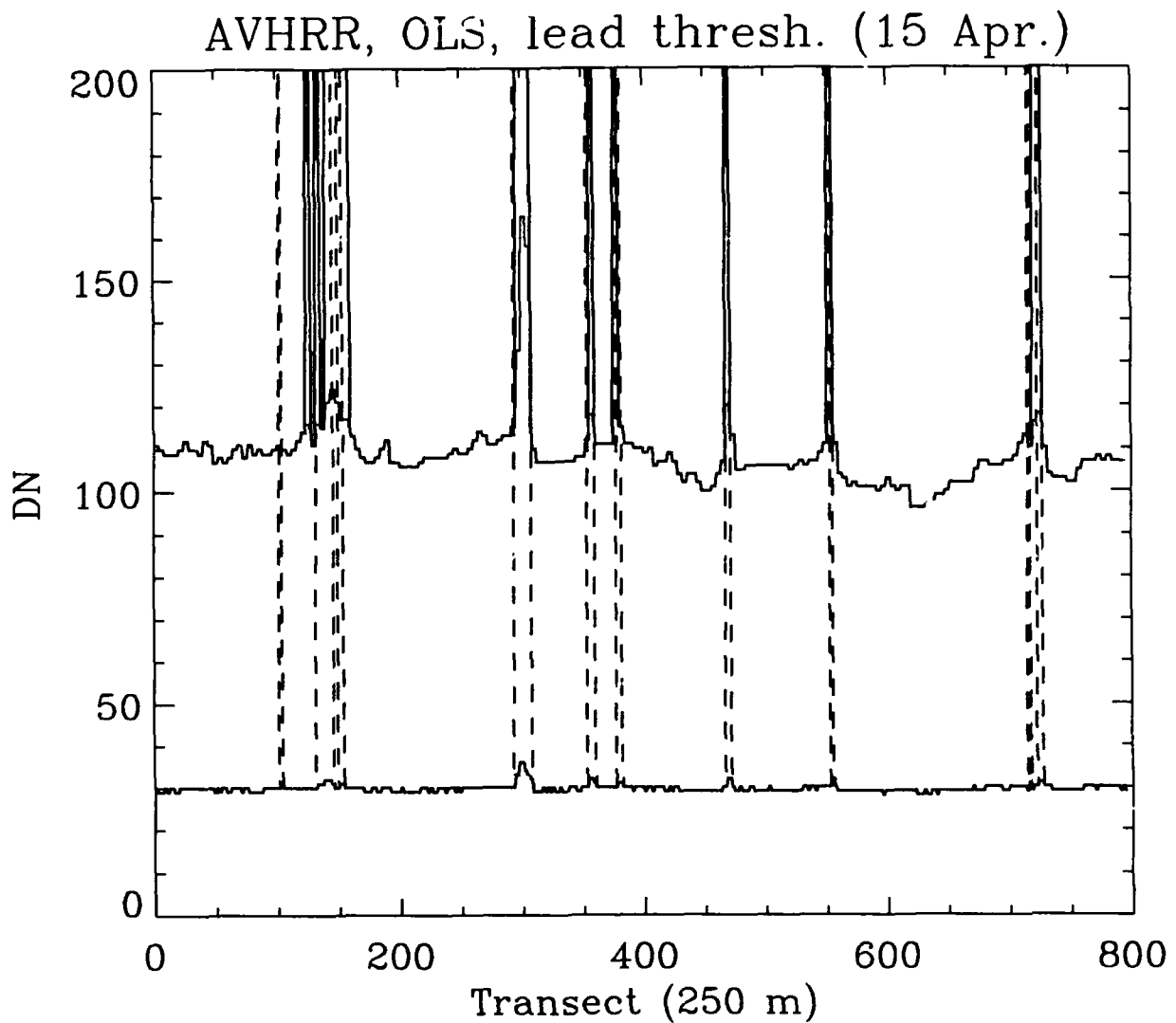## AVHRR, OLS, lead thresh. (15 Apr.)

Fig. III.7.   Comparison of portions of the transect mapped as leads using AVHRR and OLS digital-number thresholds. Digital numbers greater than the selected thresholds were mapped to a value of 200. Apparent are the limited radiometric range of the OLS data, effect of threshold on estimated lead width, and the good spatial registration between the two images.
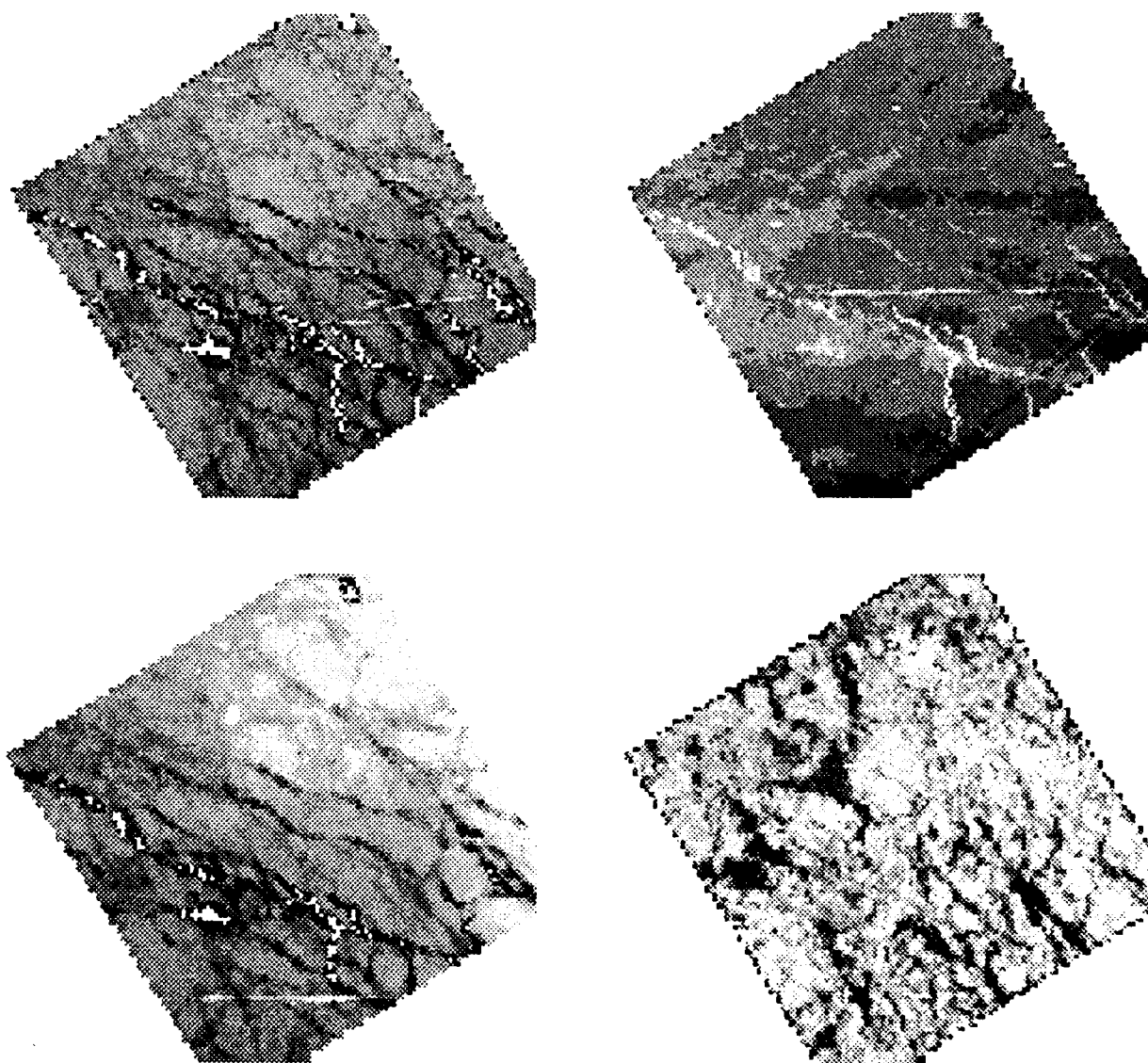
Fig. III.8. Co-registered Landsat TM Channel 2 for the central Beaufort Sea (top left), TM thermal channel 6 (top right), AVHRR Channel 1 (bottom left), and ERS-1 SAR (bottom right), each gridded to 1 km pixel size. TM and AVHRR were acquired on 16 April 1992. SAR data were acquired on 15 April 1992.
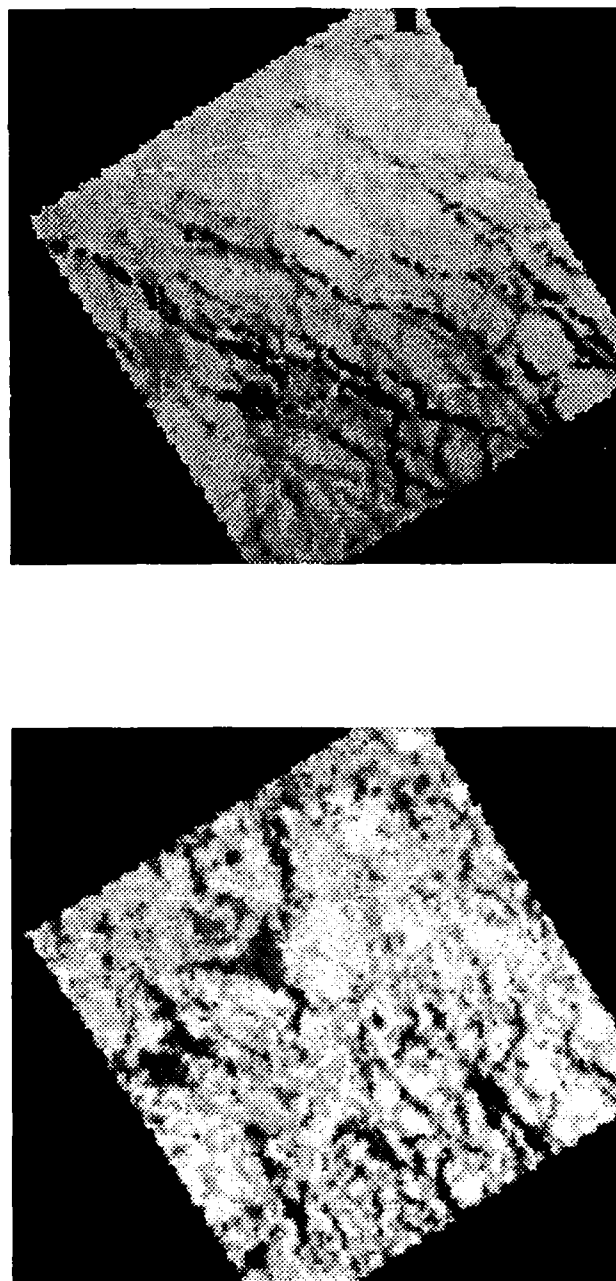
Fig. III.9. Enlarged Landsat TM Ch. 2 (a, top) and ERS-1 SAR (b) from Figure III.8.

Fig. III.10. Co-registered Landsat TM thermal channel 6 (top) and AVHRR thermal channel 4 (bottom) for 16 April 1992.

Fig. III.11. Co-located SAR and AVHRR coverage for the central Beaufort Sea. Typical lead widths in the SAR data are about 500 m. Some lead patterns probably consisting of thin, warmer ice are apparent in the AVHRR image but not in the SAR data.
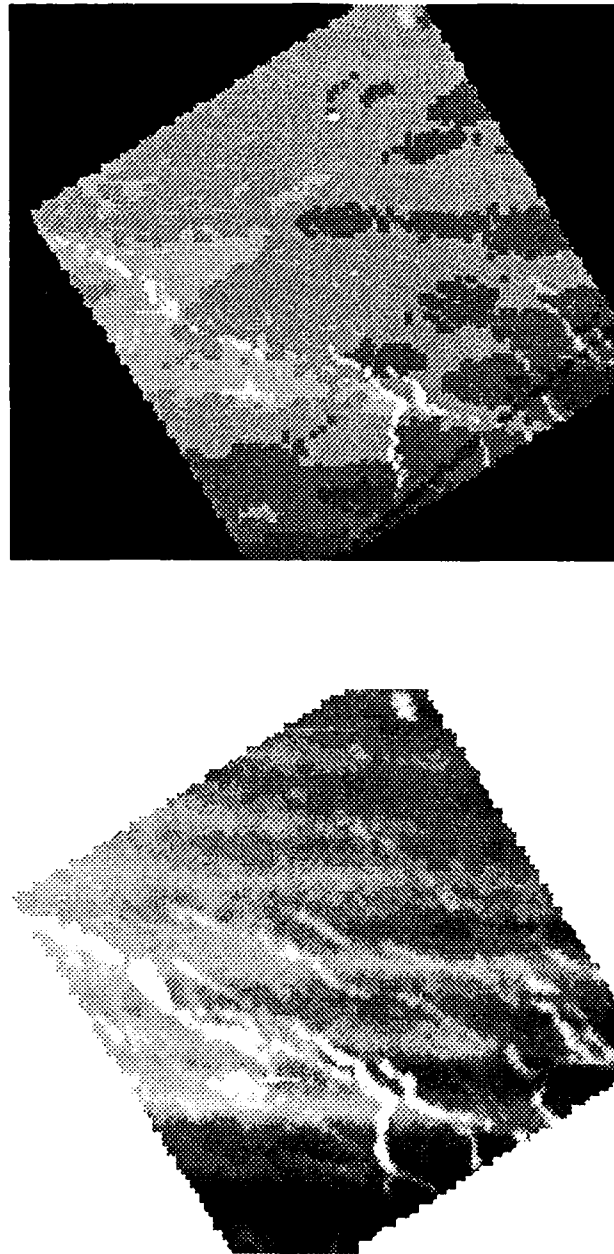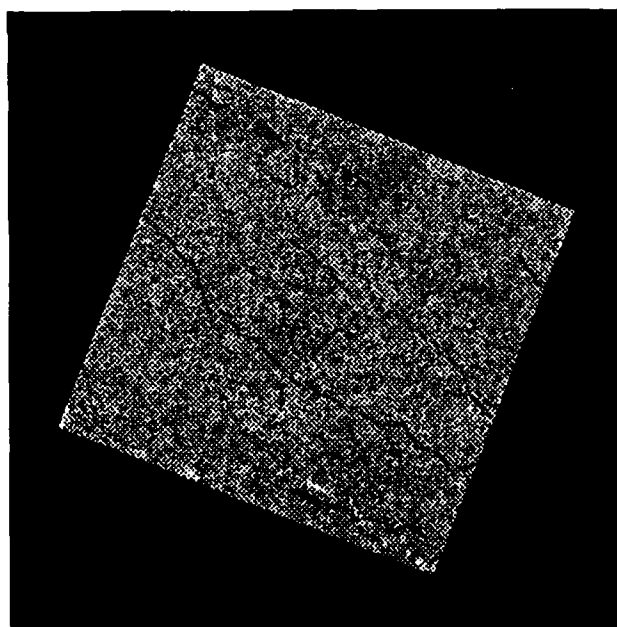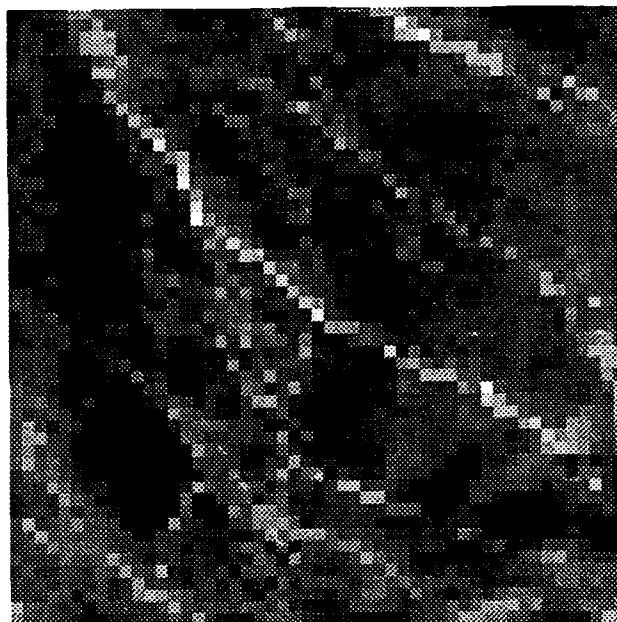
III.3 VALIDATION: SURFACE TEMPERATURE

Here we report on the application and validation of the IST retrieval procedure using a suite of *in situ* data collected during the May-June 1992 Seasonal Sea Ice Monitoring and Modelling Site (SIMMS) field campaign. Satellite-derived estimates of IST are compared to near-surface air temperatures, surface temperatures derived from upwelling longwave (broadband) radiation measurements, and from a thermocouple just below the snow surface. Since the satellite field-of-view (FOV) is at best 1.1 km, comparisons are also made with surface temperature estimates collected over an approximately 1 km^2 area with a hand-held infrared thermometer. The problems encountered are not unlike those experienced in the validation of sea surface temperatures, where there are a variety of ways of measuring the surface temperature *in situ*. Note again that the "surface" temperature refers to the skin or radiating temperature of the snow or ice surface.

III.3.1 METHODOLOGY

Surface microclimate data were collected during the SIMMS'92 (Seasonal sea-Ice Modeling and Monitoring Site) field experiment. The first-year ice (FYI) site [74° 41.66' N, 95° 35.22' W] was the focus of the measurement program and operated from 19-April to 26-June. Air temperatures were measured with thermocouple sensors. All sensors are accurate to within approximately 0.3° C. The sensors were housed within ventilated phychrometer shieldings. While air temperatures were measured at five vertical levels, the air temperature sensor used for this study (Ta1) ranged in height between 54 cm and 57 cm above the snow surface from May 10 to May 24, and between 47 cm and 65.5 cm after May 24 to the end of the experiment. As with air temperatures, snow temperatures were measured in profile within the snow cover extending from the snow/ice interface to near the snow surface, using a thermocouple epoxied in the tip of white plastic tubing (20 cm x 0.5 cm). All sensors and leads were painted white. The temperature from the thermocouple nearest the surface, the depth of which varied from 0-3 cm, is used here.

Downwelling sky and surface emitted broadband infrared radiation (4-50 μm) were measured with Eppley Precision Infrared Radiometers. One of these pyrgeometers was mounted on an extension arm approximately 8.9 m from the snow surface on an instrument tower. A sky facing pyrgeometer was mounted on a post, approximately 35 m west of the instrument tower. Instrument height was approximately 1.5 m above the snow surface. The flux measurement was corrected for the infrared radiation emitted by the thermopile using the Stefan Boltzman equation and a measure of the internal instrument temperature as recorded using the precision thermistor (YSI 44031) housed within the instrument. Thermistor tolerance is approximately ±0.125° C between -10° and -20° C; however the measurement error is probably closer to ±0.2° C when logged to the 21X micrologger. Regardless of theses specifications, the accuracy of the instrument is difficult to quantify because of possible heating of the instrument dome due to absorbed incident short-wave radiation; consequently, the temperature of the dome was also monitored in order to assess the degree to which any heating of the dome may bias the flux measurements.

The surface thermodynamic temperature based on pyrgeometer data, T_{pyrg}, was estimated from the upwelling longwave radiation emitted by the surface, $L\uparrow_{surf}$ according to the Stefan-Boltzman law:

$$T_{pyrg} = \left(\frac{L\uparrow_{surf}}{\sigma \, \varepsilon}\right)^{\frac{1}{4}} - 273.15$$

where T_{pyrg} is in degrees C, σ is Boltzman's constant, and ε is the emissivity, taken to be 0.99 here. However, because the emissivity is less than unity, the upwelling radiation measured by the sensor, $L\uparrow$, is the sum of the radiation emitted by the surface, $L\uparrow_{surf}$, and that portion of the downwelling atmospheric radiation, $L\downarrow$, that is reflected by the surface:

$$L\uparrow = L\uparrow_{surf} + (1-\varepsilon)L\downarrow$$

so that this reflected component must be removed from the upwelling radiance before calculating the surface temperature. The discussion in the appendix suggests that the uncertainty surrounding our T_{pyrg} estimate is approximately ±0.2° C.

In order to characterize the spatial variability of the temperature field over an area comparable to an AVHRR pixel, skin temperatures measured with an infrared (IR) thermometer ($T_{IRtherm}$) and snow/ice interface temperatures ($T_{s,i}$) were measured along transects within the 1 x 1 km sample site and the multiyear site. Each set of surface observations at the FYI site consisted of measurements spaced 200 m apart along two randomly-selected 1 km transects, with the time between measurements kept to a minimum. The typical time required to cover the ten stops was about 90 minutes, with sampling times selected to correspond to AVHRR overpasses whenever possible. $T_{IRtherm}$ was measured with an Everest[tm] hand-held IR thermometer; a non-contact instrument that determines a brightness temperature of the object within the instrument's field-of-view based on received radiation in the 8-14 μm range. The instrument is factory-calibrated to yield a representative accuracy of 0.5°C in an operating environment of 0° - 50°C. The manufacturer estimates that accuracy below 0°C is approximately the same. The instrument was tested periodically by measuring the temperature of fresh water at its freezing point in a slush bucket, where the IR thermometer typically yielded temperatures of +/- 0.3°C. During measurements along the transects, the IR thermometer was allowed to reach equilibrium temperature with its surroundings. Measurements were taken with the IR thermometer held about 1 m from the surface at an angle to the surface of approximately 45°. Emissivity of the snow-covered sea ice was set at 0.99.

For the retrieval of IST we use the methodology of *Key and Haefliger* (1992), as described in an earlier section. Local Area Coverage (1.1 km field-of-view at nadir) data from the NOAA-11 and NOAA-12 satellites collected by Atmosphere Environment Service are used. First-order calibration was performed following the methods described in NOAA (1991a). Additional corrections were applied to the data to account for the nonlinear response of the thermal channels (Weinreb et al., 1990; NOAA, 1991b). The AVHRR scan angle ranges from 0° to approximately 55°. Since the IST retrieval can only be done for clear sky conditions, and because automated cloud detection in the polar regions is difficult at best, images that are clear over the first-year ice site are selected through a visual analysis of various combinations of the AVHRR visible, near-infrared, and thermal channels. However, it appears that even this manual interpretation of the imagery may not be adequate for detecting low-level ice crystal precipitation ("diamond dust") and very thin stratus.

III.3.2 RESULTS

The near-surface air temperature, T_{air}, the surface temperature from the thermocouple buried just beneath the snow surface, T_{snow}, and the temperature based on upwelling longwave radiation, T_{pyrg}, are

shown in Figure III.12 for May and June, at a solar time of approximately 1000. Values for T_{snow} represent all measurents where the thermocouple was less than 3 cm below the snow-air interface. The snow temperature is typically higher than the other two temperature measurements in the early part of the experiment due to the insulating effect of the overlying snow. Snow temperatures are sometimes greater than the melting point of the snow after the initial stages of melt onset in late June due to warming of the sensor by increased transmission of solar radiation throughout the snow layer. Table III.3 provides a statistical comparison of the different measures of "surface" temperature. The two periods in May reflect early spring (8-18 May) and the transition to late spring conditions (20-24 May), when surface air temperatures become warmer than $T_{s,i}$, signifying a change in the direction of heat transport toward warming of the ice surface at the snow/ice interface. $T_{IRtherm}$ and $T_{s,i}$ were grouped, and averaged over half hour intervals to coincide with the half hour averages of T_{pyrg} and T_{air}.

Table III.3. Comparison of mean temperatures (°C) and range of differences for 8-25 May at the FYI site.

	Time Period		
	8-18 May	20-25 May	8-25 May
Mean Temperatures:			
T_{pyrg}	-13.39	-6.74	-11.76
T_{air}	-14.74	-7.72	-13.02
$T_{IRtherm}$	-13.90	-6.52	-12.09
$T_{s,i}$	-8.92	-6.40	-8.15
Temperature Differences:			
$T_{IRtherm} - T_{pyrg}$:			
Mean Difference	-0.51	0.22	-0.33
Standard Dev.	0.62	0.62	0.69
$T_{IRtherm} - T_{air}$:			
Mean Difference	0.84	1.20	0.93
Standard Dev.	1.32	0.44	1.17
$T_{pyrg} - T_{air}$:			
Mean Difference	1.35	0.98	1.26
Standard Dev.	1.19	0.90	1.13
$T_{IRtherm} - T_{s,i}$:			
Mean Difference	-5.69	-0.42	-4.08
Standard Dev.	2.26	2.33	3.36

Values of T_{AVHRR} are plotted with T_{pyrg} in Figure III.13 for May and June. The temperature reported as T_{AVHRR} is a mean of 10 pixels around the FYI site whose fields-of-view contained first-year ice only (i.e., no land), covering approximately 13 km^2, depending on the sensor scan angle. Gaps in the time series result from periods of extensive cloud cover. The maximum time difference between the *in situ* and satellite observations is approximately 20 minutes. Differences between the temperature pairs range from less than 0.1 K to more than 3 K, with the satellite estimates almost always less than the *in situ* values. The differences between T_{AVHRR} and T_{air} (not shown) are less, but the sign of the difference is usually the same.

Temperatures obtained from the IR thermometer, $T_{IRtherm}$, are compared to T_{pyrg} and the snow-ice interface temperature, T_{s-i}, in Figure III.14. The systematic difference between $T_{IRtherm}$ and T_{pyrg} over the 8-25 May period is small (0.33° C difference); $T_{IRtherm}$ measuring slightly lower in early spring (-0.51° C) and slightly higher during the late spring conditions (0.22° C). The discrepancy is less than that shown in Figure III.13 between the T_{pyrg} and T_{AVHRR} which is not entirely unexpected since T_{AVHRR} represents a sample in time and T_{pyrg} a time average. The difference between $T_{IRtherm}$ and T_{pyrg} at any one time may also be large, as shown by both the fairly large standard deviations (Table III.3). Absolute differences ranged between 0.02° C and 1.80° C. T_{s-i} follows the general increase in heat input to the surface energy budget, with less da·; iu day variability because of the insulating affect of the overlying snow cover (Figure III.14). Snow depth averaged 26±9 cm from 8-25 May.

III.3.3 DISCUSSION

The temperature differences observed in our study are likely due to undetected clouds in the imagery, the spatial and temporal variability of the temperature field, incorrect assumptions concerning the surface emissivity and atmospheric conditions, inaccuracies in the model used in the development of the satellite retrieval algorithm, and instrument error.

III.3.3.1 *Undetected Clouds*

Despite the multi-spectral approach to the manual selection of clear images, there are conditions where condensed water simply cannot be detected with the spectral information that the AVHRR provides. This is particularly true for very thin clouds such as Arctic stratus. Even more difficult to detect are low-level water or ice fogs, the most common being ice crystal precipitation in winter and early spring. The problem in their detection is that they usually exist within the low-level temperature inversion and may result in top-of-atmosphere radiances very close to what would be observed in their absence; i.e., their radiative properties, both shortwave and longwave, are similar to those of the surface. This often equates to a top-of-atmosphere temperature difference of a few degrees or less.

A re-examination of the satellite data after the initial manual cloud cover assessment and a comparison with cloud observations taken at the meteorological station Resolute Airport indicate that some form of thin cloud may actually have been present over the FYI site at the times of the AVHRR acquisitions. However, as cloud conditions may differ over only a few kilometers, it is impossible to state conclusively how often this problem influences our analysis. While cloud type and opacity were estimated for the entire sky hemisphere during the IR thermometer measurements, additional information is needed concerning clouds that lie along the path between the satellite and the surface temperature measurements.

III.3.3.2 *Spatial and Diurnal Variability of Surface Temperature*

Variability of $T_{ITtherm}$ within the 1 km site arises primarily from differences in snow depth, the shadowing effects of sastrugi-like features, and changes in temperature during the time required to cover the transects. Shown are all observations of $T_{IRtherm}$ throughout the period, plotted by local time. The apparent relationship between solar zenith angle and skin temperature is biased somewhat by sampling date for times between 1600 hrs and 2000 hrs since these observations were all collected on a single day. The greatest source of spatial variability is likely due to shadowing. Measurements taken with the shaded versus sunlit aspects of sastrugi (typical height of 10 - 15 cm) filling the entire field of view of the IR thermometer yielded temperature differences of as much as 10°C in clear-sky conditions, but only 1°C when overcast. In the normal sampling, the IR thermometer was held further away from the surface to yield a larger field-of-view that typically encompassed a mixture of shadow and sunlit areas, but not necessarily in equal proportions.

Figure III.15 shows the spatial variability of T_{AVHRR} in June over a 10 pixel area around the FYI site. There were no open water or thin ice (significantly less than 1 m) areas in the scene. The standard deviation in the temperatures measured with the IR thermometer is up to twice that of the AVHRR-derived ISTs. Minimizing the time to sample the transects would reduce the variability of $T_{IRtherm}$.

The surface temperature may change rapidly in response to radiative forcing. T_{pyrg} represents an average of this temperature over a half hour period. While $T_{IRtherm}$ also represents an average, its value may be biased by the non-systematic number of samples within the averaging period (ranging from 1 to 6), the irregular time increments between samples, and by spatial variability.

III.3.3.3 *Assumptions Made in the Retrieval Procedures*

A number of questions arise concerning the assumed properties of the surface and atmosphere affecting the AVHRR data and, potentially, the pyrgeometer measurements. One such assumption concerns the emissivity of the surface for the IR thermometer measurements. All reported observations of $T_{IRtherm}$ are based on an emissivity setting of 0.990, which is the highest setting possible on the instrument. This value is probably appropriate for the broadband emissivity of snow with grain sizes in the 100 - 200 µm range, but not for the 8-14 µm spectral range of the IR thermometer. In that range, the emissivity of snow is closer to 0.993 (*Dozier and Warren*, 1982). The relationship between thermodynamic tempertaure T (K), emissivity ε, and radiance L (milliwatts/m²-steradian-cm⁻¹) is derived from the Planck function as

$$T = \frac{c_2 \lambda}{\ln\left(\frac{\varepsilon c_1 \lambda^3}{L} + 1\right)}$$

where c_1 and c_2 are constants ($c_1 = 1.1910659 \times 10^{-5}$ milliwatts/m²-steradian-cm⁻⁴ and $c_2 = 1.438833$ cm-K) and λ is the wave number (cm⁻¹). While the difference between the assumed and probable snow emissivity is not large, it does result in a temperature overestimate of approximately 0.3°C.

Additionally, the upwelling radiance measured by the instrument is the sum of the radiation emitted by the surface and the downwelling atmospheric radiation reflected by the surface. (We consider any depletion or addition of radiation from the atmosphere itself to be insignificant given the short atmospheric path from the sensor to the surface.) While the amount of downwelling atmospheric radiation reflected by the surface is relatively small given the high surface emissivity, it does increase the radiance

received by the sensor. If corrections for this effect were made, values of $T_{IRtherm}$ would be even lower and closer to the satellite-derived temperatures by an estimated 0.1 K to 0.2 K.

Assumptions concerning atmospheric conditions could play a role in explaining the differences between the satellite-derived and *in situ* temperatures. As described earlier, the retrieval algorithm is based on ice station data from the central Arctic Ocean. The coefficients were derived for three seasons and in some sense represent the mean conditions during those periods. How do these mean conditions compare with those observed during SIMMS'92? May falls into the transition season of *Key and Haefliger* (1992), while June falls into their summer season. Differences between the ice station and the SIMMS location (represented by nearby Resolute) are shown in Table III.4 in for total precipitable water, near-surface air temperature and aerosol optical depths. No information is available on the actual aerosol optical depth at the drifting ice station so that the value shown in the table is the assumed amount used in model calculations. While the surface air temperatures at the two locations (and times) are different, the range of temperatures used in the development of the IST retrieval algorithm is similar to that experienced during SIMMS'92. The water vapor amounts are also similar. Aerosol amounts are different, primarily as a result of stratospheric aerosols from the eruption of Mt. Pinatubo, as observed during AGASP IV (Arctic Gas and Aerosol Sampling Program) over the Beaufort Sea, 1992 (*Stone et al.,* 1993 and Section III.1 of this report). Although the overall effect of aerosols on the attenuation of upwelling longwave radiation is small, an aerosol amount greater than that expected would produce a lower top-of-atmosphere radiance which, especially at significantly off-nadir views, would result in an underestimate of IST.

Table III.4. Mean precipitable water, surface temperatures, and aerosol optical depths at a drifting ice station and Resolute, N.W.T.

| | Ice Station | | Resolute | |
	Transition[1]	Summer[2]	May	June
Precipitable Water (mm)	4.6	6.6	4.2	7.1
Surface Temperature (C)	-19.4	-0.9	-13.8	-2.7
Aerosol Optical Depth	0.07[3]	0.07	2.5	2.0

[1]April, May, September, 1987
[2]June - August, 1987
[3]Assumed value for model calculations

Lastly, there may be a bias in the retrieved ISTs due to AVHRR calibration errors. This may not be trivial; for example the nonlinear calibration alone can make a difference of more than 1°C. Overall, however, we expect calibration errors to be much less, on the order of 0.1 K to 0.2 K.

III.3.3.4 *Possible Errors in the Calculation of T_{pyrg}*

Given that the adjustments to $T_{IRtherm}$ and T_{AVHRR} just discussed will decrease the differences between the two measurements, and given that both of these temperatures are typically lower than that derived from the average upwelling longwave broadband radiation T_{pyrg}, we are left wondering if there are any reasons why T_{pyrg} would be biased.

The vertical placement of the pyrgeometer at 8.9 m above the surface could play a role. Early in the season when temperature inversions are common, the atmosphere between the surface and the sensor is warmer than that of the surface. Given that the atmosphere is relatively warm, that the surface emissivity is less than unity, and that relative humidities near the surface are high, one would expect an increase in longwave radiation received at the sensor over that emitted by the surface. Radiative transfer calculations of upwelling longwave flux confirm this, although the increase in the estimated physical temperature of the surface is small, 0.3° - 0.4° C for a surface temperature of -13°C. Additionally, the large field of view associated with the pyrgeometer samples the emitted infrared radiation from a much larger area than the hand-held pyrometer, and the IR emitted by the support tower infra-structure and other 'non-snow' objects are also sampled.

Our derivation of L using the pyrgeometer assumes that any solar heating of the instrument dome, and subsequent re-radiation to the thermopile is negligible, and that the thermopile temperature is closely approximated by the case temperature. There is little reason to believe a large discrepancy in temperature between the thermopile and case thermistor given their close proximity. The net effect of the solar heating of the dome is to increase the calculated value of L. Solar heating of the dome is not expected for the inverted pyrgeometer ($L\uparrow$), and in fact the case and dome temperature differed on average by only 0.10° C between 8-25 May, with the dome being actually cooler than the case. The opposite was observed for the sky facing pyrgeometer. Slight heating of the dome for $L\downarrow$ was observed, but is not considered to be a factor that significantly influences T_{pyrg}.

III.3.4 CONCLUSIONS

In an effort to validate the satellite retrievals of ice surface temperature, differences between AVHRR-derived ice surface temperature, T_{AVHRR}, and the radiating temperature derived from measurements of upwelling longwave (broadband) radiation, T_{pyrg}, during May and June in the Canadian Arctic were observed to range from less than 0.1°C to more than 3°C with T_{AVHRR} always less than T_{pyrg}. Similarly, the mean temperatures of spatially-distributed measurements made by a hand-held IR thermometer, $T_{IRtherm}$, were typically less than T_{pyrg}, although the differences were not as great as between T_{AVHRR} and T_{pyrg}. The temperature measured by a thermocouple placed approximately 1 cm below the snow-air interface illustrates the insulating quality of the overlying snow, being higher than the radiating temperature in the early part of the season.

While these results can be explained to a limited extent by instrument calibration, incorrect assumptions of the surface emissivity and atmospheric conditions, and model inaccuracies, the main issue with a validation exercise such as this is in the definition of the "correct" surface temperature and of the method chosen to measure this temperature. The temperature of interest is the radiating temperature, not the near-surface snow temperature or the near-surface air temperature. In theory the upwelling longwave radiation can be used to determine this temperature, but in practice care must be taken to obtain an accurate value. The spatially-averaged temperatures measured with the IR thermometer suggest a possible negative bias in the AVHRR-derived temperatures, with a possible simple correction for this bias. However, the spatial and temporal variations in skin temperatures observed during the sampling of the 1 km transects with the IR thermometer are too great to permit a determination of a bias with any certainty. We conclude that there is probably a negative bias in T_{AVHRR} as computed here, on the order of 0.5° C to 1° C. To determine the actual magnitude and source of this bias we need a well-calibrated, airborne radiometer measuring in the same spectral bands as the AVHRR (to reduce the atmophseric effects and to obtain adequate spatial coverage), combined with refined surface observations that include faster sampling, more precise instrumentation, and more detailed observations on cloud properties and distributions relative to the AVHRR scan.

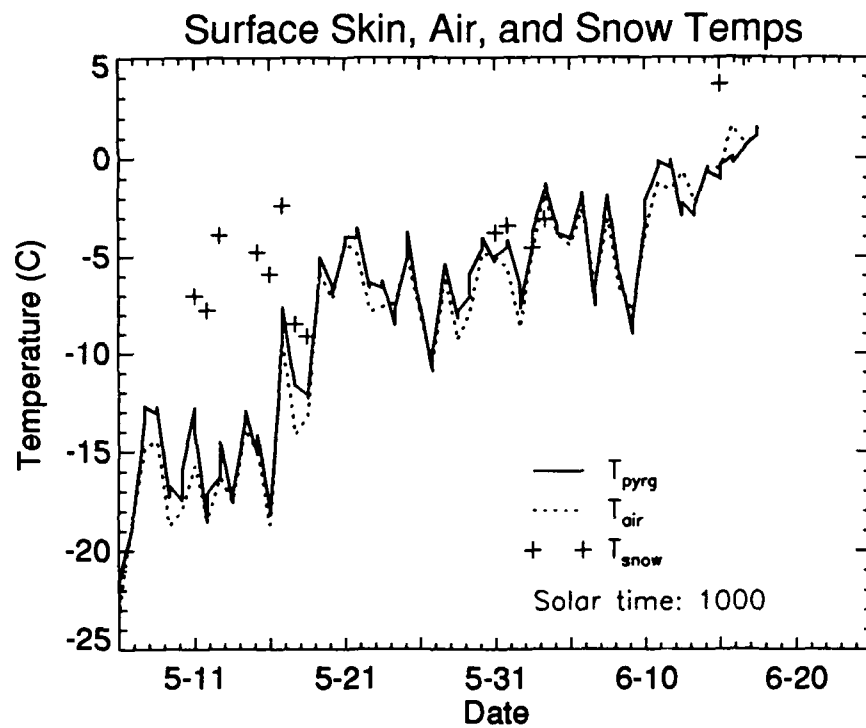## Surface Skin, Air, and Snow Temps

Fig. III.12. Near-surface air temperature, temperature measured by a thermocouple just below the surface, and temperature derived from upwelling longwave radiation at the FYI site.

AVHRR and In Situ Surface Temperatures

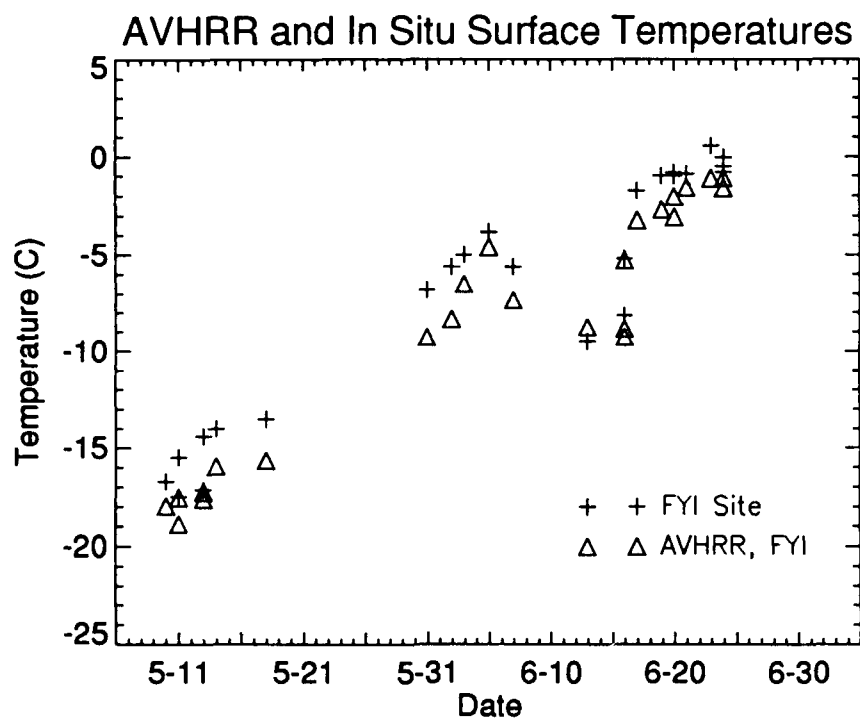Fig. III.13. Surface temperatures estimated from upwelling longwave radiation measured at the surface and from the AVHRR thermal channels at the first-year ice site during May and June.

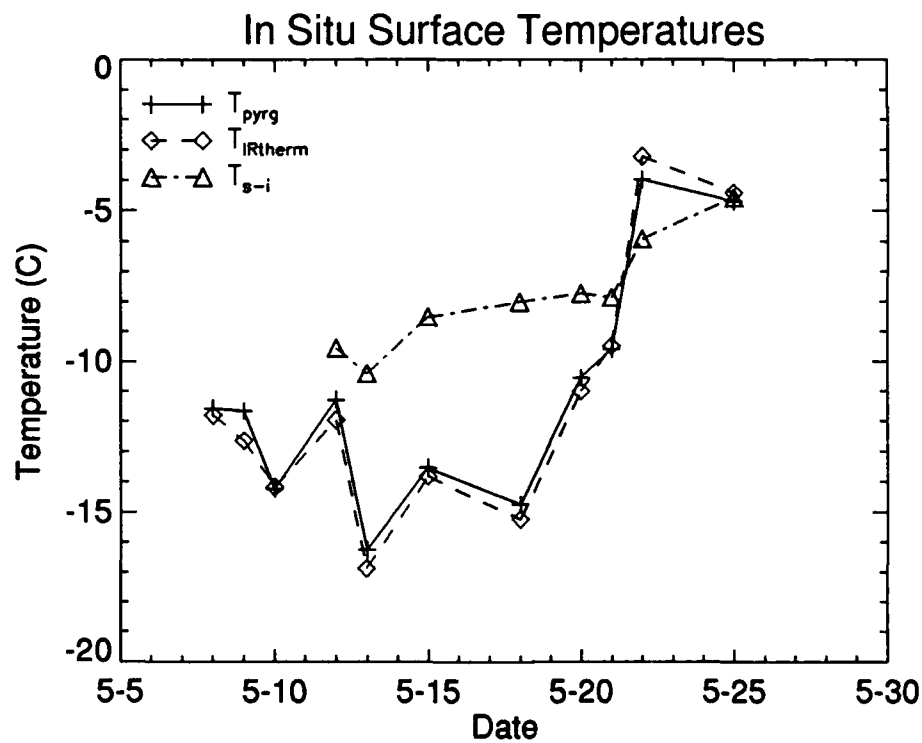## In Situ Surface Temperatures

Fig. III.14. Surface temperatures measured with the IR thermometer (spatial means) and those based on upwelling longwave radiation. Also shown are snow-ice interface temperatures measured (means).
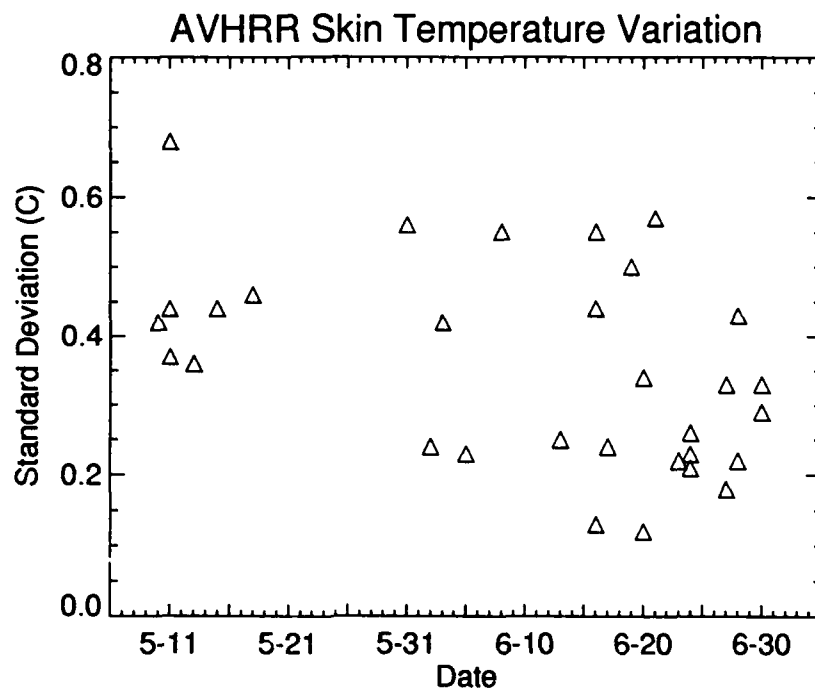
Fig. III.15. Variability of satellite-derived surface temperature within a 10-pixel area around the FYI site.

III.4 APPLICATION OF SKELETAL MODELING FOR LEAD RETRIEVAL

The method described in an earlier section for the retrieval of lead widths and orientations has one serious shortcoming: it is based on a linear regression procedure and is therefore inapplicable to leads or lead fragments that are curved. Additionally, the origin of the coordinate system upon which correlations and regression fits were based was arbitrary, but linear correlation is not insensitive to rotation. We have therefore investigated the use of a recently-developed method for the retrieval of lead geometrical characteristics: skeletal modeling (*Banfield*, 1992).

Briefly, this procedure uses skeletons, a tool from mathematical morphology, to provide a useful structural description of the shape of a lead. The skeleton of an object is the set of points that describes the "center" of the object, in this case the centers of the largest open balls that touch the boundary of the lead at two or more locations.

The procedure was applied to the AVHRR image shown in Figure III.16. Only clear sky ice areas were examined. Cloud clearing was done by applying a threshold to the channel 3 (3.7 μm) reflectances, which was estimated by subtracting the Planck radiance for that channel based on the temperature measured in channel 4 (11 μm) and dividing the remaining radiance by the solar radiance in that band.

A binary image (lead/ice) was then used as input to the code provided by J. Banfield. The results are shown in Figure III.17 for lead area, lead width, and lead skeletal length (the length along the lead as opposed to the length of the main diagonal).
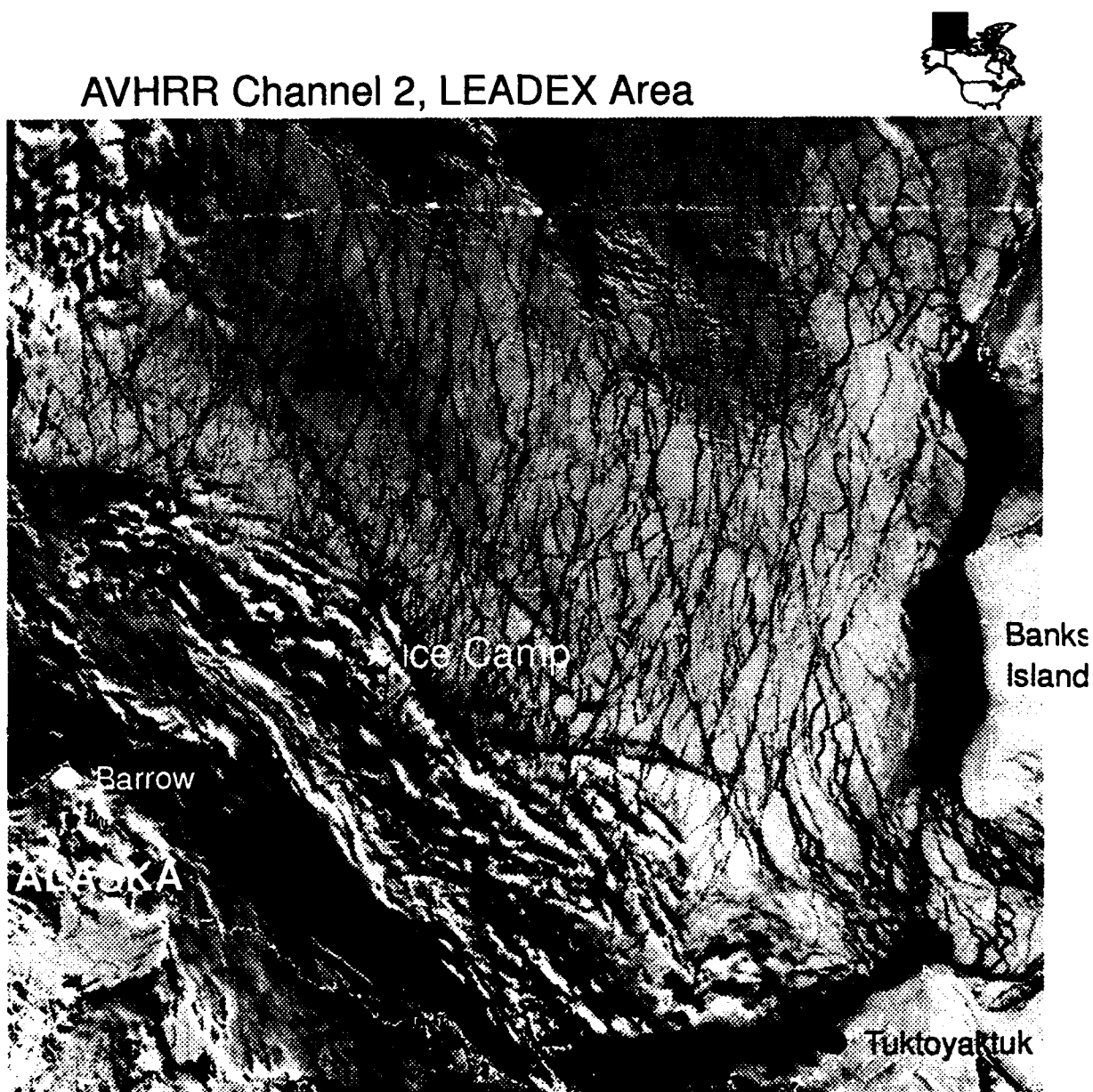
AVHRR Channel 2, LEADEX Area

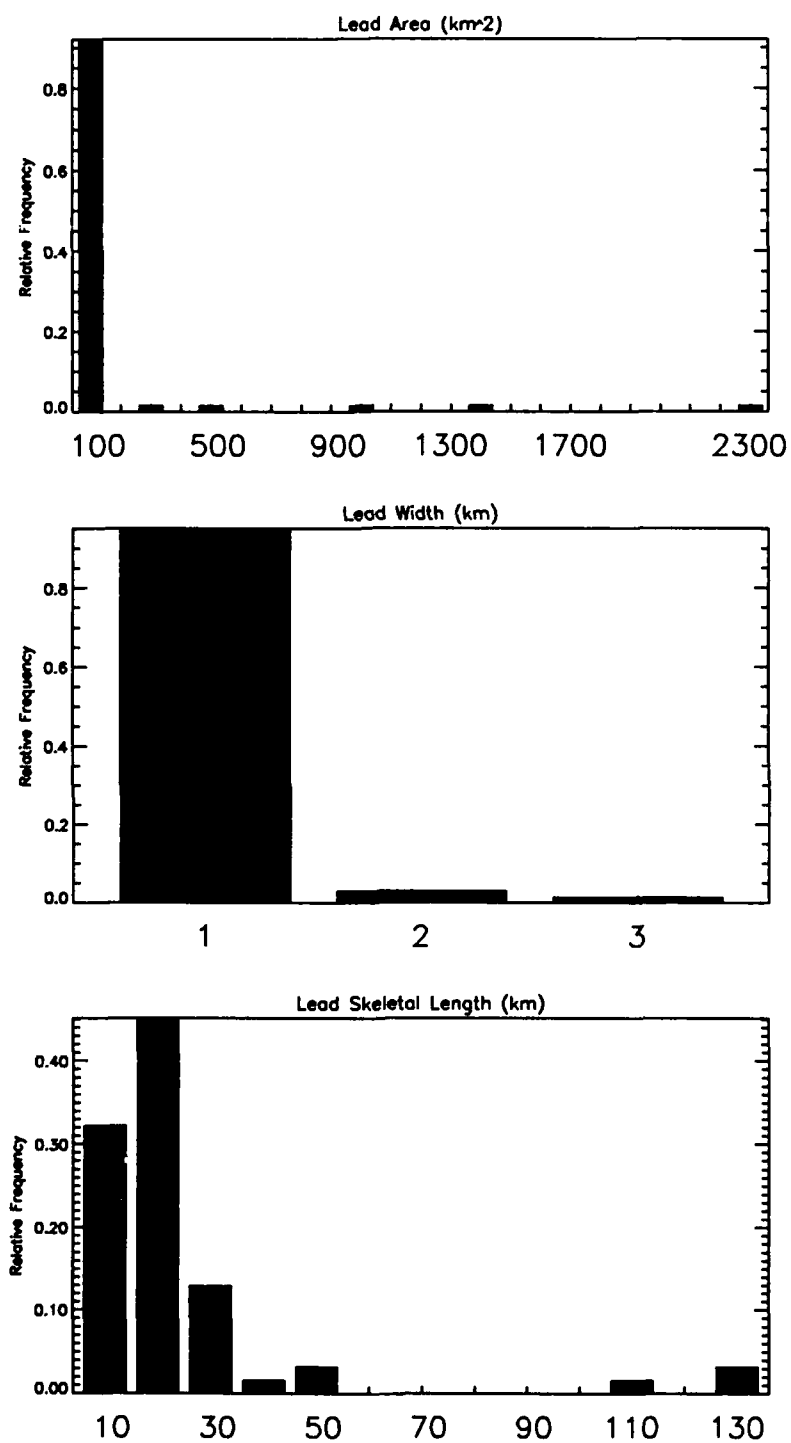Fig. III.16. AVHRR channel 2 (0.9 μm) image of the Beaufort Sea, 18 April 1992, during LEADEX.

Fig. III.17. Lead areas, widths, and skeletal lengths for the image in Figure III.16, as determined by the skeletal modeling method.

PART IV: SUMMARY OF ACCOMPLISHMENTS

IV.1 ACCOMPLISHMENTS

Over the course of this three-year project, empirical studies concerning scale relationships in the retrieval of sea ice lead statistics have been performed, as have modeling investigations of atmospheric influences on the satellite signal. Additionally, statistical models that describe the scaling properties of leads have been developed. The empirical studies have been based on Landsat imagery, while the atmospheric models have been specific to the AVHRR. Submarine sonar data have been used in the statistical model development. Specific accomplishments include:

(1) The parameterizations of clouds, haze, and atmospheric chemical constituents in the LOWTRAN-7 radiative transfer model have been reviewed. Atmospheric temperature and humidity profiles for the Arctic have been constructed from Soviet ice island data and were used in the construction of three-season "standard" atmospheres for the central Arctic.

(2) Resampling methods have been tested on simulated, AVHRR, and Landsat images, as have the effects of digital enhancements. Nearest-neighbor resampling has been shown to be the most effective in maintaining the geometrical and spectral characteristics of leads.

(3) Empirical relationships between pixel size and lead width have been illustrated.

(4) Procedures for the retrieval of lead statistics have been developed and applied to Landsat imagery successively degraded to more coarse resolutions. Applications to ERS-1 SAR data have also been explored, although a single-channel SAR does not appear to provide adequate spectral information for ice type discrimination. New methods of retrieving lead statistics utilizing mathematical morphological techniques have been applied to AVHRR data collected during LEADEX.

(5) The relationship between "apparent" lead widths measured along a transect (e.g., from submarine sonar or as a sampling method for satellite imagery) and the "true" lead width distribution has been formalized in a statistical sense, so that one distribution may be obtained from the other. Submarine sonar data have been analyzed in this context.

(6) A statistical model has been developed for the retrieval of lead area fraction from measurements along a line; e.g., a submarine sonar transect or a lineal sampling method for satellite images.

(7) The effects of atmosphere/surface conditions on the AVHRR-measured radiance in the thermal channels have been examined in terms of the thermal contrast between leads and the surrounding ice pack. Surfaces include open water, 5 cm, 15 cm, and 2 m thick ice. Atmospheric conditions include clear sky with haze, cirrus, and low-level ice crystal plumes. The relationship between atmospheric optical depth and lead size has been quantified.

(8) Information on Arctic aerosol optical depths during LEADEX has been collected by two of the

investigators on the NOAA P-3 with sun photometers. This data has been used to assess the extent of tropospheric and stratospheric aerosols and their effect on lead detection from satellite.

(9)   Satellite and *in situ* data collected during LEADEX and SIMMS'92 have been used to test the theoretical and empirical models/methods developed during the first two project years, and shows these models/methods to be generally valid.

Additionally, two workshops for the satellite remote sensing investigators of the Leads ARI prior to LEADEX were hosted by this group in Boulder. Seven referreed papers have been published, with three others submitted for publication. Two graduate students have been supported part-time over the course of the project.

IV.2 RECOMMENDED RESEARCH

Future work should include an investigation of the shortwave channels of the AVHRR and OLS sensors, following a methodology similar to that presented here for the thermal channels; i.e., the effects of aerosols, clouds and ice crystal precipitation on upwelling radiation should be examined. Concerning the retrieval of lead geometrical characteristics, using the visible and near-infrared channels should aid in the unmixing of pixels containing a lead of unknown ice thickness and "background" ice, where having measurements at a variety of wavelengths should reduce the number of possible ice thickness/lead width combinations, as suggested earlier.

IV.3 PAPERS SUPPORTED IN WHOLE OR IN PART BY N00014-90-J-1840

IV.3.1 REVIEWED JOURNALS

Key, J. and S. Peckham, 1991. Probable errors in width distributions of sea ice leads measured along a transect. *J. Geophys. Res.*, 96(C10), 18417-18423.

Key, J. and M. Haefliger, 1992. Arctic ice surface temperature retrieval from AVHRR thermal channels. *J. Geophys. Res.*, 97(D5), 5885-5893.

Stone, R. and J. Key, 1993. The detectability of winter sea ice leads in thermal satellite data under varying atmospheric conditions. *J. Geophys. Res.*, 98(C7), 12469-12482.

Key, J., R. Stone, J. Maslanik, and E. Ellefsen. The detectability of sea ice leads in satellite data as a function of atmospheric conditions and measurement scale. *Annals Glaciol.*, 17, 227-232.

Maslanik, J. and J. Key. Comparison and integration of ice-pack temperatures derived from AVHRR and passive microwave imagery. *Annals Glaciol.*, 372-378.

Stone, R.S., J. Key, and E. Dutton. Properties and decay of stratospheric aerosols in the Arctic following the 1991 eruptions of Mount Pinatubo. *Geophys. Res. Letters*, 20(21), 2359-2362.

Key, J, 1993. Estimating the area fraction of geophysical fields from measurements along a transect. *IEEE Trans. Geosci. Remote Sensing*, September 1993 (issue forthcoming).

Key, J., J.A. Maslanik, T. Papakyriakou, M.C. Serreze, and A.J. Schweiger. On the validation of satellite-derived sea ice surface temperature. *Arctic*, in press.

Key, J., J.A. Maslanik, and E. Ellefsen. The effects of sensor field-of-view on the geometrical characteristics of sea ice leads and implications for large-area heat flux estimates. *Remote Sensing Environ.*, in press.

Key, J. The area coverage of geophysical fields as a function of sensor field-of-view. *Remote Sensing Environ.*, in press.

Fowler, C., J.A. Maslanik, J. Heinrichs, and W.J. Emery, Responses of a high-concentration ice cover to synoptic weather systems, *J. Geophys. Res.*, in preparation.

IV.3.2 CONFERENCE PROCEEDINGS AND REPORTS

Key, J. and M. Haefliger, 1991. Retrieval of ice surface temperature, outgoing longwave radiation, and cloud cover from AVHRR data. WMO Report on **Polar Radiation Fluxes and Sea Ice Modeling**, WCRP-62, WMO/TD-No. 442, C22-C28.

Stone, R.S., E. Dutton, and J. Key, 1994. Properties and decay of Pinatubo aerosols in the Arctic compared with tropical observations. Proceedings of the Sixth AMS Conference on Climate

Variations, 23-28 January, forthcoming (January).

Key, J., R.S. Stone, and J. Maslanik, 1994. Retrieval of lead characteristics using visible and thermal AVHRR imagery: validation of theory with leadex data. IGARSS'94, forthcoming (August).

Key, J., A. Schweiger, R. Stone, and M. Haefliger, 1994. Estimating high-latitude radiative fluxes from satellite data: requirements, problems, and possibilities. IGARSS'94, forthcoming (August).

REFERENCES

Andreas, E.L., C.A. Paulson, R.M. Williams, R.W. Lindsay, and J.A. Businger, The turbulent heat flux from Arctic leads, *Boundary Layer Meteorol, 17*, 57-91, 1979.

Asano, S., *et al.*, Spectral optical thickness and size distributions of the Pinatubo volcanic aerosols as estimated by ground-based sunphotometry, *J. Meteorol. Soc. Jpn., 71*(1), 165-173, 1993.

Banfield, J., Skeletal modeling of ice leads, *IEEE Trans. Geosci. Remote Sensing, 30*(5), 918-923, 1992.

Blanchet, J. and R. List, Estimation of optical properties of arctic haze using a numerical model, *Atmos.-Ocean, 21*, 444-465, 1983.

Blanchet, J., and R. List, On radiative effects of anthropogenic aerosol components in Arctic haze and snow, *Tellus, 39*B, 293-317, 1987.

Bluth, G.J.S., *et al.*, Global tracking of the SO_2 clouds from the June, 1991 Mount Pinatubo eruptions, *Geophys. Res. Lett., 19*(2), 151-154, 1992.

Cahalan, R.F. and J.H. Joseph, Fractal statistics of cloud fields, *Monthly Wea. Rev., 117*(2), 261-272, 1989.

Curry, J.A., Meyer, F.G., and Ebert, E.E., Cloudless ice crystal precipitation in the polar regions, in Lenoble, J. and Creleyn, J.F. (eds) *IRS'88 Current Problems in Atmospheric Radiation*, A. Deepak Press, 80-83, 1989a.

Curry, J.A., Radke, L.F., Brock, C.A., and Ebert, E.E., Arctic ice-crystal haze, *AMS Symposium on the Role of Clouds in Atmospheric Chemistry and Global Climate*, Preprint Volume, 114-117, 1989b.

Curry, J.A., F.G. Meyer, L.F. Radke, C.A. Brock, and E. Ebert, Occurrence and characteristics of lower tropospheric ice crystal in the Arctic. *Int. J. Climatology, 10*, 749-764, 1990.

Curry, J.A., J. Schramm, and E.E. Ebert, Impact of clouds on the surface radiation balance of the Arctic Ocean. *Meteorol. Atmos. Phys., Polar Issue*, 1992.

De Cola, L., Fractal analysis of a classified Landsat scene, *Photogram. Eng. Remote Sens., 55(5)* 601-610, 1989.

Dozier, J. and S.G. Warren, Effect of viewing angle on the infrared brightness temperature of snow, *Water Resources Res., 18*(5), 1424-1434, 1982.

Deshler, D., *et al.*, Balloonborne measurements of the Pinatubo aerosol size distribution and volatility at Laramie, Wyoming during the summer of 1991, *Geophys. Res. Lett., 19*, 199-202, 1992.

Dickins, D., A. Dickinson, and B. Humphrey, Pack ice in Canadian waters: dimensions and dynamics of leads and floes, unpublished report to the Environmental Emergencies Technology Division, Environmental Protection Service, Ottawa, Ontario, 62pp., 1986.

Dutton, E.G., *et al.*, Features of aerosol optical depth observed at Barrow, March 10-20, 1983, *Geophys. Res. Lett., 11*(5), 385-388, 1984.

Dutton, E.G., *et al.*, Shortwave aerosol optical depth of Arctic haze measured on board the NOAA WP-3D during AGASP-II, April 1986, *J. Atmos. Chem., 9*, 71-79, 1989.

Dutton, E.G., and J.R. Christy, Solar radiative forcing at selected locations and evidence for global lower tropospheric cooling following the eruptions of El Chichon and Pinatubo, *Geophys, Res. Lett., 19*(23), 2313-2316, 1992.

Eppler, D.T. and W.E. Full, Polynomial trend surface analysis applied to AVHRR images to improve definition of Arctic leads. *Remote Sensing of Environ.*, 1992.

Falls, L.W., The beta distribution: a statistical model for world cloud cover, *J. Geophys. Res., 79*(9):1261-1264, 1974.

Francis, J., Improvements to TOVS retrievals over sea ice and their application to estimating Arctic energy fluxes. *Third Conference on Polar Meteorology and Oceanography*, AMS, Portland, 29 Sept - 2 Oct, 25-28, 1992.

Gerber, H.E., and Deepak, A., (eds.), *Aerosols and Their Climatic Effects*, A. Deepak Publishing, 1984.

Gringorten, I.I., Probability models of weather conditions occupying a line or area, *J. Appl. Meteorol.*, *18*, 957-977, 1979.

Gupta, V.K. and E.C. Waymire, A statistical analysis of mesoscale rainfall as a random cascade, *J. Applied Meteorol.*, 1992.

Hansen, J., *et al.*, Potential climate impact of Mount Pinatubo eruption, *Geophys. Res. Lett.*, *19*(2), 215-218, 1992.

Hanel, G., The properties of atmospheric aerosol particles as functions of the relative humidity at thermodynamic equilibrium with the surrounding moist air, in *Advances in Geophysics*, *19*, 73-188, H.E. Landsberg and J. Van Meighem (eds.), Academic Press, New York, 1976.

Harris, J.M., and B.A. Bodhaine, Eds., Geophysical Monitoring for Climatic Change No. 11: Summary Report 1982, NOAA/ARL/GMCC, Boulder, Colo., 160 pp., 1983.

Heinrichs, J., J.A. Maslanik, and K. Steffen, The seasonal cycle of multiyear ice in the Beaufort Sea as revealed by ERS-1 SAR data. EOS abstracts, pp 336, 1993.

Henderson-Sellers, A. and I. McGuffie, Investigation of the Burger distribution to characterize cloudiness, *J. Climate*, *4*, 1181-1209, 1992.

Herman, G.F., and J.A. Curry, Observational and theoretical studies of solar radiation in Arctic stratus clouds. *J. Clim. Appl. Meteor.*, *23*, 5-24, 1984.

Heymsfield, A.J., and C.M.R. Platt, A parameterization of the particle size spectrum of ice clouds in terms of the ambient temperature and the ice water content, *J. Atmos. Sci.*, *41*, 846-855, 1984.

Hobbs, P.V., *Ice Physics*, Oxford University Press, London, 1974.

Huschke, R.E., Arctic Cloud Statistics from Air Calibrated Surface Weather Observations. *Mem. RM-6173-PR*, Rand Corp., Santa Monica, CA, 79, 1969.

Herbert, G.A., *et al.*, Analysis of meteorological conditions during AGASP-IV: March 30-April 23, 1992, *NOAA Tech. Memo. ERL CMDL-5*, NOAA/ERL/Climate Monitoring and Diagnostics Lab., Boulder, Colo., 118 pp., 1993.

Hofmann, D.J., and J.M. Rosen, On the prolonged lifetime of the El Chichon sulfuric acid aerosol cloud, *J. Geophys. Res.*, *92*(D8), 9825-9830, 1987.

Jones, J.G., R.W. Thomas, and P.G. Earwicker, Multiresolution analysis of remotely sensed imagery, *Int. J. Remote Sensing*, *12*(1), 107-124, 1991.

Jones, P.A., Cloud-cover distributions and correlations, *J. Appl. Meteorol.*, *31*(7), 732-741, 1992.

Jupp, D.L.B., A.H. Strahler, and C.E. Woodcock, Autocorrelation and regularization in digital images I. Basic theory, *IEEE Trans. Geosci. Remote Sensing*, *26*(4):463-473, 1988.

Jupp, D.L.B., A.H. Strahler, and C.E. Woodcock, Autocorrelation and regularization in digital images II. Simple image models, *IEEE Trans. Geosci. Remote Sensing*, *27*(3), 247-258, 1989.

Justice, C.O., B.L. Markham, J.R.G. Townshend, and R.L. Kennard, Spatial degradation of satellite data. *Int. J. Remote Sens.*, *10*(9), 1539-1561, 1989.

Kahl, J.D., and A.D.A. Hansen, Determination of regional sources of aerosol black carbon in the Arctic, *Geophys. Res. Let.*, *16*, 327-330, 1989.

Karlinger, M.R. and B.M. Troutman, Fat fractal scaling of drainage networks from a random spatial network model, *Water Resources Res.*, *28*(7), 1975-1981, 1992.

Key, J. and R.G. Barry, Cloud cover analysis with arctic AVHRR data: 1. cloud detection, *J. Geophys. Res.*, *94*(D15), 18521-18535, 1989.

Key, J., A.J. Schweiger, and J.A. Maslanik, 1990. Mapping sea ice leads with a coupled numeric/symbolic system. *ACSM/ASPRS Proceedings, Vol. 4*, Denver, Colorado, 228-237, 1990.

Key, J., and S. Peckham, Probable errors in width distributions of sea ice leads measured along a transect, *J. Geophys. Res.*, *96*(C10), 18417-18423, 1991.

Key, J., and M. Haefliger. Arctic ice surface temperature retrieval from AVHRR thermal channels. *J. Geophys. Res.*, *97*(D5), 5885-5893, 1992.

Key, J., R. Stone, J. Maslanik, and E. Ellefsen, The detectability of sea ice leads in satellite data as a function of atmospheric conditions and measurement scale. *Annals Glaciol.*, *17*, 227-232, 1992.

Key, J., The effect of sensor field-of-view on the observed area coverage of geophysical fields, *Remote Sensing Environ.*, 1993. (in press)

Key, J., E. Ellefsen, and J. Maslanik, Effects of satellite sensor field-of-view on the retrieved geometrical characteristics of sea ice leads, *Remote Sensing Environ.*, submitted, September, 1993.

Kidder, S.Q., and H.-T. Wu, Dramatic contrast between low clouds and snow cover in daytime 3.7 µm imagery, *Mon. Weather Rev.*, *112*(11), 2345-2346, 1984.

Kneizys, F.X., E.P. Shettle, W.O. Gallery, J.H. Chetwynd, Jr., L.W. Abreu, J.E.A. Selby, R.W. Fenn, and R.A. McClatchy, Atmospheric Transmittance/Radiance: Computer Code LOWTRAN 5, AFGL-TR-80-0067, *Environmental Research Papers*, *no.697*, 233 pp., 1980.

Kneizys, F.X., E.P. Shettle, W.O. Gallery, J.H. Chetwynd, L.W. Abreu, J.E.A. Selby, S.A. Clough, and R.W. Fenn, Atmospheric transmittance/radiance: computer code LOWTRAN 6, *AFGL-TR-83-0187* (NTIS AD A137796), 1983.

Kneizys, F.X., E.P. Shettle, L.W. Abreu, J.H. Chetwynd, G.P. Anderson, W.O. Gallery, J.E.A. Selby, and S.A. Clough, Users Guide to LOWTRAN 7, AFGL- TR-88-0177, *Environmental Research Papers*, *no.1010*, 137 pp., 1988.

Konig-Langlo, G., and A. Zachek, Radiation budget measurements over Antarctic sea ice in late winter, *World Climate Research Programme, Sea-Ice and Climate, WCRP-62, WMO/TD-No. 442*, 1991.

Lacis, A., J. Hansen, and M. Sato, Climate forcing by stratospheric aerosols, *Geophys. Res. Lett.*, *19*(15), 1607-1610, 1992.

Ledley, T.S., A coupled energy balance climate-sea ice model: Impact of sea ice and leads on climate, *J. Geophys. Res.*, *93*(D12), 15915-15932, 1988.

Lovejoy, S., Area-perimeter relation for rain and cloud areas, *Science*, *216*, 185-187, 1982.

King, M.D., *et al.*, Aerosol size distributions obtained by inversion of spectral optical depth measurements, *J. Atmos. Sci.*, *35*, 2153-2167, 1978.

Marko, J.R. and R.E. Thomson, Rectilinear leads and internal motions in the ice pack of the western Arctic ocean, *J. Geophys. Res.*, *82*(6), 979-987, 1977.

Maslanik, J.A. and R.G. Barry, Short-term interactions between atmospheric synoptic conditions and sea ice behavior in the Canada Basin, *Annals Glaciol.*, *12*, 113-117, 1989.

Maslanik, J.A., C. Fowler, and W. Emery, Response of the Beaufort ice pack to synoptic weather systems: multisensor observations and large-scale simulations. EOS abstracts, pp. 335, 1993.

Maykut, G.A., Large-scale heat exchange and ice production in the central Arctic, *J. Geophys. Res.*, *87*(C10), 7971-7984, 1982.

Maykut, G.A. and D.K. Perovich, The role of shortwave radiation in the summer decay of a sea ice cover, *J. Geophys. Res.*, *92*(C7), 7032-7044, 1987.

McLaren, A.S., The under-ice thickness distribution of the Arctic Basin as recorded in 1958 and 1970, *J. Geophys. Res.*, *94*(C4), 4971-4983, 1989.

McCormick, M.P., *et al.*, Spatial changes in the stratospheric aerosol associated with the north polar vortex, *Geophys. Res. Lett.*, *10*(10), 941-944, 1983.

McCormick, M.P., and C.R. Trepte, Polar stratospheric optical depth observed between 1978 and 1985, *J. Geophys. Res.*, *92*(D4), 4297-4306, 1987.

Mendonca, B.G., J.J. DeLuisi, and J.A. Schroeder, Arctic haze and perturbations in the solar radiation fluxes at Barrow, Alaska, *Proceedings from 4th Conference on Atmospheric Radiation*, AMS, Toronto, Ontario, Canada, 95-96, June 1981.

Miles, R.E., Random polygons determined by random lines in a plane, *Proc. National Academy Sci.*, *52*, 901-907, 1964.

Minnis, P., *et al.*, Radiative climate forcing by the Mount Pinatubo eruption, *Science*, *259*, 1411-1415, 1993.

NOAA, *NOAA Polar Orbiter Data User's Guide*, U.S. Dept. of Commerce., National. Ocean. and Atmos. Admin., NESDIS, February 1991.

Platt, C.M.R., and Harshvardhan, Temperature dependence of cirrus extinction: Implication for climate feedback, *J. Geophys. Res*, *93*, 11,051-11058, 1988.

Rahn, K.A., and McCaffrey, On the origin and transport of the winter Arctic aerosol, *Ann. N.Y. Acad. Sci.*, *338*, 486-503, 1980.

Reddan, *et al.*, The SIMMS'92 data report, *ISTS-EOL-SIMS-TR-92-003*, Earth Observations Laboratory, University of Waterloo, 226 pp., 1992.

Reddy, P.J., *et al.*, Aerosol optical depths over the Atlantic derived from shipboard sunphotometer observations during the 1988 global change expedition, *Global Biochem. Cycles.*, *4*(3), 225-240, 1990.

Robert, A. and A.G. Roy, On the fractal interpretation of the mainstream length-drainage area relationship, *Water Resources Res.*, *26*(5), 839-842, 1990.

Robock, A., and J. Mao, Winter warming from large volcanic eruptions, *Geophys. Res. Lett.*, *12*(24), 2405-2408, 1992.

Rosen, H.T., Novakov, and B.A. Bodhaine, Soot in the Arctic, *Atmos. Environ.*, *15*, 1371-1374, 1981.

Ross, S., *A First Course in Probability*, 2nd edition. New York: Macmillan Publishing Company, 392 pp., 1984.

Rossow, W.B., L.C. Garder, and A.A. Lacis, Global, seasonal cloud variations from satellite radiance measurements. Part I: sensitivity of analysis, *J. Climate*, *2*, 419-458, 1989.

Rothrock, D.A. and A.S. Thorndike, Measuring the sea ice floe size distribution, *J. Geophys. Res.*, *89*(C4), 6477-6486, 1984.

Sakellariou, N.K., H.G. Leighton, and Z. Li, Identification of clear and cloudy pixels at high latitudes from AVHRR radiances, *Int. J. Remote Sensing*, in press.

Schnell, R.C., R.G. Barry, M.W. Miles, E.L. Andreas, L.F.Radke, C.A. Brock, M.P. McCormick, and J.L. Moore, Lidar detection of leads in Arctic sea ice, *Nature*, *339*, 530-532, 1989.

Serreze, M.C., J.D. Kahl, and R.C. Schnell, Low-level temperature inversions of the Eurasian Arctic and comparisons with Soviet drifting station data, *J. Climate*, *5*(6), 599-613, 1992.

Serra, J., *Image analysis and mathematical morphology*. London: Academic Press, 1982.

Shaw, G.E., Sun photometry, *Bull. Am. Meteorol. Soc.*, *64*(1), 4-10, 1983.

Shenk, W.E. and V.V. Salomonson, A simulation study exploring the effects of sensor spatial resolution on estimates of cloud cover from satellites, *J. Appl. Meteor.*, *11*, 214-220, 1972.

Shettle, E.P., and R.W. Fenn, Models of the aerosols of the lower atmosphere and the effects of humidity variations on their optical properties, *AFGL-TR-79-0214*, 1979.

Shettle, E.P., F.X. Kneizys, S.A. Clough, G.P. Anderson, L.W. Abreu, and J.H. Chetwynd, Cloud models in LOWTRAN and FASCODE, *Proceedings of the Cloud Impacts on DOD Operations and Systems 1988 Workshop*, Silver Spring, MD, 18-20 Oct. 1988.

Simmonds, I. and W.F. Budd, A simple parameterization of ice leads in a general circulation model and the sensitivity of climate to change in Antarctic ice concentration, *Annals of Glaciol.*, *14*, 266-269, 1990.

Smith, S.D., R.J. Anderson, G. den Hartog, D.R. Topham, and R.G. Perkin, An investigation of a polynya in the Canadian archipelago, 2, Structure of turbulence and sensible heat flux, *J. Geophys. Res*, *88*, 2900-2910, 1983.

Spinhirne, J.D., and M.D. King, Latitudinal variation of spectral optical thickness and columnar size distribution of the El Chichon stratospheric aerosol layer, *J. Geophys. Res.*, *90*(D6), 10,607-10,619, 1985.

Stamnes, K., S-C Tsay, W. Wiscombe, and K. Jayaweera, Numerically stable algorithm for discrete-ordinate-method radiative transfer in multiple scattering and emitting layered media, *Applied Optics*, *27*, 2502-2509, 1988.

Steffen, K., Fractures in arctic winter pack ice (North Water, northern Baffin Bay), *Annals Glaciol.*, *9*, 1-4, 1987.

Steffen, K., J. Heinrichs, J. Maslanik, and J. Key, Sea ice feature and type identification in merged ERS-1 SAR and Landsat Thematic Mapper Imagery, First ERS-1 Symposium, ESA SP-359, Cannes, France, 1993.

Stephens, G.L., The transfer of 3.7μm radiation through model cirrus clouds. Preprints, *Fourth Conference on Atmospheric Radiation*, Boston, American Meteorological Society, 214-216, 1981.

Stone, R.S., G.L. Stephens, C.M.R. Platt, and S. Banks, The remote sensing of thin cirrus cloud using satellites, lidar and radiative transfer theory, *J. Appl. Meteorol.*, *29*, 353-366, 1990.

Stone, R. and J. Key (1993), The detectability of winter sea ice leads in thermal satellite data under varying atmospheric conditions. *J. Geophys. Res. (Oceans)*, in press.

Stone, R.S., Properties of austral winter clouds derived from radiometric profiles at the south pole, *J. Geophys. Res.*, in press, 1993.

Stowe, L.L., C.G. Wellemeyer, T.F. Eck, H.Y.M. Yeh, and The Nimbus-7 Cloud Data Processing Team, Nimbus-7 global cloud climatology. Part I: algorithms and validation, *J. Climate*, 1, 445-470, 1988.

Stoyan, D., W.S. Kendall, and J. Mecke, *Stochastic Geometry and its Applications*. New York: Wiley, 345 pp., 1989.

Toon, O.B., and J.B. Pollack, A global average model of atmospheric aerosols for radiative transfer calculations, *J. Appl. Meteorol.*, *15*, 225-246, 1976.

Townshend, J.R.G. and C.O. Justice, Selecting the spatial resolution of satellite sensors required for global monitoring of land transformations, *Int. J. Remote Sensing*, *9*(2), 187-236, 1988.

Tsay, S.C., K. Stamnes, and K. Jayaweera, 1989. Radiative energy budget in the cloudy and hazy arctic. *J. Atmos. Sci.*, *46*(7), 1002-1018.

Tsay, S.C., and K. Jayaweera, Physical Characteristics of Arctic Stratus Clouds. *J. Climate Appl. Meteor.*, *23*, 584-596, 1984.

Valero, F.P.J., T.P. Ackerman, and W.J.Y. Gore, Radiative effects of the Arctic haze, *Geophys. Res. Lett.*, *10*(12), 1184-1187, 1983.

Valero, F.P.J., Ackerman, T.P., and W.J.Y. Gore, The effects of the Arctic haze as determined from airborne radiometric measurements during AGASP II, *J. Atmos. Chem.*, *9*, 225-244, 1989.

van de Hulst, H.C., *Light Scattering by Small Particles*, Dover Publications, N.Y., 470 pp., 1981.

Vowinckel, E., and S. Orvig, The Climate of the North Polar Basin. *World Survey of Climatology*, *14*, Climates of the Polar Regions, Elsevier, 129-252, 1970.

Wadhams, P. and R.J. Horne, An analysis of ice profiles obtained by submarine sonar in the Beaufort Sea, *J. Glaciol.*, *25*(93), 401-424, 1980.

Wadhams, P., Sea-ice topography of the Arctic Ocean in the region 70°W to 25°E, *Philos. Trans. Royal Soc. London*, 302, 45-85, 1981.

Wadhams, P., The underside of the Arctic sea ice imaged by sidescan sonar, *Nature*, 333, 161-164, 1988.

Wahiche, C., N.A. Scott, and A. Chedin, Cloud detection and cloud parameters retrieval from the satellites of the TIROS-N series, *Annales Geophysicae*, *4*, B, 2, 207-222, 1986.

Warren, S.G., C.J. Hahn, J. London, R.M. Chervin, and R.L. Jenne, Global Distribution of Total Cloud

Cover and Cloud Type Amounts over the Oceans, DOE/ER-0406, *National Center for Atmospheric Research Technical Note NCAR/TN-317+STR*, 42 pp. plus maps, December 1988.

Wielicki, B.A. and R.M. Welch, Cumulus cloud properties derived using Landsat satellite data, *J. Clim. Appl. Meteorol.*, 25, 261-276, 1986.

Wielicki, B.A. and L. Parker, On the determination of cloud cover from satellite sensors: the effect of sensor spatial resolution, *J. Geophys. Res.*, 97(D12), 12799-12823, 1992.

Woodcock, C.E. and A.H. Strahler, The factor of scale in remote sensing, *Remote Sensing Environ.*, 21, 311-316, 1987.

Yamanouchi, T., K. Suzuki, and S. Kawaguchi, Detection of clouds in Antarctica from infrared multispectral data of AVHRR, *J. Meteorol. Soc. Japan*, 65, 949-961, 1987.